

# Medical University of Białystok

Faculty of Medicine with the Division of Dentistry  
And Division of Medical Education in English



Doctoral dissertation in Medical Science

## **Impact of the expression modulation of Aquaporin 9 on proteomic profile and oxidative stress homeostasis in HepG2 model of hepatic lipid overload**

---

Mauro Galli

Supervisor: **dr hab. Piotr Zabielski**,  
Department of Medical Biology,  
Medical University of Białystok

Białystok 2022



This research was conducted within the project which has received funding from the European Union's Horizon 2020 research and innovation programme under the Marie Skłodowska-Curie grant agreement No 754432 and the Polish Ministry of Science and Higher Education, from financial resources for science in 2018-2023 granted for the implementation of an international co-financed project.

## Acknowledgments

Once again I am reaching a new goal in my life, a Ph.D. title. Ten years ago I would have never imagined me walking down this road and yet I am. When I look back, I see the faces of a lot of people always on my side, supporting me and my dreams.

The first of them is Vanessa, always on my side, always supporting all of my choices. First, I would like to thank you for following me here, in the remote corner of Poland. It has been a jump that required a lot of courage and resilience, especially for the language issues we had at the beginning. Thank you for tolerating my being silly and for facing together the obstacles in front of us. A huge thanks goes also to my family, in Italy: mom Sandra, dad Giorgio, Luca, Isa and the magical twins Linda e Beatrice. I know it has been difficult for you to see me leaving my home country to run into my adventurous life, but you never stopped supporting me and making me feel you are close. I'll be always there, even if I am far.

Huge thanks are for Arek, always available for a coffee break in the lab. I will never forget our cleaning sessions in the cell culture room! You have helped me by lending me your time when I had none left to complete this project. Thank you! I would like to thank also Damian, Karolina, Paula, Anna, Kamila, Monica, Adam, Alicia and all the other lab members to help me despite me being the English-speaking guy.

I could never thank enough Iria for being there, always. You trained me step-by-step, first in Italy, then remotely and finally in Spain. It seems our faith is somehow bound, or maybe we just like to work together. I will never repay you my debt for transforming me into the scientist I am today, always torturing me to make me improve. You have always done more than you were supposed to do for me and I will always acknowledge it. There are few people you can trust in life, and you are one of those. Speaking about Spain, I have to thank also Angie. I met you in Iria's lab and I taught you as much as I could. On the other side, you have always been available and eager to help me: we both know I could not have done all that workload alone in Spain. Thank you, you are part of this! Thank you also to Cristina, Edu, Gonzalo and all the other lab members I met at the UC3M!

Stefano, how can I leave you out of this? I am sure you don't expect to be here, but actually, you are essential. You taught me everything I know about microscopy and I needed all of it in this experience. Plus, if I have a problem, you are always there trying to help me! Thank you!

I would like to thank also all my travel companions in the ImPRESS project: it has been hard, but we are doing it guys! A special mention goes to Alessandro and Viviana. Despite we spent just one year together in Bialystok, it has been amazing! Thank you guys, everything was easier when you were here! Jordan, my friend... it is a pleasure to share this adventure with you. Besides, I can say that I've got a US friend now! And thank you, Gladys, Anna, Felipe, Mirkan, Synemyz, Efe: it has been a pleasure meeting you and sharing fantastic moments! Thanks also to my Italian friends Dario and Michael, the pandemic with you has been much easier!

I am sure I am not citing a lot of people who contributed to making my polish journey unique: thank you all guys!

<b>1</b>	<b>Abbreviations .....</b>	<b>6</b>
<b>2</b>	<b>Tables and Figures list.....</b>	<b>9</b>
2.1	<i>Tables.....</i>	9
2.2	<i>Figures.....</i>	9
<b>3</b>	<b>Introduction.....</b>	<b>11</b>
3.1	<i>Obesity and Insulin resistance .....</i>	<i>11</i>
3.2	<i>ROS &amp; redox regulation .....</i>	<i>13</i>
3.3	<i>Integral membrane proteins.....</i>	<i>14</i>
3.4	<i>Aquaporins.....</i>	<i>15</i>
3.5	<i>Aquaporins, insulin resistance and type 2 diabetes.....</i>	<i>17</i>
3.6	<i>The importance of high-throughput untargeted proteomics in the study of pleiotropic effects of AQP modulation.....</i>	<i>20</i>
<b>4</b>	<b>Aims.....</b>	<b>25</b>
<b>5</b>	<b>Material and methods.....</b>	<b>26</b>
5.1	<i>Cell culturing and samples collection .....</i>	<i>26</i>
5.2	<i>Reagents and treatments .....</i>	<i>26</i>
5.3	<i>FFAs-BSA conjugation protocol.....</i>	<i>27</i>
5.4	<i>SDC-assisted lysis method .....</i>	<i>27</i>
5.5	<i>MCX zip-tipping for peptides desalting/cleaning .....</i>	<i>28</i>
5.6	<i>MS acquisition .....</i>	<i>29</i>
5.6.1	<i>Data-dependent analysis (DDA).....</i>	<i>29</i>
5.6.2	<i>Data-independent analysis (DIA) .....</i>	<i>30</i>
5.7	<i>Data analysis .....</i>	<i>30</i>
5.7.1	<i>Ion chromatogram libraries .....</i>	<i>30</i>
5.7.2	<i>DIA analysis .....</i>	<i>31</i>
5.8	<i>Bioinformatics analysis with Lasagna 2.0.....</i>	<i>31</i>
5.9	<i>Lipid droplets staining with Oil red O.....</i>	<i>32</i>
5.10	<i>Lipid droplets staining with Bodipy 493/503.....</i>	<i>32</i>
5.11	<i>Apoptosis assay.....</i>	<i>32</i>
5.12	<i>Microscope short time-lapse experiments .....</i>	<i>32</i>
5.13	<i>Microscope long time-lapse experiment.....</i>	<i>33</i>
5.14	<i>Digitonin treatment.....</i>	<i>33</i>
5.15	<i>Microscope images analysis .....</i>	<i>34</i>

5.16	<i>Statistical analysis</i> .....	34
5.17	<i>R graphs</i> .....	34
<b>6</b>	<b>Results</b> .....	<b>35</b>
6.1	<i>Data Independent Acquisition (DIA) development I: Variable windows width</i> .....	35
6.2	<i>Untargeted proteomics analysis of human liver samples</i> .....	40
6.3	<i>Bioinformatics analysis of the AQP9 promoter</i> .....	47
6.4	<i>HepG2 lipid overload model</i> .....	48
6.5	<i>AQP9 upregulation in lipid overload HepG2 model activates apoptosis</i> .....	51
6.6	<i>Insulin signaling influence on hydrogen peroxide flux</i> .....	52
6.7	<i>Lipid overload decrease the hydrogen peroxide transport in HepG2 liver cells</i> .....	53
6.8	<i>Oxidative stress accumulation in the endoplasmic reticulum of Lipid overloaded HepG2 cells</i> .....	54
6.9	<i>Is there a reductive shield around the endoplasmic reticulum?</i> .....	55
6.10	<i>Data Independent Acquisition (DIA) development II: Staggered windows width</i> .....	56
6.11	<i>Ion libraries refinement</i> .....	59
6.12	<i>Windows scheme refinement</i> .....	62
6.13	<i>Coefficient of variation and ID m/z distribution</i> .....	64
6.14	<i>Biological experiment validation</i> .....	65
6.15	<i>Untargeted proteomics analysis of HepG2 under lipid overload and with AQPs modulation</i> .....	66
6.15.1	<i>LO(+) vs Ctrl</i> .....	66
6.15.2	<i>LO(+) + AQP9 vs LO(+)</i> .....	68
6.15.3	<i>LO(+) + AQP9i vs LO(+)</i> .....	70
6.15.4	<i>LO(+) + AQP9 VS LO(+) + AQP9i</i> .....	72
<b>7</b>	<b>Discussion</b> .....	<b>74</b>
7.1	<i>MS method development</i> .....	74
7.2	<i>Isolation windows in DIA proteomics</i> .....	77
7.3	<i>Untargeted analysis of human liver samples</i> .....	78
7.4	<i>In-silico analysis of the promoter of AQP9</i> .....	79
7.5	<i>AQP9 involvement in lipids accumulation in HepG2 cells</i> .....	80
7.6	<i>AQP9 and oxidative stress</i> .....	83
7.7	<i>Advanced DIA development</i> .....	85
7.8	<i>Untargeted analysis of HepG2 under lipid overload and AQP9 modulation</i> .....	89
7.9	<i>AQPs relevance in lipid overload and insulin resistance development in hepatic cells</i>	92

<b>8</b>	<b>Conclusions .....</b>	<b>95</b>
<b>9</b>	<b>Bibliography .....</b>	<b>96</b>
<b>10</b>	<b>Abstract.....</b>	<b>115</b>
<b>11</b>	<b>Abstract in Polish.....</b>	<b>117</b>
<b>12</b>	<b>Supplementary materials .....</b>	<b>119</b>

## 1 Abbreviations

•OH	Hydroxyl radical
11i	siRNA-silenced AQP11
11mf	AQP11mycFlag
9i	siRNA-silenced AQP9
9mf	AQP9mycFlag
ACN	Acetonitrile
Acyl-CoA	Acyl-coenzyme A
AGPAT	1-acylglycerol-3-phosphate-O-acyltransferase
AKT	Protein kinase B
AQP0	Aquaporin 0
AQP1	Aquaporin 1
AQP10	Aquaporin 10
AQP11	Aquaporin 11
AQP12	Aquaporin 12
AQP2	Aquaporin 2
AQP3	Aquaporin 3
AQP4	Aquaporin 4
AQP5	Aquaporin 5
AQP6	Aquaporin 6
AQP7	Aquaporin 7
AQP8	Aquaporin 8
AQP9	Aquaporin 9
AQPs	Aquaporins
ARE	Antioxidant response element
Aromatic/R	aromatic/arginine
ATP	Adenosine triphosphate
AVG XIC	Average extracted ion chromatogram peak width
CE	Collision energy
CEBPA	CCAAT Enhancer Binding Protein Alpha
CER	Ceramide
CHOP	DNA damage-inducible transcript 3
Ctrl	Control
CVs	Coefficients of variation
DAG	Diacylglycerol
DDA	Data-dependent acquisition
DIA	Data-independent acquisition
Digi	Digitonin
DNS	Data not shown
DTT	Dithiothreitol
EGF	Epidermal Growth Factor
ER	Endoplasmic reticulum
FABPs	Fatty acids binding proteins
FATPs	Fatty acids transport proteins
FDR	False discovery rate

FFAs	Free fatty acids
FWHM	Full width at half maximum
GAS	Optimized -gas source parameters
Glycerol-3P	Glycerol 3 phosphate
GPAT	Glycerol-3-phosphate acyltransferase
GPF	Gas-phase fractionation
GPFs	Gas-phase fractions
GSH	Reduced glutathione
GSSG	Oxidized glutathione
H <sub>2</sub> O <sub>2</sub>	Hydrogen peroxide
HepG2	Hep G2 Cell Line human
HIGH	Optimized - gas, temperature and voltage source parameters
HMOX1	Heme Oxygenase 1
HMOX2	Heme Oxygenase 2
HpH	High pH
ID	Identification
IGT	Impaired glucose tolerance patients
kDa	kilo-Dalton
Keap1	Kelch-like ECH-associated protein 1
LC	Liquid chromatography
LO	Lipid overload
LO(+)	Lipid overload + insulin
LPIN1	Lipin-1 Phosphatidate phosphatase
LUT	Look-up table
m/z	mass/charge
MAMs	Mitochondrial associated membranes
mM	millimolar
MS/MS	Tandem mass spectrometry
MS1	Mass spectrometry
MS2	Tandem mass spectrometry
NADPH	Reduced nicotinamide adenine dinucleotide phosphate
ND	Non-diabetic patients
NO	Nitric oxide
NOXes	NADPH oxidases
NPA	asparagine-proline-alanine
NPC	asparagine-proline-cysteine
Nrf2	Nuclear factor-erythroid 2 related factor 2
O <sub>2</sub>	Oxygen
O <sub>2</sub> -	Superoxide anions
OPT	Optimized - gas and temperature source parameters
Orbitrap-MS	Orbitrap mass spectrometry
PDB	Protein data bank
PI3K	Phosphatidylinositol 3-kinases
PKC	Protein Kinase C
PM	plasma membrane
RCSB	Research Collaboratory for Structural Bioinformatics

ROIs	Region of interest
ROS	Reactive oxygen species
RP-LC	Reversed-phase liquid chromatography
siRNA	small interfering RNA molecules
SODs	Superoxide dismutases
STAT1	Signal transducer and activator of transcription 1
STD	Standard source parameters
STW	Staggered windows
T2D	Type-2 diabetic patients
T2DM	Type 2 diabetes mellitus
TAL1	T-cell acute lymphocytic leukaemia protein 1
TIC	Total ion chromatogram
TKR	Receptor tyrosine kinase
TOF-MS	Time-of-flight mass spectrometry
TXN	Thioredoxin
VWW	Variable windows width
WHO	World Health Organization
$\mu$ LC	Micro liquid chromatography
mM	micromolar

## 2 Tables and Figures list

### 2.1 Tables

Table I. Source parameters optimization.	p.35
Table II. Gradients optimization.	p.36
Table III. CE equations.	p.38
Table IV. AQP9 predicted binding sites.	P.47

### 2.2 Figures

Figure 1. Adipose tissue and insulin resistance.	p.12
Figure 2. Aquaporins structure.	p.17
Figure 3. DDA and DIA.	p.22
Figure 4. Source optimization results.	p.36
Figure 5. LC gradients comparison.	p.37
Figure 6. Ion spectrum match.	p.38
Figure 7. Swath tuner variable windows.	p.39
Figure 8. HpH fractionation.	p.41
Figure 9. Identifications and CVs of DIA analysis on human liver samples.	p.42
Figure 10. AQP9 expression levels in human liver samples.	p.43
Figure 11. FABPs expression levels in human liver samples.	p.44
Figure 12. DAG synthetic pathway analysis.	p.45
Figure 13. Oxidative stress analysis.	p.46
Figure 14. AQP9 promoter bioinformatics analysis.	p.47
Figure 15. Cells count and viability.	p.48
Figure 16. Lipid droplets staining with oil red O.	p.49
Figure 17. Lipid droplets staining with Bodipy 493/503	p.49
Figure 18. Lipid droplets accumulation.	p.50

Figure 19. Apoptosis activation.	p.51
Figure 20. Insulin-stimulated H <sub>2</sub> O <sub>2</sub> fluxes.	p.52
Figure 21. H <sub>2</sub> O <sub>2</sub> transport inhibition.	p.53
Figure 22. Lipid-induced H <sub>2</sub> O <sub>2</sub> accumulation in the ER.	p.54
Figure 23. HyPer responsiveness and basal state anomalies.	p.55
Figure 24. DIA methods schemes.	p.57
Figure 25. Ion libraries depths and performances.	p.58
Figure 26. Improved ion libraries depth.	p.59
Figure 27. Libraries yield comparison.	p.60
Figure 28. DIA cycle times comparisons.	p.62
Figure 29. Windows schemes improvements.	p.63
Figure 30. CVs and IDs analysis in different windows schemes.	p.64
Figure 31. HpH-VWW and GPF-40STW performance comparison in a biological experiment.	p.65
Figure 32. LO (+) VS Ctrl	p.67
Figure 33. LO (+) + AQP9 VS LO(+)	p.69
Figure 34. LO (+) + AQP9i VS LO(+)	p.71
Figure 35. LO (+) + AQP9 VS LO(+) + AQP9i.	p.73

### 3 Introduction

#### 3.1 Obesity and Insulin resistance

Obesity and obesity-connected metabolic diseases are recognized worldwide as expanding health problem. The modern lifestyle together with the socioeconomic conditions, the cultural influences, and also the genetic predisposition, are the deep roots leading to it. WHO global estimates in 2016 stated that 39% of adults were overweight and 13% obese, while overweight and obese children/adolescents percentage raised from 4% in 1975 to 18% in 2016. The unstoppable spread of this issue in all ages and with no boundaries justifies the term Globesity – global obesity epidemic [1,2]. Obese people are subject to a higher risk of developing comorbidities, a spectrum covering a variety of disturbances: from hypertension and cardiovascular disease to dyslipidemia, insulin resistance and type-2 diabetes (T2D) [3]. These are the most relevant comorbidities of obesity, which were recently proven to be involved in the increase of complications insurgence and mortality rate of COVID-19 patients [4]. The adipose tissue accumulating in obese people increases the synthesis of harmful adipokines (resistin, visfatin, etc.) and pro-inflammatory cytokines (TNF $\alpha$ , IL-6, etc.) with a subsequent major generation of reactive oxygen species (ROS), connected with inflammation, oxidative stress and mitochondrial dysfunction. Additionally, the excess of adipose tissue is associated with a rise in the levels of circulating free fatty acids (FFAs) (**Figure 1**). Both ROS and FFAs' abnormal concentrations are strictly connected with the development of insulin resistance and type-2 diabetes [3,5]. The insulin-sensitive organs such as the liver, skeletal muscles, and adipose tissue suffer from insulin resistance. It arises from their decreased metabolic response to insulin, the hormone responsible for the regulation of glucose, lipid and amino acid homeostasis [6]. The development of insulin resistance can stay silent for many years, being compensated by increased  $\beta$ -cells secretory activity to grant the metabolic homeostasis. The excessive amount of adipose tissue in obese people is subject to the development of insulin resistance. This leads to systemic consequences: on one side, fat tissue decrease the generation of beneficial adipokines (leptin, adiponectin), on the other side it increases the synthesis and release of pro-inflammatory cytokines (TNF $\alpha$ , IL-6). Moreover, there is a boost in plasma FFAs and free glycerol driven by the major lipolysis of triacylglycerol stores, which cannot be efficiently controlled by lipogenic insulin signaling [5,7]. Consequently, obesity is behind the augmentation of the bioactive lipids diacylglycerol (DAG) and ceramide (CER) in the liver and skeletal muscles [8,9]. An association between the high amount of DAG in the liver and activation of a different isoform of PKC has been

found. This isoform contributes to the inhibition of the insulin signaling, being responsible for diminished phosphorylation of the insulin receptor substrate [10]. FFAs and glycerol access the liver through dedicated channels. FFAs hepatic transporters are fatty acids transporters (FATPs) and fatty acid-binding proteins (FABPs) whose involvement in hepatic bioactive lipids accumulation and insulin resistance has been extensively studied [11,12]. In the last decades scientists individuated in aquaporin the proteins responsible for the transport of glycerol in both adipose tissue and liver, nominating them as new possible molecular targets involved in insulin resistance development [13–16].

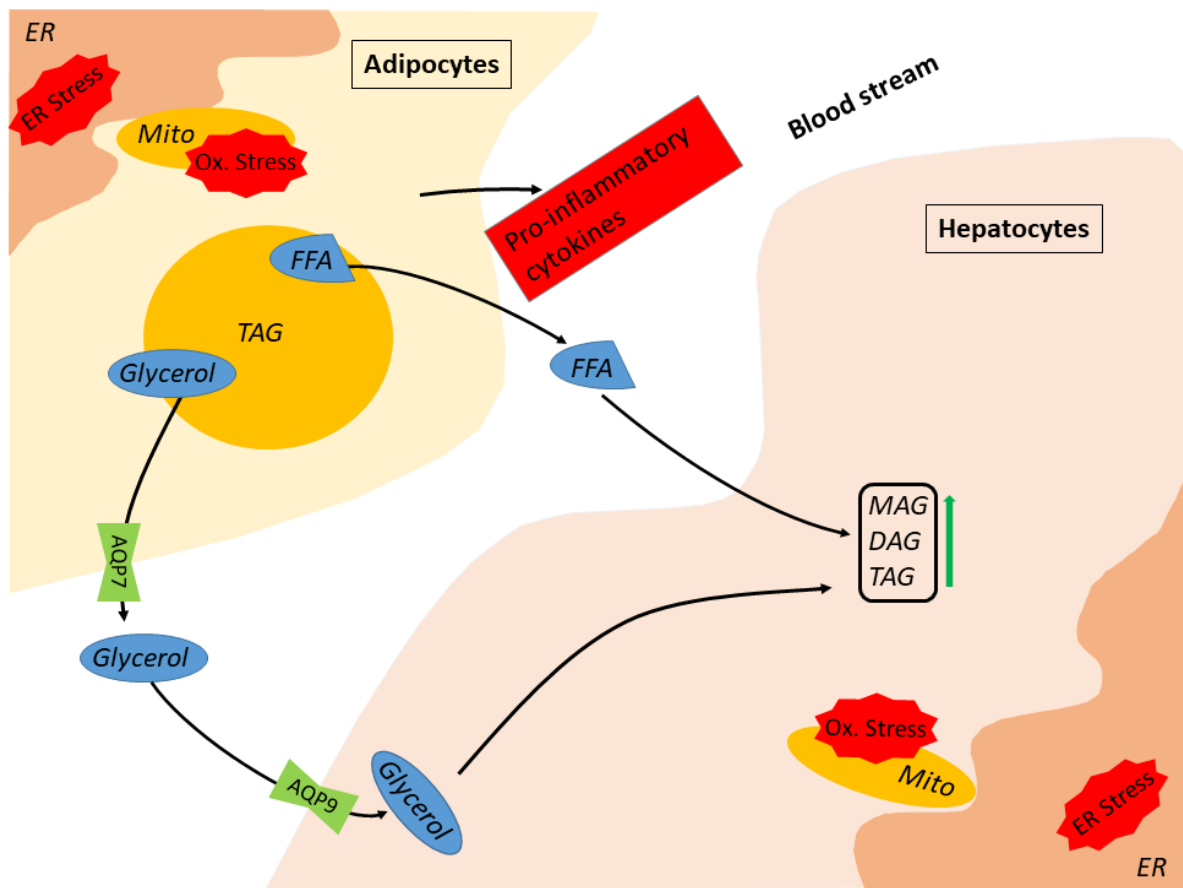


**Figure 1.** Adipose tissue and insulin resistance. Adipose tissue accumulation brings to the increase of the release in plasma of free fatty acids, glycerol and pro-inflammatory cytokines. FFA and glycerol reach the liver through the bloodstream and promote the accumulation of diacylglycerol, which has been shown to be connected with insulin resistance development in the liver. The lipids accumulation leads to the development of oxidative stress and ER stress in both tissues.

### 3.2 ROS & redox regulation

Reactive oxygen species (ROS) have always been a matter of discussion in the scientific community. Reactive oxygen species, a group of molecules derived from molecular oxygen characterized by a high reactivity, consist of free radicals including singlet oxygen ( $O_2$ ), hydroxyl radical ( $\bullet OH$ ) and superoxide anions ( $O_2^-$ ). On the other side, it includes also nonradical molecules such as hydrogen peroxide ( $H_2O_2$ ) and reactive nitrogen species such as nitric oxide (NO) [17,18]. ROS' role inside the cells is still discussed, most of the research points at their harmful effects, yet some data underlines their importance in the balancing of the signalling processes and cells' life. Nowadays the most researches agree that ROS display both beneficial and harmful properties, depending on their release mechanism, intracellular compartmentalization and concentration. ROS are essential signalling molecules for the development of the cell and for maintaining good signalling, but this is valid till they are present in a controlled concentration [19,20]. Another proof of the importance of ROS in the cells is the existence of ROS producers called NADPH oxidases (NOXes) [21]. The members of this family of oxidoreductases produce superoxide anions, subsequently processed by the superoxide dismutases (SODs) in hydrogen peroxide, which can be effectively transported by aquaporins. Aquaporins have been shown to take part in signalling pathways in the cells which involve  $H_2O_2$  trafficking [22,23]. On the other side, metabolic dysfunctions or environment-induced stresses leading to a further accumulation of ROS are dangerous for the cells [24,25]. An uncontrolled presence of ROS facilitates the peroxidation of lipids, proteins and nucleic acids, altering properties of biological membranes, affecting enzyme activity and protein degradation and disturbing gene expression and regulation. Other side effects of dysregulation in ROS metabolism are higher risks of cell senescence, apoptosis, necrosis and carcinogenesis [18].

To limit the damage caused by the ROS the cells develop multiple mechanisms of antioxidant defence, both enzymatic and non-enzymatic, which are able to maintain the redox homeostasis. Catalase, glutathione peroxidase, peroxiredoxin and superoxide dismutase are the main enzymes of the antioxidant system. There are many other compounds with an antioxidant effect, whose most relevant are glutathione, thioredoxin and glutaredoxin [26,27]. Catalase controls the concentration of  $H_2O_2$  with a 2-steps reaction. This ubiquitous enzyme is very active in the liver and converts  $H_2O_2$  to water and molecular oxygen [28]. Superoxide dismutases are the first line of defence against ROS, dismutating superoxide anions to molecular oxygen and hydrogen peroxide, subsequently converted by catalase to water and

molecular oxygen. SOD requires the collaboration of other enzymes such as catalase or glutathione peroxidase to control the  $H_2O_2$  levels [29]. Peroxiredoxins, or thioredoxin peroxidase, influence the levels of  $H_2O_2$  and have a double role both in signalling and oxidative stress control [30]. The thioredoxins, cooperating with NADPH and thioredoxin reductases, have an important role in reducing disulphides in proteins and peptides [31]. Glutathione is a ROS quencher situated mainly in the cytosol, but also the ER, peroxisomes, nuclear matrix and mitochondria of the cells. Its function is driven by the equilibrium between the reduced form (GSH) and the oxidized one (GSSG), connecting two molecules of GSH. The reduced form is important in defending important structures from electrophilic agents and it is a cofactor for glutathione peroxidase and glutathione transferase. Glutathione is also part of the glutaredoxin system [32,33].

The antioxidant defences responding to a problem need to be coordinated, and one of the coordination levels is done at the level of gene regulation. The insurgence of oxidative stress activates a response synchronously modulating the expression of the target genes. The molecule orchestrating this is Nrf2 (Nuclear factor erythroid 2-related factor 2), a transcription factor which binds to the antioxidant response element present on all the genes which take part in the antioxidant response [34,35]. Nrf2, a basic leucine-zipper transcription factor, is ubiquitously expressed and normally under continuous repression. The inactive form of Nrf2 is free-floating in the cytoplasm bound to the redox-sensitive Kelch-like ECH-associated protein 1 (Keap1). The high sensitivity of Keap1 to the small redox variations is the trigger of the antioxidant defence system. When the ROS levels increase, Keap1 is not able to bind Nrf2 anymore. Free-Nrf2 travels to the nucleus where it activates the expression of the genes carrying an antioxidant response element (ARE), binding target of Nrf2 [36]. The list of known targets of Nrf2 includes antioxidant genes, NADPH-generating enzymes, drug-metabolizing enzymes, drug transporters and stress response proteins [37]. Many other Nrf2 targets need to be discovered yet and the chance that aquaporins could be one of those has to be considered. There are already examples of transporters modulated by the concentration of its substrates, such as the sodium-potassium pumps or the calcium pumps [38–41]. Similarly, aquaporins transporting  $H_2O_2$  could be modulated by Nrf2 to control the redox homeostasis of the cells.

### 3.3 *Integral membrane proteins*

Living cells have to recover from extracellular space rough material necessary for biosynthesis and energy production. In parallel, they have to release metabolism wastes in the

same extracellular space. Furthermore, the need for the cells to interface and interconnect with nearby cells and the full organism has to be considered. Since the free passage through the lipidic double layer is granted just to a few non-polar and small compounds cells need the help of proteins. Free diffusion indeed is basal and passive transportation driven by the electrochemical gradient with limited capabilities [42]. The best tool that evolution has provided to the cells to bypass their plasma membrane is the integral membrane proteins, a big family of proteins spreading from contact sites to channels, from receptors to ion pumps [43]. In some cases, integral membrane proteins simplify the passage of molecules following their concentration gradient, but often the movement of molecules is against their concentration or electrical gradient, requiring active transporters. Those transporters, part of the carriers, can pump compounds in or out of a cell using a source of energy as ATP [44]. Carriers can also be passive, transporting compounds according to the gradient and do not requiring any energy consumption. On the other side, there are protein channels that allow a much faster transmembrane flow compared to the typical transporters, nearing the physical limit of the free diffusion [45]. Membrane channels are mostly oligomeric, composed of multiple subunits that are often identical. Channels are less stereospecific of the transporters and usually facilitate transmembrane movement trafficking of a group of chemically similar compounds. Composed of alpha-helix segments or beta-barrels structures, the channels saturation point is rarely reached. Aquaporins are channels of raising interest in the last years: first discovered as water transporters, the list of molecules they are able to handle is steadily increasing [46].

### 3.4 *Aquaporins*

The two most important features for cells' survival and adaptation, are the water homeostasis and the energy balance. Aquaporins are the key players in the regulation of the water passage, which is driven by osmotic and hydrostatic pressures [47–49]. Aquaporins are tetrameric proteins, whose relatively low molecular mass monomer weighs approx. 30kDa. Generally, the monomers are the result of the connection of 6 tilted alpha-helix regions with 5 loops. The selective properties of aquaporins in transporting particular class of compounds result from the restriction sites present inside the pore of the monomer. One restriction site is called the NPA, composed of 2 asparagine-proline-alanine sequences facing each other and responsible for the dimensional filtering. The other, shared by most of the aquaporins, is an aromatic/R site, conferring the selectivity properties to the AQPs (**Figure 2**) [46,50]. Typically, aquaporins are located in the plasma membrane, except for some of them present in

subcellular compartments as AQP11 [51]. Being integral membrane proteins, aquaporins possess highly hydrophobic transmembrane domains. This makes the crystallization process more complicated and the 3D structure has been identified only for a few of them, increasing the importance of the bioinformatics modeling approaches [52]. The relevance of those proteins is highlighted by their vast diffusion in both the plant and animal world: numerous aquaporins have been discovered in plants and 13 in mammals [53]. The mammals' aquaporins are traditionally divided into three distinct groups: the classical aquaporins, the aquaglyceroporins, and the superaquaporins [54]. The classical AQPs subfamily includes all the aquaporins mainly dedicated to the water transport, as AQP0, AQP1, AQP2, AQP4, and AQP5. The channels transporting other small molecules like hydrogen peroxide, urea, glycerol and ammonia are usually inserted in the aquaglyceroporin subfamily. Scientists are discovering new solutes transported by them, but they are generally called aquaglyceroporins. In this subfamily, we can find AQP3, AQP6, AQP7, AQP8, AQP9, and AQP10 [23,55–58]. The so called superAQPs family can be considered as a separate branch of AQPs, and is composed of two proteins with many peculiarities. The sequence homology with the other 2 subfamilies is low and the NPA site is not completely conserved, changing to NPC (asparagine-proline-cysteine) [59,60]. On the other side, AQP could also be categorized starting from the main functional role performed in the cells: aquaporins, which transport water, glyceroporins, involved in glycerol trafficking, and peroxiporins, responsible for transmembrane hydrogen peroxide fluxes [61]. Understanding AQPs' role is more important than the classical categorization based on what is transported in these channels. AQP0 is assigned to the water transporter AQPs by sequence homology, but it has been shown that the water flux through AQP0 is almost absent, pushing the consideration that it is a structural aquaporin [62]. AQP8 is correctly listed in aquaglyceroporins, but it could be considered a standalone family. This AQP shows a different phylogenetic path and recently scientists showed its unique role in signaling modulation, with a particular mechanism of oxidative stress-related closure mechanism [52,63–65]. AQP11 is an ER-resident aquaporin, dedicated to the transport of hydrogen peroxide [51]. AQP3 can be enlisted in the peroxiporins, given its recently shown involvement in the insulin signaling modulation of a hepatic cell line [22]. Anyway, AQPs connection with a number of molecules and cellular pathways would justify a flexible characterization of these molecules, allowing for the assignment of certain aquaporins to multiple groups.

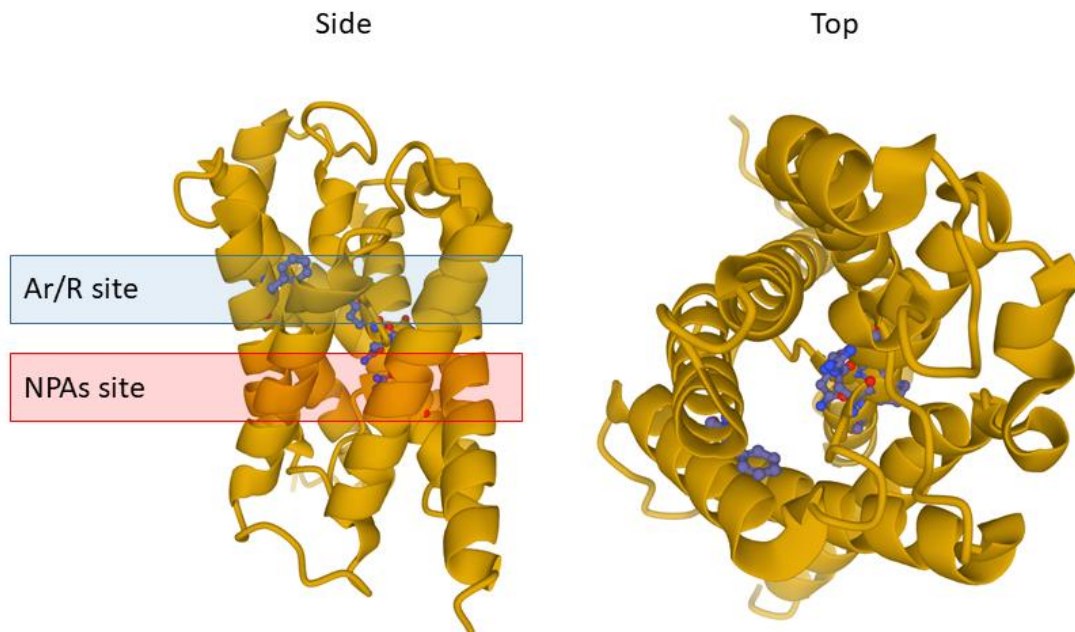


**Figure 2.** Aquaporins structure. The figure shows the 3D structure of Aquaporin 10, shared by most of the AQPs. The ribbons represent the alfa-helix structures and the lines the connection loops. In blue are represented the amino acids of the two restriction sites of the AQPs, NPAs and ar/R. The figure is based on the RCSB PDB [18] crystal structure of AQP10 (PDB ID: 6F7H) published by Gotfryd et al. [19]; the images has been prepared with the use of mol\* software [20].

### 3.5 *Aquaporins, insulin resistance and type 2 diabetes*

Aquaporins, insulin resistance and Type 2 diabetes (T2DM) could be considered distant topics and some could wonder what is the possible connection between them. The role of gatekeepers of the cells makes these channels more important and more interconnected with the diseases than expected. Additionally, we have to consider obesity-induced T2DM as a systemic disease, induced by unbalances of the human metabolism which is connecting multiple organs and tissues [66]. The fact that nowadays a definitive explanation behind T2DM insurgence and treatment has not been discovered, stimulates scientists in considering alternative solutions. The amount of scientific data collected in recent years sustains the formulation of new theories and the expansion of system biology can help confirm those.

Cells, organs and in general the human body are the master adaptation skills. The variations happening inside of an organism as the development of obesity or disease as type 2 diabetes stimulate different responses in different organs and different cells, with the final goal of balancing the energy metabolism. AQPs position at the boundaries of the cells and their role as transporters make them key molecules in the interconnection of multiple organs and cells. This candidates them to have a major role in all those diseases involving multiple tissues as T2DM. The confirmed presence of different AQPs in adipocytes and hepatocytes, dedicated to the transportation of a variety of molecules supports their importance in the development of insulin resistance and T2DM. For example, AQP3 is a hydrogen peroxide transporter present in mice hepatocytes where it could cause first oxidative stress and then acute liver injury. Furthermore, it has been shown the involvement of this AQP in insulin signaling of a hepatocyte cell line, where it modulates the PI3K/AKT branch of the insulin signaling [22,67].

Aquaporins 7 (AQP7) and Aquaporin 9 (AQP9) are recognized as glycerol transporters, allowing glycerol transport through the plasma membrane. AQP7 is highly expressed in adipocytes compared to the other aquaglyceroporins and it is responsible for the glycerol intra and extracellular glycerol flux [68]. AQP9 is believed to be AQP7 counterpart in the hepatocytes [16]. AQP7 and AQP9 can be considered the first step of interconnection since their probable cooperation defines maximum fat-tissue related fatty acids and glycerol load on the liver [69]. Lipolysis in adipocytes due to adipose tissue insulin resistance brings to the hydrolysis of triacylglycerols yielding fatty acids and glycerol [70]. AQP7 favors the export of glycerol, allowing for more efficient lipolysis and increasing the free glycerol and free fatty acids in the bloodstream. The free glycerol reaching the liver is entering the hepatocytes through the AQP9, which facilitates re-esterification of fatty acids towards TAG and DAG. The accumulation of lipid droplets in the liver has been linked with the development of hepatic insulin resistance [71]. Facilitating the access of glycerol used in the DAG and TAG synthesis, AQP7 and AQP9 could be involved in the lipid droplets accumulation and insulin resistance development in the liver. In support of the fact that they are both transporting the same compound, they are also modulated in the same way by the lipogenic or lipolytic signaling. Indeed, these states are influenced by insulin and leptin, two hormones modulating in opposite ways lipid degradation [72]. In normal conditions both those AQPs show a reverse insulin-driven modulation in liver and adipose tissue: fasting is promoting the increase of their levels while feeding is leading to a downregulation [73,74]. In other studies, performed

on HepG2 cells and adipocytes, another type of regulation has been proven. AQP7 and AQP9 presence is negatively modulated by leptin and positively by insulin [72]. Despite a definitive confirmation of their bound has not yet been obtained, their relationship with obesity, insulin resistance and diabetes seems quite strong [13]. Any of those metabolic states possibly influencing their coordination could start a chain of reactions leading to the faster insurgence of metabolic disturbances.

Those are not the only AQPs that can be relevant to the induction of insulin resistance, as other AQP role in the modulation of oxidative stress could be an important factor. AQP11 has recently been shown to be a hydrogen peroxide transporter located in the endoplasmic reticulum. Furthermore, its presence in the mitochondria-associated membranes (MAMs) have been confirmed [51]. So AQP11 could act as a preferential channel for the flow of hydrogen peroxide from mitochondria to the endoplasmic reticulum in the case of mitochondrial dysfunction. This would limit the harm for the cells, accumulating it in an intracellular compartment with high capacity of H<sub>2</sub>O<sub>2</sub> metabolism. Here is where obesity takes its toll, since it is known to induce mitochondrial dysfunction and ER stress in both adipocytes and hepatocytes. The increased accumulation of hydrogen peroxide originated by the mitochondrial dysfunction in the ER overflows the ER radicals sequestering capacity leading to ER stress, which in turn triggers inflammatory response and subsequently, the mitochondrial dysfunction. In other words, obesity stimulates the creation of a vicious cycle that is leading to increased oxidative stress and ROS accumulation in the cells [75–77]. In this chain of oxidative stress confirmed both in adipocytes and hepatocytes, we have to evaluate AQP11's possible roles. Its presence in the MAMs is probably important in the transfer of H<sub>2</sub>O<sub>2</sub> into the ER, but it could also promote H<sub>2</sub>O<sub>2</sub> efflux from the ER. AQP11 participation in H<sub>2</sub>O<sub>2</sub> efflux from the ER has been shown in adipocytes from obese patients, where its overexpression leads to a mitigation of the ER stress [78]. The presence of this compensation is another example of the importance of redox homeostasis and of the importance of aquaporins in the attempt to balance it. A similar mechanism involving AQP11 could be present also in the hepatocytes, but confirmation is still needed [79]. Given all the multiple hints and associations found in the literature, we can see a strong connection between the system of aquaporins and the T2DM development.

### *3.6 The importance of high-throughput untargeted proteomics in the study of pleiotropic effects of AQP modulation*

The utilization of high-throughput proteomics techniques could be crucial to unravel the involvement of AQP9 in hepatic lipid overload and insulin resistance development. A broad study on the highly intricate pathways associated with T2DM and AQPs would help clarifying the mechanisms involving AQP9 and its relevance in them. Mass spectrometry is a world that evolves at an exponentially growing pace. Year by year the introduction of new instrumentations and new bioinformatic algorithms and increasing software capability pushes the boundaries of this discipline a little bit further. In this context, two different instrumental high-resolution approaches contend for supremacy in the field of mass spectrometry-based proteomics: the time of flight mass spectrometry (TOF-MS) and the Orbitrap-based mass spectrometry (Orbitrap-MS). In most cases of the proteomic analysis, both variants are employed in form of tandem mass spectrometry, with first quadrupole and collision cell responsible for the isolation of the peptide ions and generation of product ions with the use of CID (collision-induced dissociation) or HCD (higher energy collision-induced dissociation), respectively, and a high-resolution detector (TOF or Orbitrap) used for the detection of both the precursor ions (MS1 scan) and product ions (MS2 scan). Generally speaking, TOF-MS instruments provide faster overall scanning rate yet display inferior resolution and stability of mass measurement, while Orbitraps offer better mass resolution and stability yet offer significantly lower scanning speed [80,81]. Depending on the main goal one approach can be better than the other, but nowadays both are valid for the traditional proteomics data-dependent acquisition (DDA) and Data Independent Acquisition (DIA). DDA is the most used and easiest to implement approach, both at the level of data acquisition and analysis, with consolidated methods and extensive bioinformatic software options. Tandem mass spectrometer can select ions and induce their fragmentation. The fragments analyzed with high-resolution analyzers allow to identify the peptides by matching the MS/MS fragmentation pattern of the digested peptides with the theoretical one obtained with an in-silico digestion and fragmentation. In DDA mode, usually the Top-10/20/30 most intense peptides from the precursor scan are selected for fragmentation. Despite this, its major drawback consists in reproducibility, given its stochastic nature of the selection of the MS1 precursor peptide ion for the MS2 analysis. For this reason, scientists are more and more interested in the development of DIA methods, which grant a high reproducibility in-between runs. Unluckily, technology limitations and the difficulties in the data analysis due to the generation of very complex product ion MS2 spectra limited the rise of this technology,

which is flourishing nowadays [82]. The high consistency of DIA is an innate ability of this approach since all the ions undergo MS2 fragmentation due to a wider MS1 isolation window. On the other side, the extensive fragmentation results in a highly multiplexed and noisy signal requiring unique bioinformatics resources and software for the proper identification of rich MS2 spectra (**Figure 3**). The only way to cope with the technical limitations is to create precursor isolation windows where the instrument is fragmenting everything inside each window. To satisfy the prerequisites for a precise quantitation 7-9 data points per peak are necessary. This allows precise reconstruction of the MS2 peak shape and area and precise label-free quantitation of the peptide based on at least 3 unique fragment ions. For this reason, the identification has to rely on a previously acquired DDA library [82,83]. The preparation of an extensive DDA library for the DIA projects is one of the major drawbacks of this technique, being both time- and resource-consuming. In the last years, bioinformaticians tried many different solutions to liberate the DIA from its DDA limits, predicting peptides fragmentation to create a completely in-silico library (Prosit software) and developing software not requiring an ion library (for example DIA Umpire, Spectronaut and others) [84,85]. In DIA, data are collected creating m/z mass isolation windows where all the ions are fragmented and acquired in one scan. A sequence of windows is covering the total range of m/z of interest. The basic scheme is composed by a repetition of identical windows (400m/z-450m/z ; 450m/z-50m/z ; ...). Scientists tried to improve DIA also working with the windows schemes. It has been proposed to acquire smaller windows randomly in every cycle of the instrument through entire precursor MS1 mass range to decrease the noise through a demultiplexing algorithm (MSX) or to vary the dimension of the windows based on the mass range and the amount of coeluting ions (variable windows scheme) [86–88].

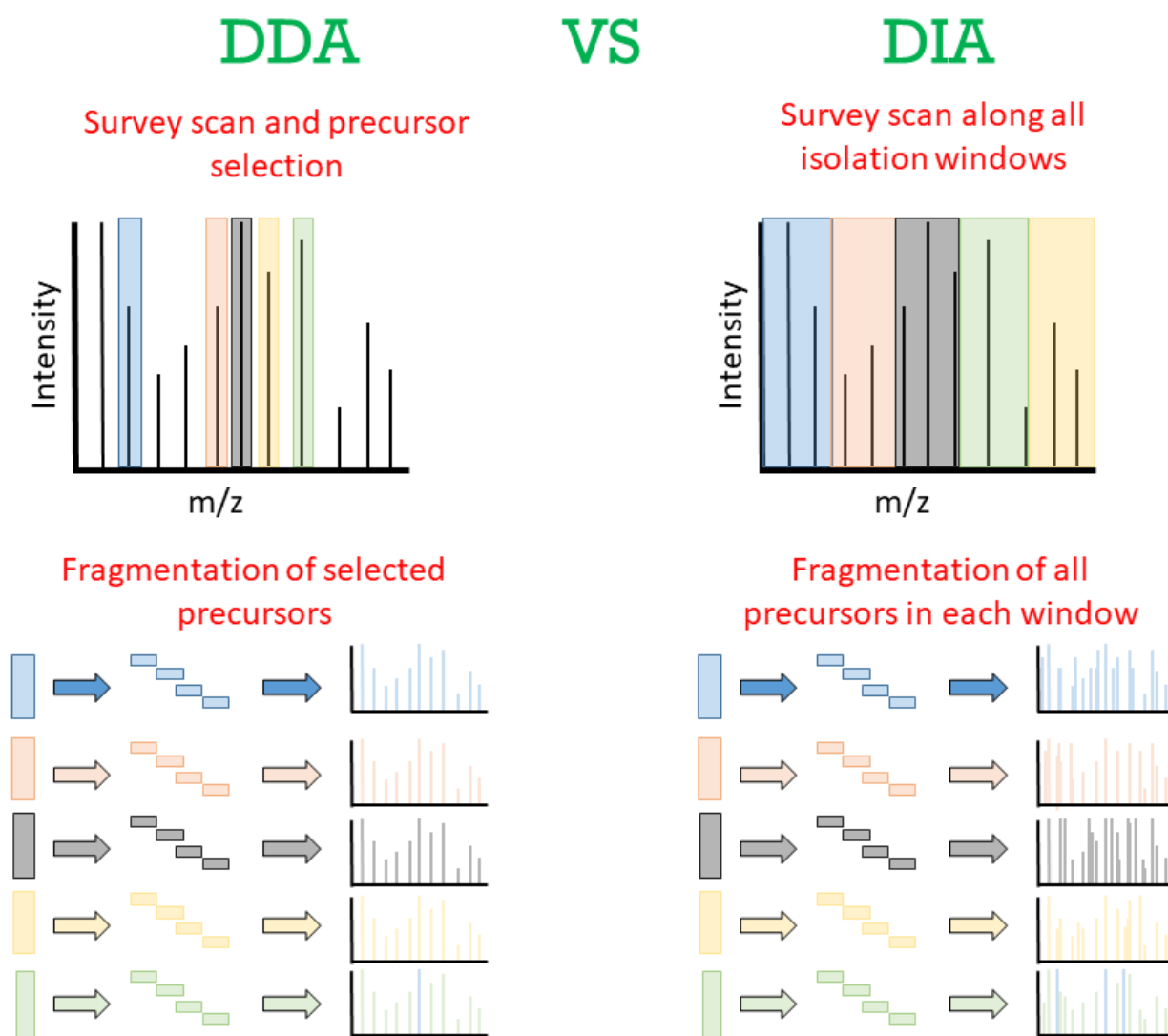


**Figure 3.** DDA and DIA. The figure shows schematically the difference between DDA and DIA MS approach. In DDA, the survey scan is needed to select the most intense precursors. These precursors will be fragmented in the MS/MS step. In DIA the survey scan hit all the precursors present in the isolation windows. All of the precursors will be fragmented in the MS/MS, originating highly multiplexed spectra

One of the most promising novel approaches is the so called staggered windows scheme, aiming at the same time to reduce the noise and complexity of the data as well as to simplify the ion library preparation [89]. Overlapping half of the windows every even cycle allows the use of a demultiplexing algorithm which is distinguishing the noise from the real peaks, cleaning the signal from the DIA runs [89,90]. The algorithm is distinguishing the noise peaks (different in the overlapping windows) from the real peaks (identical in the overlapping windows). At the same time, the concept of the DIA chromatogram library approach was

introduced. Here the library is produced directly from DIA runs, taking advantage of gas-phase fractionation (GPF). GPF is an iterative analysis of a sample over multiple and different  $m/z$  ranges (400 $m/z$ -500 $m/z$ , 500 $m/z$ -600 $m/z$ , etc.). GPF gives the chance to decrease the width of the overlapping windows, where EncyclopeDIA or Walnut software have been able to identify peptides creating a chromatogram library directly from DIA runs [91].

The staggered windows DIA approach has been developed on Orbitrap where it is successfully working, yet no one has applied it on TOFs instruments yet, probably for the higher level of noise generated by TOFs instruments or the characteristics of an algorithm developed on Orbitrap data [89,91]. Here we are proposing a successful adaptation of the staggered windows to the TOFs instruments, taking advantage of its combination with microLC ( $\mu$ LC) and last generation TripleTOF technology. Lately, the scientific community is attracted by the  $\mu$ LC thanks to technological advances. The control of the dead volumes is essential for the successful implementation of  $\mu$ LC. The latest progress of the companies in coupling the  $\mu$ LC to the MS solved the issues connected with it [92–95]. This chromatographic method though is characterized by excellent robustness and a marked simplicity in the use of the instruments compared to the nano-LC, yielding substantially better trouble-free operation and higher cycle time. The progress in the sensitivity of the instruments allows enjoying the benefits of the micro LC, as lower system pressures and shorter cycle times [96]. All of these characteristics convinced us to choose this configuration which should grant a high throughput and constant operation in the process of experimental and clinical samples.

Despite some investigation on clinical samples are still performed using a DDA approach, nowadays the DIA is starting to be more and more central, especially in the creation of proteomic datasets from the large number of clinical samples. The majority of the recent studies are still performed with a nanoLC setup excluding some exceptions adopting microflow or capillary flow setups [97–101]. Yet, the complications connected with the establishment of DIA pipelines and the evolution pace of this technique limit its application. Through the comparison of different DIA methodologies, we are showing a novel and effective combination to easily perform DIA on TOFs instruments. The introduction of  $\mu$ LC together with the development of the staggered windows method on TOFs leads to saving time and resources achieving similar results. The development of these innovative methods on our equipment grants the flexibility needed to perform research proteomics on different

experiments. Its application to the AQP's study will help proving his involvement in insulin resistant development in liver.

## 4 Aims

- Development of novel LC/MS proteomics approach suited for the analysis of both the HepG2 cells and liver clinical samples in the aspect of hepatic lipid overload and insulin resistance.
- Elucidation of the impact of the AQP9 modulation on cellular proteome HepG2-based model of lipid overload.
- Understanding the influence of AQP9 expression levels on oxidative stress homeostasis in the HEPG2-based model of lipid overload.

## 5 Material and methods

### 5.1 Cell culturing and samples collection

HepG2 cell line was bought from ATCC. The cells were cultured in Minimal Essential Medium (MEM) + Glutamax medium (GIBCO-Life Technologies) supplemented with 10% fetal bovine serum (FBS – Pan Biotech), 1% penicillin-streptomycin 5,000 U/mL (GIBCO-Life Technologies), 1% MEM Non-Essential Amino Acids Solution 100X (GIBCO-Life Technologies) and 1% Sodium Pyruvate 100 mM (GIBCO-Life Technologies).

Human liver samples were obtained from obese non-diabetic, insulin resistant and type-2 diabetic patients established based on American Diabetes Association (ADA) guidelines. They were collected during sleeve gastrectomy procedure performed at the 1<sup>st</sup> Clinical Department of General and Endocrine Surgery, Medical University of Bialystok. The consent was granted by the Medical University of Bialystok Bioethics Committee: No/ R-I-002/609/2018 & No/APK.002.107.2021.

### 5.2 Reagents and treatments

Aquaporin 9 - mycFlag (AQP9mycFlag) and Aquaporin 11-mycFlag (AQP11mycFlag) expressing plasmid were bought from OriGene (RC224567, RC208083). The transient transfection of AQP9mycFlag was performed with Fugene HD from Promega (E2311) or JetPrime from Polyplus. The transfection has been performed 48 hours before the endpoint of the experiment. The transfection with Fugene HD was performed first by mixing DNA with optiMEM and waiting 5 minutes. Then Fugene was added on top with a ratio of 3:1 Fugene:Plasmid. An incubation time of 15 minutes was applied while cells were washed with PBS and a 1:1 mix of optiMEM:MEM was added. The transfection mix was poured drop-by-drop onto the cells. The JetPrime transfection sees the dilution of the DNA in the jetPrime buffer. Then JetPrime is added with a 2:1 ratio JetPrime:DNA. After an incubation of 10 minutes at room temperature, the mix is added drop-by-drop to the cells in MEM medium. To increase the viability of the transfections methods, the medium was changed after 4h.

Lipid overload (LO) was induced by supplementing the medium of the cells for 24 hours with 0.5 mM FFA 2 : 1 oleic acid : palmitic acid, 100 $\mu$ M glycerol (Sigma G2025-100ML ). Lipid overload was supplemented (LO(+)) with 100nm Insulin (Sigma I0516-5ml). Oleic acid (Sigma O1008), palmitic acid (Sigma 76119). A 10mM FFA stock was prepared, conjugating fatty acids with Bovine serum albumin (BSA – Sigma A7030).

### 5.3 *FFAs-BSA conjugation protocol*

First Oleic Acid, Palmitic Acid, BSA and KOH were weighted. KOH was resuspended to a final concentration of 0.1M in 80% methanol. Fatty acids were dissolved separately in 10X wt./vol amount of n-hexane and KOH. N-hexane was warmed under hot water (~50°C) and added to the fatty acids tube, mixing under hot water. An equimolar amount +3% excess of 0.1KOH solution was added mixing under hot water. The solutions were mixed until uniformly dissolved. The fatty acids solutions were evaporated to dryness under a nitrogen stream in 50°C hot water bath until a film appeared. The amount of BSA to create a 10mM FFA solution was resuspended in PBS 10X. To facilitate the dissolution of BSA, the mix was heated and stirred at 50°C for 2 hours. Once the BSA solution was uniformly mixed and the fatty acids dried, the warm BSA was added to each of the fatty acids and the solution was mixed under hot water. The solutions were sonicated with Sonic&Materials sonicator at 40% amplitude, keeping the tubes in hot water (50°C). After an additional mix under hot water, the tubes were stirred at 50°C for one hour to complete the binding of the fatty acids with the BSA. 10mM FFA-BSA mix was filtered hot with 0.22µm filters in sterile conditions. Aliquots of 10mM oleic acid and 10mM palmitic acid were stored at -20°C.

### 5.4 *SDC-assisted lysis method*

Cells were washed with PBS twice and moved on ice. 150uL or 500uL LRDB lysis buffer (%5 SDC, 5mM TCEP in 50mM ABC, pH=7.8) was added to p35 or p100 respectively. The lysis was completed with a scraper and the solution was moved to a 1.5ml LoBind tube. Samples were sonicated on ice with Sonic&Materials sonicator for 3 X 20s at 50% amplitude. If some samples did not reach complete solubilization the procedure was repeated. The samples were then reduced heating for 30 minutes at 60°C in a Eppendorf Thermoblock. Samples were then cooled on ice and the Thermoblock cooled to 25°C. Iodoacetamide was then added to the samples to a final concentration of 15mM. Samples were incubated with IAA for 30 minutes at 25°C in the dark. Finally, the samples were centrifuged for 10 minutes at 14.000g at RT and the supernatant was moved to a new Eppendorf tubes. The protein concentration has been measured in 10X diluted aliquots using a BCA assay kit (BCA-1, Sigma-Aldrich). The concentration of the samples was normalized to 2.5 µg/µL using LDB buffer (5% SDC in 50mM ABC, pH=7.8). To proceed with the digestion, samples were diluted 10X using ABC buffer (50mM ABC, pH=7.8), lowering the concentration of SDC to 0.5%. Trypsin/Lys-C mix was added with an enzyme:proteins ratio of 1:25. The mix was incubated for 16 hours at 37°C in a Thermoblock shaking at 600rpm.

After digestion TFA was added to the samples at a final concentration of 0.5% to acidify the samples and ethyl acetate was included with a 1:1 ratio (vol:vol) to perform the phase extraction of SDC. The SDC extraction was performed through a vortexing of the samples for 1 minute. The phases were separated with centrifugation for 5 minutes at 14.000g. The upper phase was then discarded and the ethyl acetate extraction was repeated twice. After this, the samples were placed in a Thermoblock for 20 minutes at 60°C shaking with the caps open to allow the evaporation of residual ethyl acetate. The samples were then processed with the MCX ZipTip protocol for peptides desalting/cleaning.

### 5.5 MCX zip-tipping for peptides desalting/cleaning

MCX zip tips were prepared in-house with a maximum capacity of 30µg of peptide retention each. Precisely 3-stacks of MCX membrane cutouts were packed gently inside 200µL clean tips till constituting a solid filter a few mm far from the exit of the tip. Tips were mounted on an open Eppendorf using a rubber gasket. The Zip Tips were conditioned in 2 steps. The first one consisted in passing 50µL of pure LC/MS ACN centrifuging the tips at 1.700g for 1 minute. The second in passing 50µL of pure LC/MS water centrifuging at 1.700g for 1 minute. To equilibrate the ZipTips 50µL of 0.1% TFA in LC/MS water was added twice to the tips and centrifuged at 1700g for 1 minute. Then 25µg of digested peptides were loaded on the ZipTips and bound to MCX membrane with low-speed centrifugation, at 800g for 2-3 minutes, ensuring that all the sample was loaded correctly. The samples were then washed twice with 50 µL of wash buffer composed of 0.1% TFA and 2% ACN at 1.200g for 3 minutes. For the elution phase, Zip Tips were then moved onto a new clean LoBind Eppendorf and the peptides were eluted from the disks with 20µL of 50% ACN/5% ammonia hydroxide in water and centrifugation at 1.200g for 3 minutes. The elution was performed three times. The eluates were dried using a Labconco Vacuum Concentrator at 45°C and 0.05 atmosphere residual pressure for 60 minutes. The dried peptides were resuspended in 45uL of Acidic Sample Solvent (ASS: = 2% ACN, 0.2% TFA, 0.001% ZTS) and 5uL of iRT peptides (Biognosys) to a final concentration of 0.5ug/µL. Samples were moved in AS glass vials and 10µL equivalent to 5µl of peptides were injected into the µLC system. The samples dedicated to the HpH fractionation were resuspended in basic sample solvent (BSS; 100mM ammonium hydroxide, 2% ACN, 0.001% Zwittergent 3-16).

## 5.6 MS acquisition

Libraries were created from pooled samples (wild type, LO, LO + I, LO + I + AQP9). Proteins were digested with SDC-assisted method and desalted with MCX ZipTip prepared following the appropriate protocols [102–105]. For the traditional ion library generation we used the High-pH (HpH) peptide fractionation with fraction concatenation approach (A - 10mM NH<sub>4</sub>OH in H<sub>2</sub>O; B -10mM NH<sub>4</sub>OH in 90% ACN). The resulting 24 fractions were pooled to final 8, using a concatenation scheme to optimize the concentration and distribution of peptides in every combined fraction. The HpH fractionation was performed on Dionex 3500RSLC equipped with C18 Waters XBridge Peptide BEH Column (300Å, 3.5 μm, 1 mm X 150 mm). Subsequently, the pooled fractions were evaporated in a Labconco Vacuum Concentrator at 0.05 residual pressure and 45° degrees overnight. Samples were resuspended in an acidic sample solvent (ASS, 2% ACN, 0.2% TFA, 0.001% ZTS). Both the fractions and the digested samples were run on Eksigent nLC425 μflow LC with trap-load setting and the following gradients: A - 2% ACN, 98% H<sub>2</sub>O and 0.2% FA; B – 90% ACN, 10% H<sub>2</sub>O and 0.2% FA. The flow was set to 5 μL/min and loading has been optimized to keep a real 1h sample-to-sample run time and 24 samples/day throughput. The LC was connected to a Sciex TripleTOF 6600+ through OptiFlow TurboV source. The injection cycle included 4-minute on-line trapping/desalting on Waters nanoEase M/Z Peptide BEH C18 trap (130Å, 1.7 μm, 300 μm X 50 mm) using A buffer. Trapped peptides were eluted and resolved by a binary reversed-phase gradient was applied on a 15cm column nanoEase M/Z Peptide BEH C18 Column (130Å, 1.7 μm, 300 μm X 150 mm). An identical gradient was used for both the VWW, STW and DDA runs. MS cycle speed was normalized in all the methods to yield approx. 9 points per peak. We decided to turn to the microLC system because of the multiple advantages offered by this system

### 5.6.1 Data-dependent analysis (DDA)

DDA runs for the method development and the HpH libraries were completed with a TOP 30 approach. MS1 scan with 250ms accumulation time covered 400-1200 m/z, MS2 fragmented the 30 most intense precursors, with charges between 2 and 5. Precursors threshold was set to 150cps, mass tolerance was set to 50mDa, excluding them for the next fifteen seconds. The equalization of the peptide fragments between DDA and DIA was obtained uniforming the CE equations and increasing the CE spread. The following CE equation was applied in DDA and DIA methods:  $CE = [0.0625 \text{ (slope)}] * [\text{precursor (m/z)}] + [-10.5 \text{ (intercept)}]$ .

## 5.6.2 Data-independent analysis (DIA)

DIA analysis with variable windows was performed using three different MS2 schemes (100,75,50 VWW). DIA with staggered windows width was performed using three different MS2 schemes of overlapping windows (50,40,25 STW). In VWW, MS1 accumulation time was 250ms covering 400-1200 m/z. MS2 accumulation time for 100, 75 and 50VWW was of 25, 35 and 50ms. SwathTuner tool for R was used to determine the variable windows based on the MS1 of a preliminary DDA run. Windows placement was improved with Skyline considering the forbidden zones. STW MS1 accumulation time was kept at 250ms covering the same m/z region. 50 STW, 16m/z each, had an MS2 collection time of 25ms. 40STW, 20m/z each, had an MS2 collection time of 31ms. 25STW, 32m/z each, had an MS2 collection time of 50ms. GPF chromatogram libraries were produced from 8GPFs of 100m/z using two additional STW schemes. 2m/z and 4m/z wide overlapped windows. In 2m/z windows, MS1 scan accumulation time was 250ms, MS2 scans were collected for 25ms on a range 100-1800 m/z. In 4 m/z windows, MS1 scan accumulation time was 250ms, MS2 scans were collected for 50ms on a range 100-1800 m/z. Windows placement was improved with Skyline considering the forbidden zones [89,106].

MS cycle time was normalized to 2.8 seconds in all the approaches, obtaining around 4-5 MS cycles at FWHM for each chromatographic peak. To avoid variability problems all the methods used the same settings for chromatography, source and the following MS/MS connected parameters. MS1 mass range 400-1200 (except GPF DDA runs), MS2 declustering potential - 80, MS1 collision energy - 10V, MS2 mass range 100-1800, MS2 declustering potential - 80, MS2 CE spread - 15, MS2 performed with rolling collision energy (DDA), MS2 Ion release delay - 66, MS2 - Ion release width - 24, MS2 mode - high sensitivity.

## 5.7 Data analysis

### 5.7.1 Ion chromatogram libraries

8 HpH-fractionated samples were run in DDA to create the specific library for VWW. 8 GPF-fractionated samples were run in DIA (2m/z and 4m/z) to create the specific library for STW. All the libraries were supplemented with 3XDDA runs creating the hybrid version of them. DDA runs covering the full 400-1200m/z addition to the GPF libraries allowed for an improved iRT based retention time calibration. Libraries were built with Spectronaut version 15.4.210913.50606(Rubin). Files were searched with the build-in Pulsar engine against Homo sapiens Uniprot reference proteome FASTA file (UP000005640\_9606, one sequence per

protein) using standard settings with the following minor modifications: Trypsin/LysC - specific digestion with cut at P, carbamidometylation of C as fixed modification, deamidation of Q or N, acetylation of N-terminal and oxidation of M as variable modifications, peptide length between 7 and 35 amino acids, max 5 variable modifications and max 2 missed cleavages. All the STW were demultiplexed with the algorithm based on Amodei et al. [89] MS1 and MS2 spectra were mass-calibrated by Pulsar engine with the dynamic calibration algorithm. Between 3 and 6 most intense fragments of b or y type, with an m/z between 300 and 1800 m/z and at least 3 amino acids were included in the chromatogram libraries. FDR cutoff for precursors, peptide-spectrum matches and proteins was set at 1%. Spiked-in iRT peptides and deep learning-assisted iRT regression were used for RT calibration and RT window calculation.

### 5.7.2 DIA analysis

The same Spectronaut standard settings were applied for the analysis of VWW, STW and direct-DIA runs with minor modifications. MS1 and MS2 ion chromatogram from VWW and STW were extracted using dynamic mass calibration based on max ion intensity, dynamic mass tolerances and iRT-based RT extraction window. The results were searched with experiment specific ion libraries. FDR was calculated with target-decoy approach using mutated sequence. 1% Q value cutoffs (corresponding to FDR thresholds) was chosen for precursors and peptides, 5% for proteins run-wise and 1% for proteins experiment-wise. Runs were analyzed with settings analogous to the one used in library-based analyses. Quantification was performed with the use of MaxLFQ algorithm of Spectronaut. Per-sample peptide quantity (minor group) was calculated as a mean of the peak areas of top 3 MS2 fragment ions, whereas protein quantity (major group) was expressed as a mean of top 3 peptides.

### 5.8 Bioinformatics analysis with Lasagna 2.0

The bioinformatics prediction of the transcription factor binding sites has been performed using LASAGNA-Search 2.0: Searching for transcription factor binding sites (TFBSs). The input model for the prediction selected was TRANSFAC TFBSs, part of the LASAGNA aligned model section. TRANSFAC TFBSs uses precomputed transcription factors model from the TRANSFAC public database aligned by the LASAGNA algorithm. The promoter sequence input was set to retrieve the promoter sequence inserting the species and the name of the protein of interest. The results were filtered setting a Cutoff p-value of 0.001. The tool is

providing the binding site's predicted position and strand. To evaluate the prediction reliability, the score, p-value and E value are shown by the tool [107,108].

#### *5.9 Lipid droplets staining with Oil red O*

The medium was removed and cells were washed with TBS-cyt buffer (20mM Tris, 154mM NaCl, 20mM EGTA, 2mM MgCl<sub>2</sub>, pH 7.4). Cells were fixed with 4% paraformaldehyde for 20 minutes at RT. Cells were washed 4 times and then 60% isopropanol was added for 5 minutes right before the staining. The stock solution of Oil red O (0.5 % Oil Red O in 100 % IPA) was diluted at 6:4 in deionized H<sub>2</sub>O to get a working solution in 60 % IPA, 40 % H<sub>2</sub>O. The working solution was left standing for 10 minutes and filtered directly before use. The staining was applied to the cells for 15 minutes and then the wells were washed 5 times with TBS-cyt. Coverslips were mounted using Mowiol 4-88 from Sigma. Slides dried overnight at RT and acquired.

#### *5.10 Lipid droplets staining with Bodipy 493/503*

The medium was removed and cells were washed with TBS-cyt buffer. A 1 $\mu$ M Bodipy staining solution was prepared in PBS. The cells were incubated with the staining solution for 15 minutes at 37°C. Cells were then washed three times with TBS-cyt. 4% paraformaldehyde was used for 20 minutes at RT to fix the cells. After four TBS-cyt washes, coverslips were mounted with Mowiol 4-88. Slides dried overnight at RT and acquired. The excitation/emission maxima are 493/503nm.

#### *5.11 Apoptosis assay*

Apoptosis was evaluated using the CellEvent Caspase-3/7 Green Detection Reagent from Invitrogen (C10723). The medium was removed and cells were washed with PBS. The staining solution was prepared at 1 $\mu$ M concentration in PBS with 5% FBS to reduce the background noise. Cells were incubated with the staining solution for 30 minutes at 37°C. Cells were then washed twice with PBS and fixed with 4% paraformaldehyde for 20 minutes at room temperature. Coverslips were mounted using Mowiol 4-88. Slides dried overnight at RT and acquired. The excitation/emission maxima are 502/530nm.

#### *5.12 Microscope short time-lapse experiments*

Microscope short time-lapse experiments were performed on Leica DMI8. Cells carrying HyPer1 or HyPer 7.2 in different locations were acquired exciting the probe at 405 nm or 488 nm and reading the emission always at 520nm. The two ex/em combinations were acquired alternatively every second for 5 minutes, collecting 150 images for each channel. After 1

minute from the start of the acquisition  $\text{H}_2\text{O}_2$  or insulin was added and after 4 minutes DTT was added. HyPer is a genetically encoded ratiometric probe able to respond to the hydrogen peroxide accumulation with the change in fluorescence emissions. The ratio between 488/520 and 405/520 grants the independent was used to estimate  $\text{H}_2\text{O}_2$  emissions. Novel HyPer7.2 ratiometric probe offers improved brightness of emission and better fluorescence independence from intracellular pH variations.

Cells were cultured in p35 dish carrying a 24mm slide. Before the acquisition, the coverslip was moved into Attofluor chambers (ThermoFisher). Cells were washed twice and incubated 10 minutes in 500 $\mu\text{L}$  of Ringer buffer (RB = 140mM NaCl, 2mM  $\text{CaCl}_2$ , 1mM  $\text{MgSO}_4$ , 1.5mM  $\text{K}_2\text{HPO}_4$ , 10mM glucose and 10mM HEPES (Sigma H4034), pH 7.4). A 6X solution of 300 $\mu\text{M}$   $\text{H}_2\text{O}_2$  was prepared in RB and 100 $\mu\text{L}$  was added after 1 minute of acquisition bringing the concentration to 50 $\mu\text{M}$ . In the experiments involving insulin stimulation, 6X insulin stock (600nM) was prepared and added after one minute to a 100nM final concentration. A 7X DDT 35mMDTT stock solution was prepared in RB as well, and 100 $\mu\text{L}$  was added at the fourth minute of acquisition, to a final concentration to 5mM.

#### *5.13 Microscope long time-lapse experiment*

Microscope long time-lapse experiments were performed on Leica DMI8. Cells carrying HyPer in ER lumen were acquired by exciting the probe at 405 nm or 488 nm and reading the emission at 520nm. Bright field, 405/520nm and 488/520nm were acquired every 15 minutes for 20 hours. Cells were prepared as described for the short time-lapse experiment, but they were incubated with the lipid overload medium. The acquisitions were performed overnight in a controlled environment, keeping the constant temperature to 37°C and  $\text{CO}_2$  to 5%. The autofocus was set to calibrate itself every cycle on the bright field image. This allowed the measurement of  $\text{H}_2\text{O}_2$  accumulation in the ER of cells under lipid overload with extreme accuracy.

#### *5.14 Digitonin treatment*

Cells were permeabilized with digitonin to investigate the presence of a reductive shield around the ER of HepG2 cells. Digitonin (Sigma D141) was solubilized by heating at 5% concentration (approx. 50mg/ml) in water to 95-98°C and cooling to RT. To disrupt the plasma membrane keeping the ER membrane intact we diluted the stock solution to a working solution of 40 mg/ml. The working solution was used at 1:500 concentration for 1 minute, promoting the release of the cytoplasmic protein content while maintaining the intracellular

membrane structure unaltered. Samples were washed twice in RB and incubated for 5 minutes in RB before the acquisition.

#### *5.15 Microscope images analysis*

Analysis of the images was performed through FIJI open-source software. Image sequences were imported and filtering for the condition and wavelength (405nm or 488nm) was applied. Free-hand Region of Interests (ROIs) were designed on a total of 25 cells/slide. Mean gray value was measured and results were pasted in an excel sheet for both the excitations. The ratio between 488 stimulated and 405 stimulated gives the oxidative state of the probe and it was converted to fold changes (FC) to facilitate the comparison between the different cells. Medians were imported in GraphPad Prism 9, where 2 experiments with 3 replicates per condition were collected. Mean + SEM is shown for every timepoint of the plot.

Microscope images were prepared on FIJI. First, the background noise has been isolated defining a threshold manually. The look-up table (LUT) was changed to promote the visualization. In the case of multiple channels acquired, the image's brightness was modified to ensure its similarity between the channels. Images were merged modifying the LUT.

#### *5.16 Statistical analysis*

Statistics analysis for microscope experiments was performed in Graphpad Prism 9. Results are expressed as mean +/- SEM. Statistical significance for the comparison of more than two groups has been calculated using one-way ANOVA with post hoc test. Statistical analysis of proteomics data has been performed in Biognosys Spectronaut as described in materials and methods section. Pathway analysis was performed with Ingenuity Pathway Analysis Software (IPA) as described in methods section.

#### *5.17 R graphs*

Venn diagrams were designed with the BioVenn package for R [109] starting from the reports exported from Biognosys Spectronaut. Volcano plots were designed using the EnhancedVolcano Bioconductor package for R [110]. R version 3.6.3.

## 6 Results

### 6.1 Data Independent Acquisition (DIA) development I: Variable windows width

The following method optimization steps were performed prior to the analysis of the experimental samples:

- the optimization of ESI source parameters using PepCalMix peptide calibration standard
- the optimization LC gradient using HeLa protein digest standard
- the optimization of collision energy parameters to improve the matching between DDA chromatogram library MS2 spectra and DIA methods MS2spectra
- the introduction and optimization of the variable windows scheme (STW) and comparison with currently standard variable windows width approach (VWW)

**Table I.** OptiFlow TurboV **source optimization parameters.** Sciex TripleTOF 6600+ source parameters optimization. Lines represent the different parameters which were modulated to obtain highest response. Each column is a different optimized setting.

	<b>STD</b>	<b>GAS</b>	<b>OPT</b>	<b>HIGH</b>
<b>GS1</b>	35	25	25	20
<b>GS2</b>	15	15	15	15
<b>CUR</b>	25	30	30	25
<b>ISVF</b>	4500	4500	4500	5000
<b>TEM</b>	0	0	75	150

GS1=GAS1, GS2=GAS2, CUR=Curtain gas, ISVF= IonSpray Voltage Floating, TEM=Temperature

The source parameters of the TripleTOF MS, optimizing the Gas1, Gas2, Curtain gas, temperature and voltage as described in **Table I**. Decreasing the Gas1, increasing the curtain gas and the temperature improved the signal and signal-to-noise ratio for the peptide calibration mixture (PepCalMix). The selected configuration is the best compromise between signal improvement and equipment usage. **Figure 4.** shows the improvement of the signal with optimized gas (GAS), optimized gas and temperature (OPT) and optimized temperature and voltage (HIGH) compared to the non-optimized (STD)one, as expected. The OPT and HIGH options show the best results.

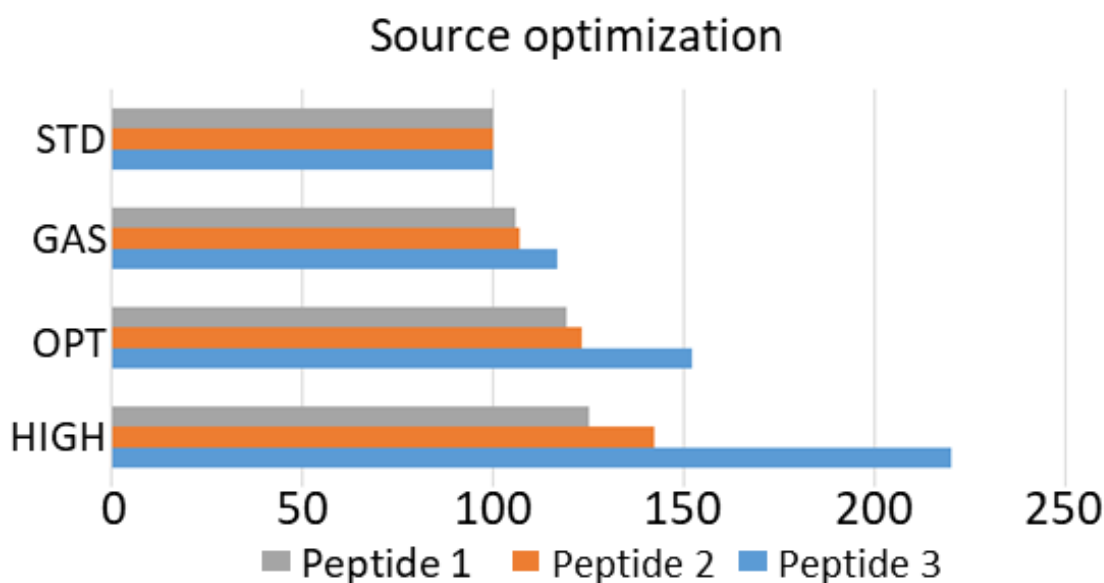


**Figure 4.** The figure shows the area under the curve for three exemplificative peptides with the different optimization steps compared to one with the STD source settings.

**Table II. LC gradients optimization.** Variations of the %ACN in an analytical run lasting 57 minutes.

Min	%ACN						
	V1	V2	V3	V4	V5	V6	V7
0	2.07	2.07	2.07	2.07	2.07	2.07	2.07
2	2.97	3.87	4.05	4.05	4.5	4.95	4.5
40	27	27.9	28.8	28.8	28.8	28.8	27.9
45	36	36.9	37.8	37.8	40.5	40.5	40.5
47	81	81	81	81	81	81	81
50	81	81	81	81	81	81	81
51	2.07	2.07	2.07	2.07	2.07	2.07	2.07
57	2.07	2.07	2.07	2.07	2.07	2.07	2.07

V1...V7=Version 1...Version 7, %ACN=% Acetonitril

Once obtained the best setting for the source, the LC gradient was optimized next. The gradient was designed for 1 sample per hour and 24 samples per day throughput, taking advantage of the higher speed offered by the  $\mu$ LC setup. In RP-LC the elution of the peptides is linked to the percentage of organic solvent (acetonitrile, ACN) flowing through the column.

The first peptides eluted are the most hydrophilic ones. Increasing the % of ACN more and more hydrophobic peptides will be eluted.

As described in **Table II and Fig.5**, the slope of the gradient was changed by altering the % of acetonitrile (ACN), the organic solvent used for the elution. The option which gave us the best results in terms of peptide identifications, number of identified proteins and tighter peaks (as described by full width at half maximum (FWHM)) was the V7 gradient. The 2% of ACN starting concentration helps to retain peptides on trap during loading step of the trap-elute method, without sacrificing hydrophilic peptides. First step consists of the loading of the sample to a short trap column where it is washed by the low % of ACN, flushing salts and impurities. Increasing the % ACN the sample peptides are eluted from the analytical column. The first short step from minute 0 to 2, with %ACN increasing to 4.5 was designed to improve the resolution of highly hydrophilic peptides, otherwise appearing in a single peak during the gradient start. The elution gradient is divided into 3 steps. From minute 2 to 40 consisting of a progressive increase of %ACN from 4.5 to 27.9, grants the best separation of the bulk of the sample peptides, followed by a second shorter, from minute 40 to 45, with %ACN reaching 40.5.

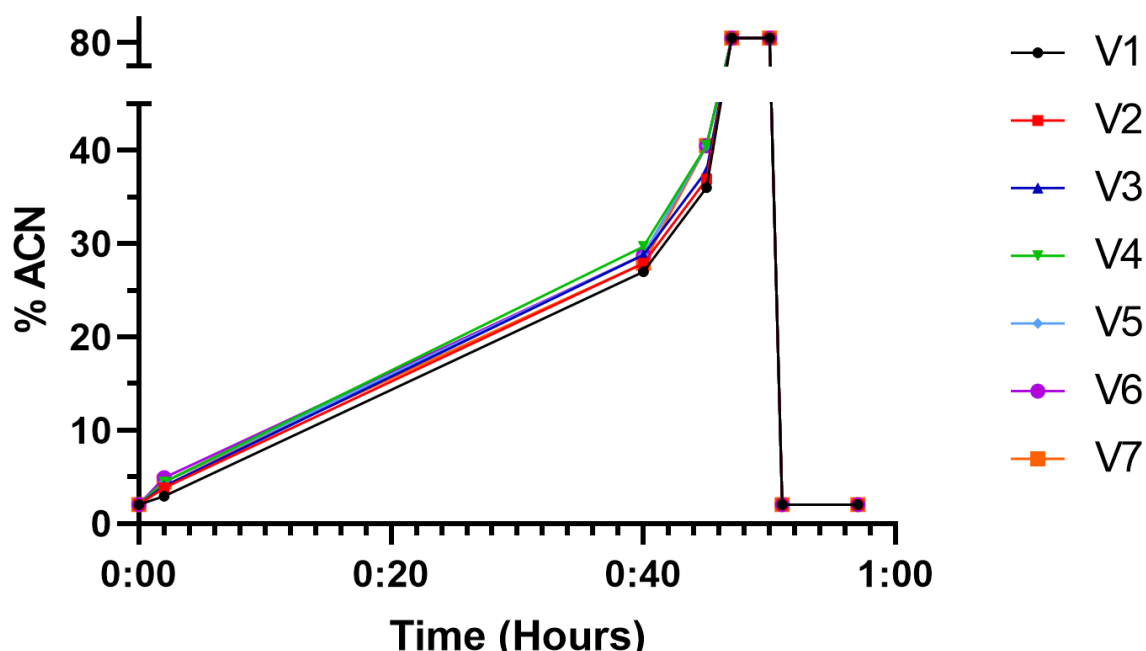


**Figure 5. LC gradients comparison.** The picture shows the % of ACN in the gradients tested. Y axis is divided in 2 to ensure a major definition of the region 0-40% ACN. On X axis there is the gradient time in hours.

The increased steepness in this part of the gradient permits the elution of the most hydrophobic peptides. Subsequently, the column is cleaned by increasing the %ACN to 81% for 3 minutes. The last 6 minutes are needed to re-equilibrate the column at 2%ACN, while another sample is prepared for the injection in the autosampler.

**Table III. CE equations.** The two tables show the CE equations for the different charge states. On the left are listed the ideal CE equation for an optimal fragmentation of the peptides. On the right the modified version, showing a uniform equation throughout all the charge states leading to a milder fragmentation, especially in DDA.

Ideal CE equations			Milder CE equations		
Charge	Slope	Intercept	Charge	Slope	Intercept
Unknown	0.049	-1	Unknown	0.0625	-10.5
1	0.05	5	1	0.0625	-10.5
2	0.049	-1	2	0.0625	-10.5
3	0.048	-2	3	0.0625	-10.5
4	0.05	-2	4	0.0625	-10.5
5	0.05	-2	5	0.0625	-10.5

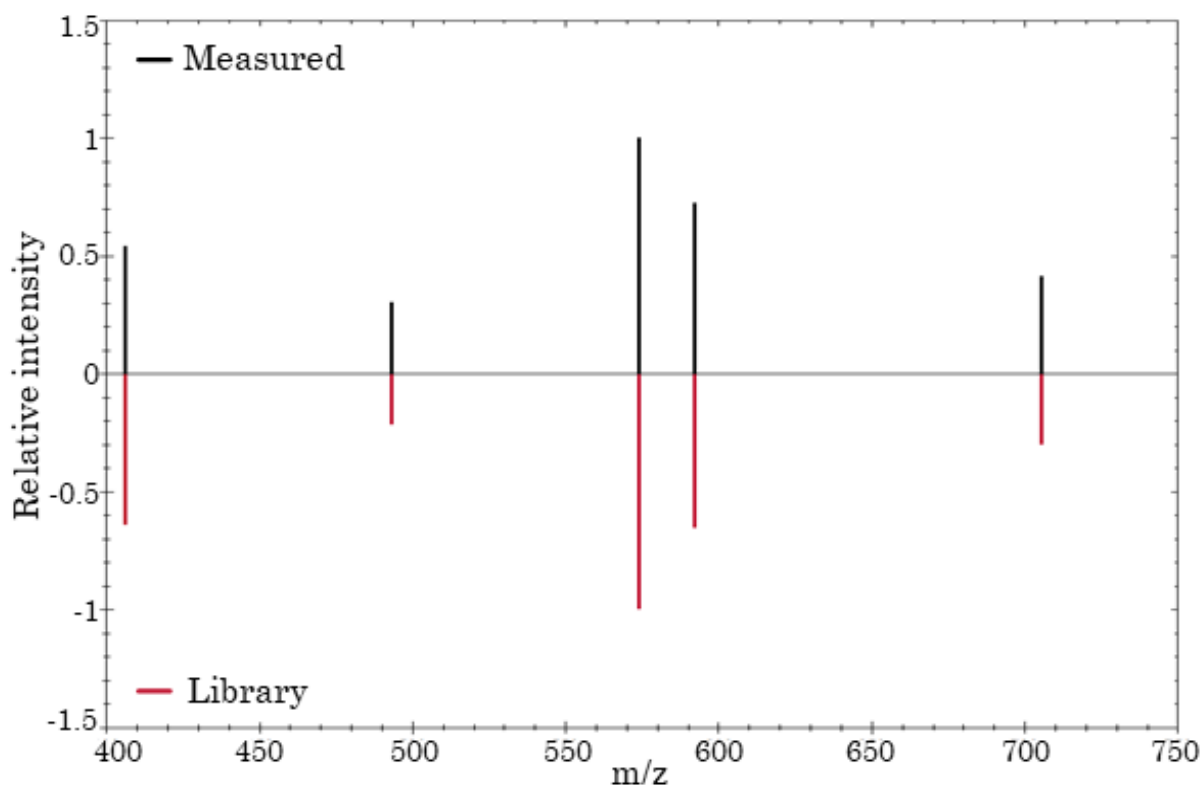


**Figure 6. Ion Spectrum Match.** Representation of the matching fragmentation pattern between DDA (Red, Library) and DIA (Black, Measured) approaches using the milder and uniformed CE equation. The type of fragments is the same and the intensity is almost identical, reducing at the minimum the difference between DDA and DIA spectra.

The collision energy (CE) equation in TripleTOFs instruments defines the energy applied to the CID event based on  $m/z$  of the precursor ions. Different CE equations can be set for the different charge states to compensate for the increased energy needed for the fragmentation of multiply-charged high  $m/z$  peptide ions. In Table III presents the equation optimized for the best peptide fragmentation (first column) in DDA mode, which improves fragmentation of long-sequence, multiply-charged peptides. In DIA, the identifications of ions in the sample runs rely on the DDA MS2 spectral library, previously collected in DDA mode. Keeping the ideal CE settings, the different nature of DDA and DIA techniques will bring to the production of different fragmentation patterns starting from the same ion. Thus, with the ideal CE settings, we can produce a richer library given the optimal fragmentation performed. However, this does not translate into more identified peptides in the DIA runs. Some of the ions in the library are not recognized in the DIA runs because the different fragmentation pattern applied in the windowed fragmentation scheme makes the matching difficult. Using a DIA-optimized CE equation (Table III) and applying it to all the charge states in DDA and all the isolation windows in DIA we are overcoming this issue. The MS2 product ion pattern and intensity obtained from both DDA and DIA runs will be similar, granting a higher probability of the identification of complex MS2 spectra and increased coverage of the library. Figure 6

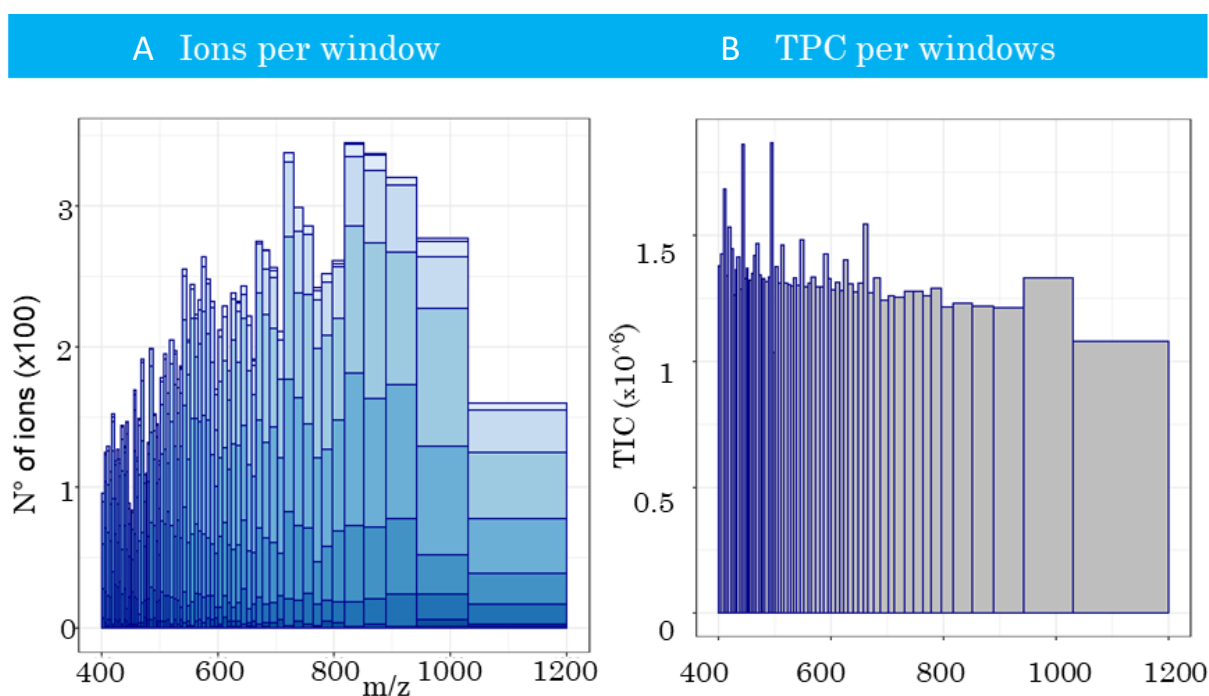


**Figure 7. Swath Tuner variable windows.** Panel A describes the distribution of ions per windows. Panel B describes the distribution of TIC (or TPC in this case) per windows

shows an example of the similarity of the fragmentation pattern with the modified CE equation, supporting our approach.

The main difference between DDA and DIA is fragmentation: the former selects the top 10 to 30 most intense precursor (MS1) ions for fragmentation, the latter fragments every precursor (MS1) ion isolated in the predefined mass window. This explains the non-stochastic nature of the DIA, with the drawback of highly complex MS2 spectra. The process of fragmenting of multiple precursor ions yields very complex product (MS2) ion spectra, whose interpretation is troublesome. As it is currently impossible to apply very narrow windows (approx. 1m/z) which cover full MS1 mass range of the analysis under the reasonable cycle time, the full MS1 m/z range is divided into wider mass windows where all the relevant ions undergo CID fragmentation. The traditional DIA approach, divides MS1 space into windows of the same size (approx. 10-50m/z wide, equipment dependent), while a more advanced approach is based on variable windows. The variable windows are designed to give more time to the instrument to analyze ions in m/z regions with highest ion densities. In VVW approach the windows are smaller and more numerous to increase the hits, with larger windows in the regions populated by fewer ions. The SwathTuner, an R-based tool was used for the calculation of the proper windows distribution, based on the TIC (or total peptide chromatogram) of a sample acquired previously in DDA mode. The **Figure 7** shows show the variable dimension of the windows equilibrated the number of ions per window, but especially the TIC (or TPC – what is TPC - describe) per window.

## 6.2 *Untargeted proteomics analysis of human liver samples*

The DIA proteomics approach for the untargeted analysis was first applied to a limited number of samples with the goal of possible identification and quantitation of aquaporins and the proteins involved in the hepatic lipid metabolism. The human liver samples were obtained from obese patients undergoing bariatric surgery and consisted of: obese non-diabetic patients (ND), obese with impaired glucose tolerance (IGT), and obese with type 2 diabetes (T2D). Initial study involved 3 patients for each condition. High pH fractionation (HpH fractionation) was used to fractionate the samples and increase the coverage of the peptides present in a single sample. The 24 fractions are then concatenated into 8 final fractions. The scheme of concatenation, pooling together fractions collected at different retention times, ensures an equilibrated peptide distribution upon injection and acquisition in DDA mode. We created a High pH fractionated library from ND, IGT and T2D mixed samples and we concatenated the fractions with a fixed scheme as shown in **Figure 8a**. This is confirmed by

**Figure 8b**, showing the distribution of peptides and resulting proteins among the 8 pooled fractions. This approach ensures the maximal coverage of proteins and peptides in the samples, distributing peptides with similar characteristics in different fractions. Keeping the optimized settings described before, we have been able to build a library covering 4433 hepatic proteins.

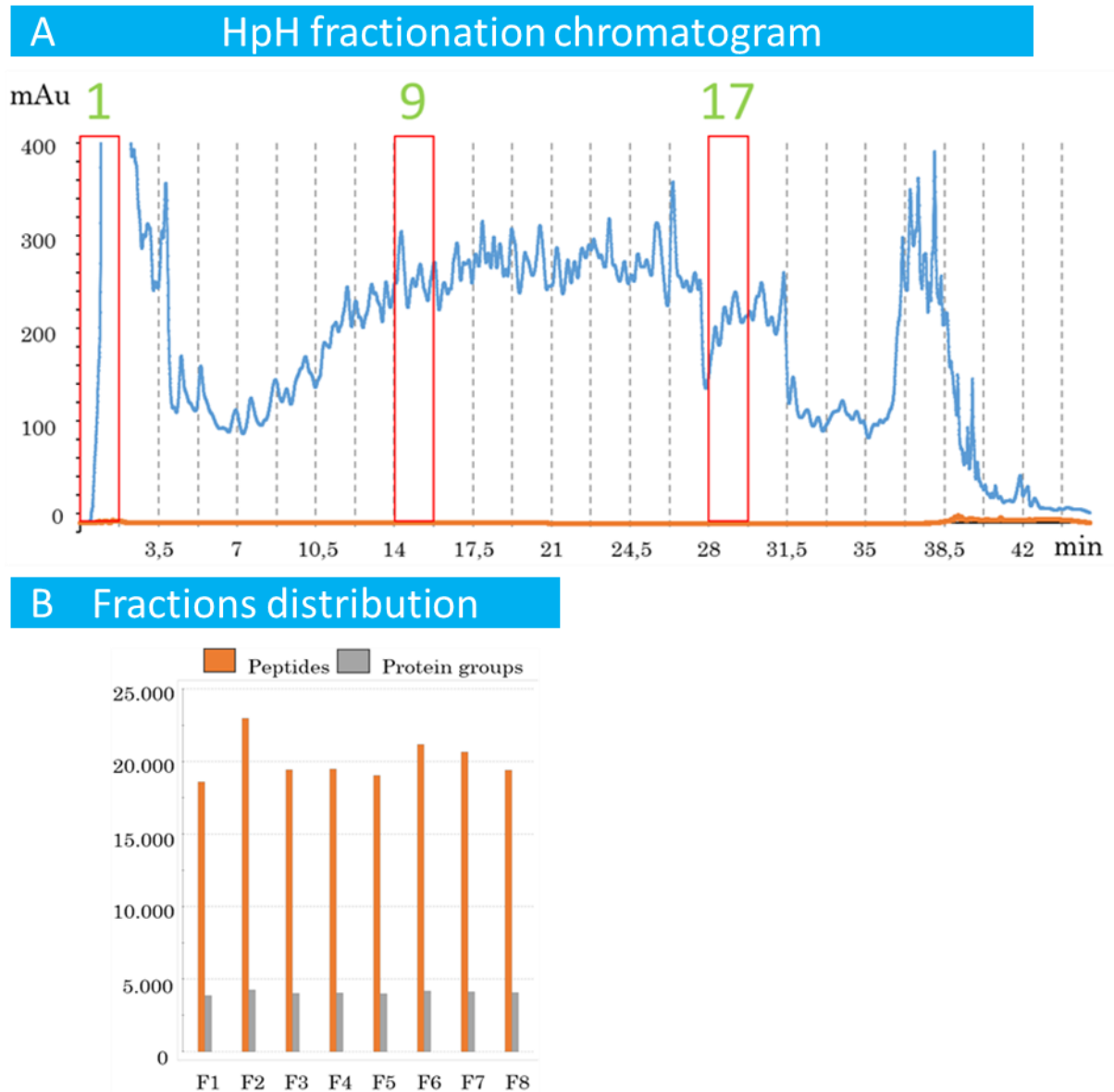


**Figure 8. HpH fractionation.** Panel A representatively shows the HpH chromatogram from a ND sample. The red boxes indicate the pooling scheme adopted for the fraction concatenations (1-9-17, 2-8-18, ...). Panel B shows the peptides and proteins identified with DDA in the 8 pooled fractions.

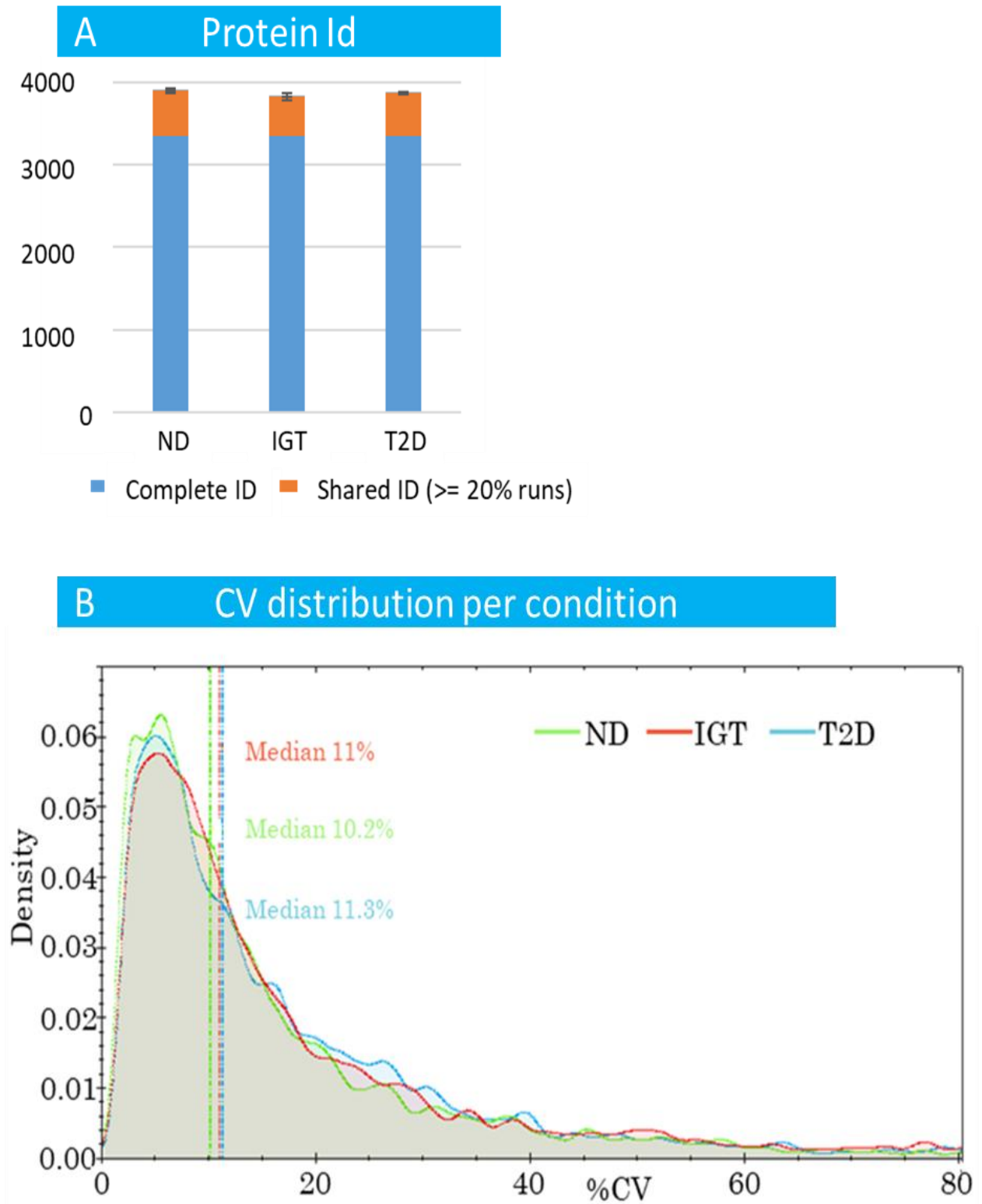


**Figure 9. Identifications and CVs of DIA analysis on human liver samples.** Panel A shows the identified proteins in each group. Proteins identified in all the samples of the group are represented in blue. Proteins identified in at least 20% of the samples (1 in this case) are depicted in orange. Panel B shows the CV distribution per condition. The coloured lines represent the distribution of the CV, the dotted lines indicate the median.

Each sample has been run with 64VWW DIA scheme, reaching an impressive library coverage of around 90% for ND, IGT and T2D with almost 4000 proteins identified at 1% FDR. Despite patient heterogeneity, the majority of the identified proteins were shared between the groups. The in-group proteins variability showed excellent results (**Figure 9**). **Figure 9b** shows the distribution of the coefficient of variation (CV) of the proteins per experimental condition. Contrary to the DDA approach, the non-stochastic nature of DIA analysis ensured a high reproducibility between samples and groups. The median CV for identified proteins measured with DIA approach was 10% with  $\frac{3}{4}$  of the proteins displaying CV below 20%.

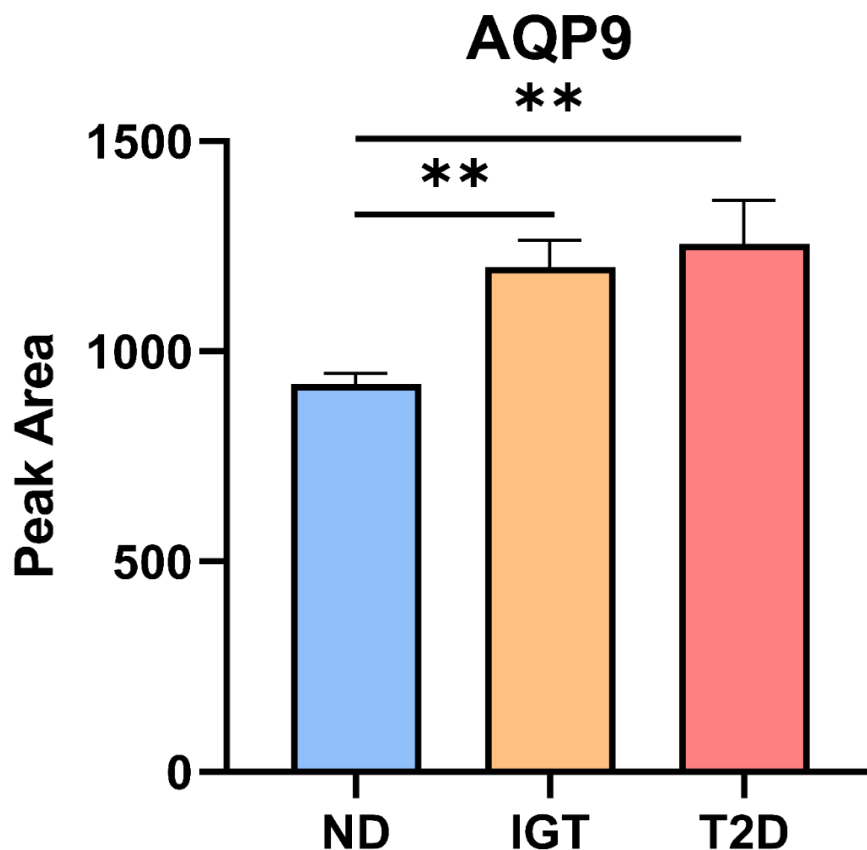


**Figure 10. AQP9 expression levels in human liver samples.** The figure shows the expression of AQP9 in ND (Blue), IGT (Orange) and T2D (Red) patients. The quantification is based on the peak area of the three best peptides. N=3, mean +SEM. Multiple t-test applied, \*\*=0.005

From the biological point of view, it has been performed the analysis of these few samples as an exploratory work to identify possible new targets in liver insulin resistance and type 2 diabetes. The focus was mainly on the analysis of diacylglycerol (DAG) accumulation-

connected and oxidative stress pathways, as their role in these processes is well-characterized. The main finding in this experiment was aquaporin-9 (AQP9), a protein that being both an H<sub>2</sub>O<sub>2</sub> and a glycerol transporter can potentially link both pathways (**Figure 10**). DIA approach allowed for the detection of AQP9 upregulation in IGT patients, which is also shown to be similar in T2D patients. The quantification based on the selection of the best three peptides shows an increase in the protein levels of around 30% compared to the ND. N-terminal acetylation is a common modification in eukaryotes, involving a large variety of proteins [111]. Also, AQP9 appears to be acetylated in obese non-diabetic subjects. Interestingly, we notice an increase of the N-terminal acetylated peptide both in the two stages of the disease, IGT and T2D.

AQP9 upregulation was accompanied by increased expression of fatty acids-binding proteins (FABPs), the main fatty acids transporters in liver cells. As AQP9, both the FABP4 and FABP5 are upregulated in IGT patients (**Figure 11**). The coordinated upregulation of glycerol and fatty acid transporters in IGT patients supports the hypothesis of cooperation in the DAG accumulation in the liver.

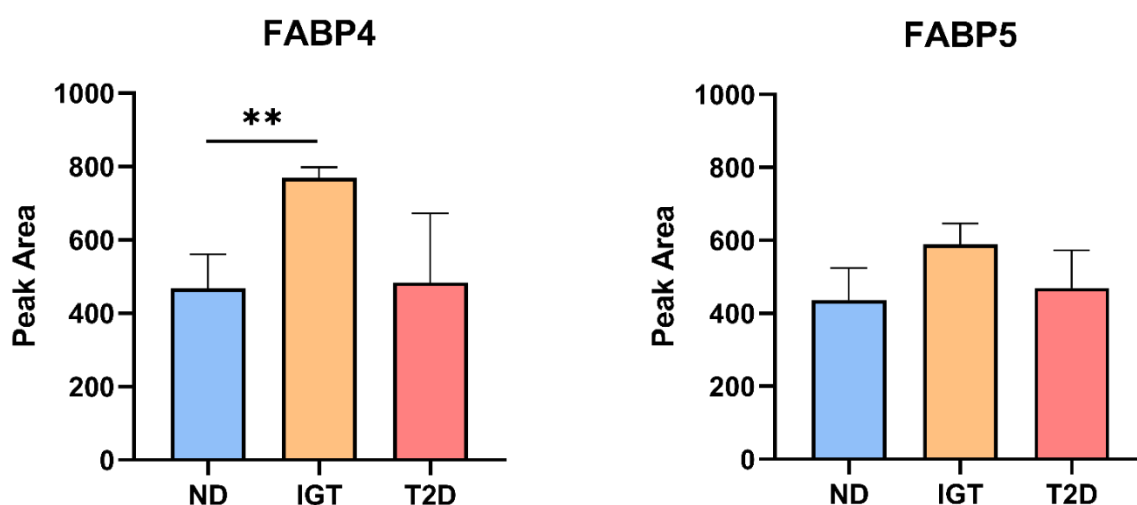


**Figure 11. FABPs expression levels in human liver samples.** The figure shows the expression of FABP4 and FABP5 in ND (Blue), IGT (Orange) and T2D (Red) patients. The quantification is based on the peak area of the three best peptides. N=3, mean +SEM. Multiple t-test applied, \*\*=0.005

Therefore, the key enzymes of the diacylglycerol synthetic pathway were analyzed in **Figure 12a**. The expression of the first two enzymes of the pathway, GPAT and AGPAT, is not heavily influenced by the disease. On the contrary, LPIN2 - the true rate-limiting step of the pathway - shows a marked upregulation in IGT and T2D (**Figure 12**).

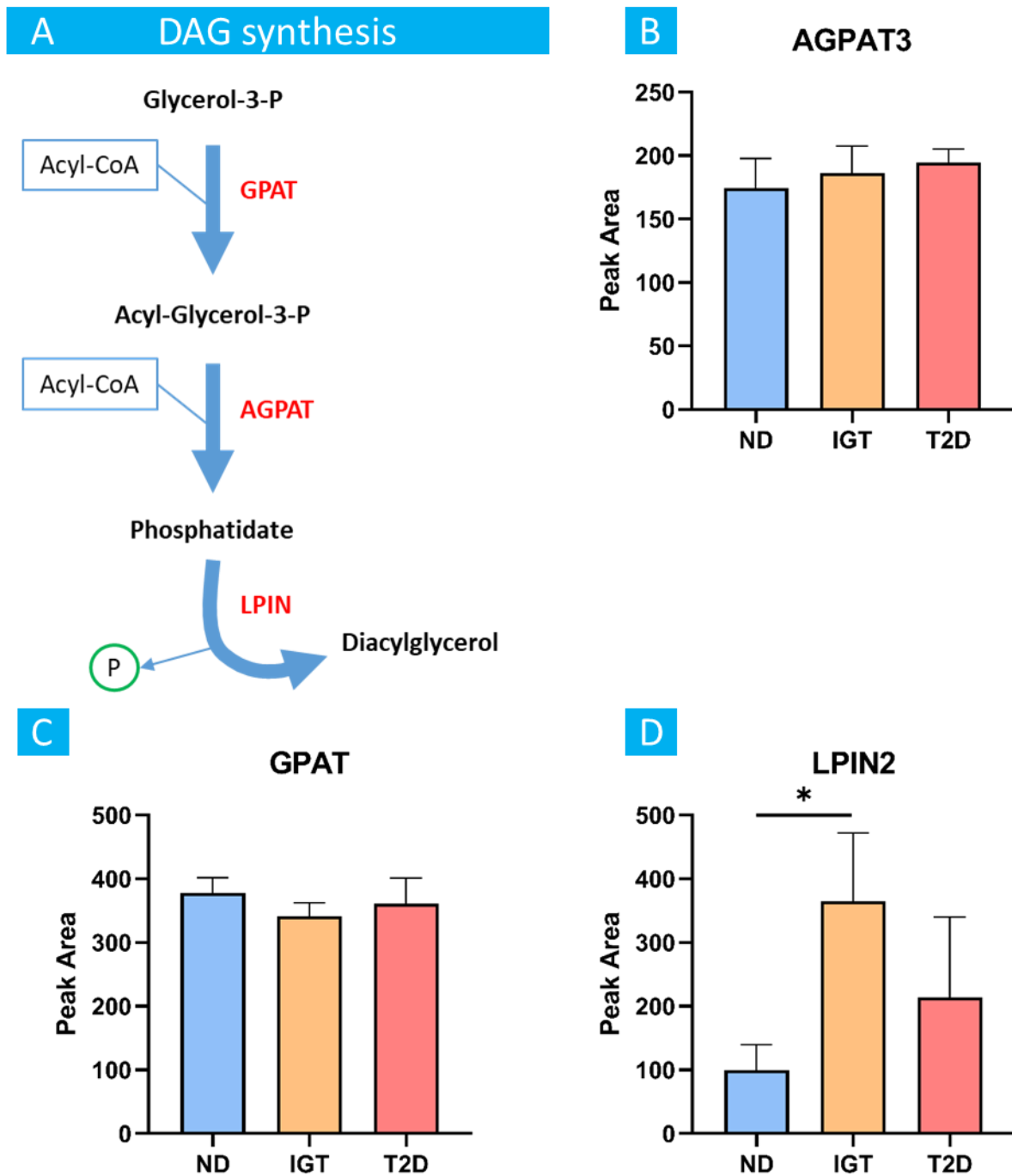


**Figure 12. DAG synthetic pathway analysis.** A. Scheme of the DAG synthetic pathway. B, C and D. The figure shows the expression of GPAT, AGPAT3 and LPIN2 in ND (Blue), IGT (Orange) and T2D (Red) patients. The quantification is based on the peak area of the three best peptides. N=3, mean +SEM. Multiple t-test applied, \*=0.05

In the last part of the analysis, the oxidative stress-connected proteins were considered, finding an upregulation of 3 components of the antioxidant response. HMOX1 is a known target of Nrf2, the transcription factor modulating the antioxidant response. HMOX1 and the isozyme HMOX2 mediated degradation of heme group leads to antioxidant and anti-

inflammatory effects, facilitating the removal of ROS. The same effect is obtained by thioredoxin, through the reduction of oxidized cysteines or disulfide bonds. In **Figure 13** there is a soft upregulation of HMOX1 in IGT patients and HMOX2 is upregulated IGT and T2D groups. Even more marked is the overexpression of thioredoxin (TXN) both in IGT and both in T2D.

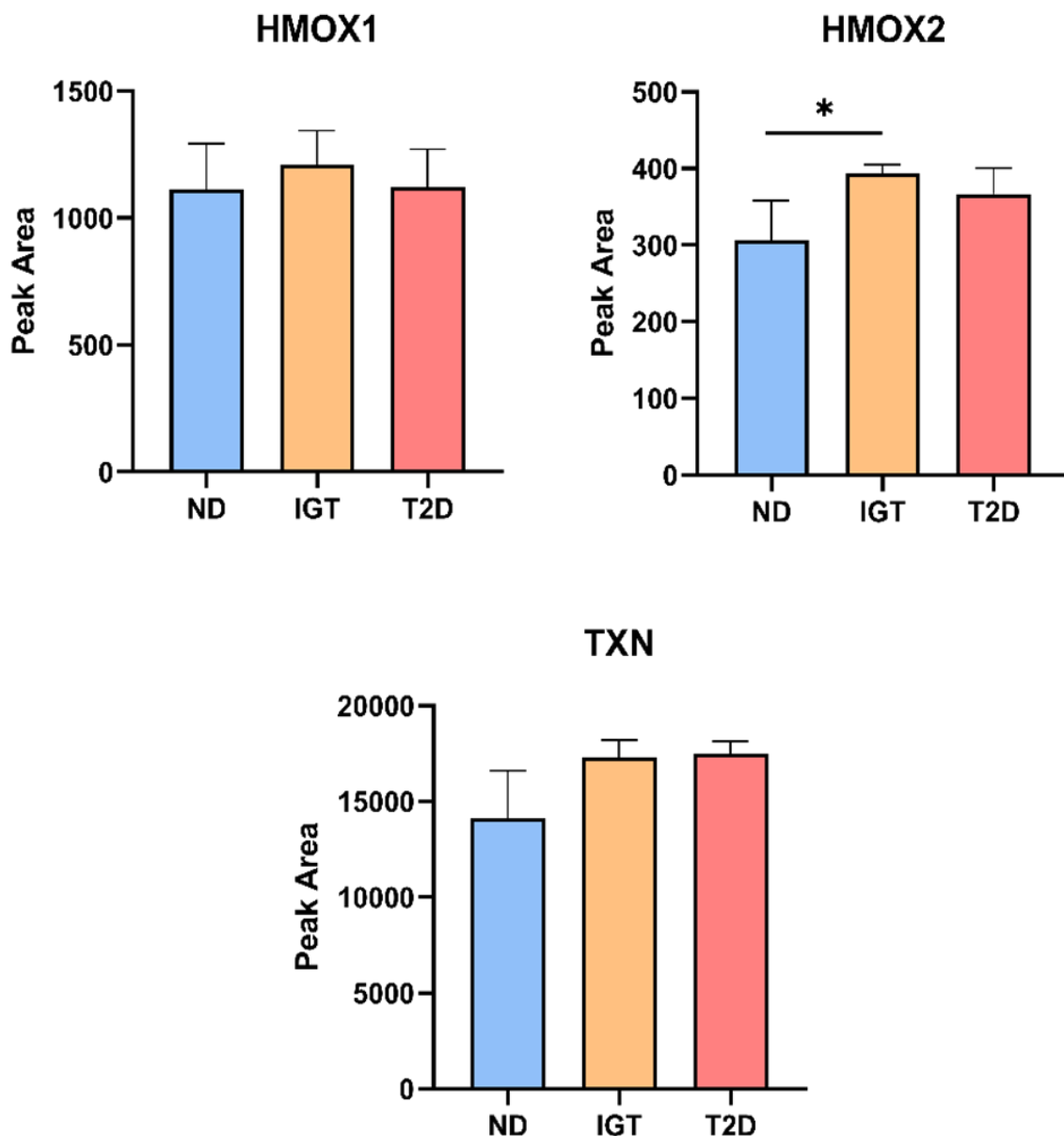


**Figure 13. Oxidative stress analysis.** Oxidative stress state is analysed considering the markers upregulated by the antioxidant response of the cells. A, B and C show HMOX1, HMOX2 and TXN expression in ND (Blue), IGT (Orange) and T2D (Red) patients. The quantification is based on the peak area of the three best peptides. N=3, mean +SEM. Multiple t-test applied, \*=0.05

### 6.3 Bioinformatics analysis of the AQP9 promoter

**Table IV. AQP9 predicted binding sites.** The table gives information about the position of the predicted binding site on the promoter of AQP9, the score Lasagna 2.0 assigned to it, and the p- and E-values. The search module computes a score evaluating how the predicted binding site matches the Transfac database sequence. The p-value indicates the probability to obtain by chance a score higher than or equal to the one obtained. The E-value describes the number of times a sequence with the same or higher score can be found in the promoter analyzed.

	Position (0-based)	Strand	Score	p-value	E-value
<b>Nrf2</b>	<b>-440</b>	<b>+</b>	<b>11.31</b>	<b>0.0001</b>	<b>0.049</b>
<b>Tal1</b>	<b>-71</b>	<b>+</b>	<b>8.8</b>	<b>0.0004</b>	<b>0.196</b>
<b>Stat1</b>	<b>-440</b>	<b>-</b>	<b>15.18</b>	<b>0.00015</b>	<b>0.073</b>

The possible involvement of AQP9 in insulin resistance development in the liver and its dual role both related to oxidative stress and lipid droplet accumulation makes AQP9 a promising candidate to be studied. The upregulation of the channel suggested that either events impact its transcription or its degradation. For this reason, we decided to perform a bioinformatics analysis of the promoter of AQP9, looking for possible binding sites of relevant modulators (Table IV).

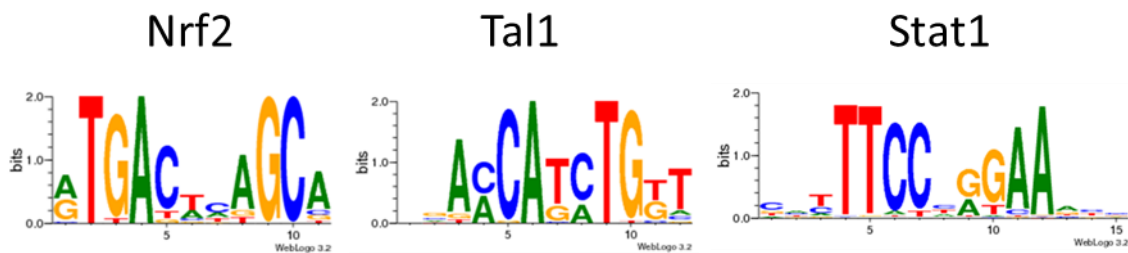


**Figure 14. AQP9 promoter bioinformatics analysis.** AQP9 predicted binding sites for Nrf2 (upper) and Tal1 (middle) and STAT1 (lower). On the left are represented the putative binding sites sequences according to Transfac database. The pictures are visual prediction of the binding sites. The biggest the letter, less is the uncertainty.

As shown below, the prediction points to an Nrf2 binding site (Figure 14). Nrf2, is the master regulator of the antioxidant response. Nrf2 in the inactive form is floating in the cytoplasm bound to Keap1. In presence of an oxidative stress Keap1 is ubiquitinated and degraded, dissociating from Nrf2. The free Nrf2 translocate to the nucleus binding to the promoters of the antioxidant response elements (ARE). The presence of Nrf2 in one of the first hits, together with the high score given by the tool and the low p-value, supports that the AQP9 promoter harbors an ARE. Another interesting hint is regarding the TAL1 binding site, a transcription factor connected to the family of the NFkB pathway. The involvement in

signaling is supported also by the predicted binding site for STAT1, a transcription factor activated also by the EGF signaling cascade and modulating the response of genes important for cell viability. Among the findings, there are also connections of AQP9 with ER stress and lipid accumulation with a couple of predicted binding sites for CHOP::CEBPA (DNS). CEBPA is known to regulate gluconeogenesis and lipogenesis in liver. CHOP is involved in the ER stress response and dimerizes with CEBPA, inhibiting the expression of CEBPA modulated genes.

#### 6.4 HepG2 lipid overload model

Considering all the promising results obtained, A lipid overload model was established on HepG2 cells. The treatment timings and the lipid concentrations were adjusted in order to have lipid accumulation with a limited harm for the cells. The FFAs mix was prepared in a ratio oleate : palmitate 2:1 and we tested two different concentrations, 0.5 and 1 mM. 4 different concentrations of glycerol (50, 100, 250 or 500 $\mu$ M ) were tested and the glucose in the medium increased to 15mM.

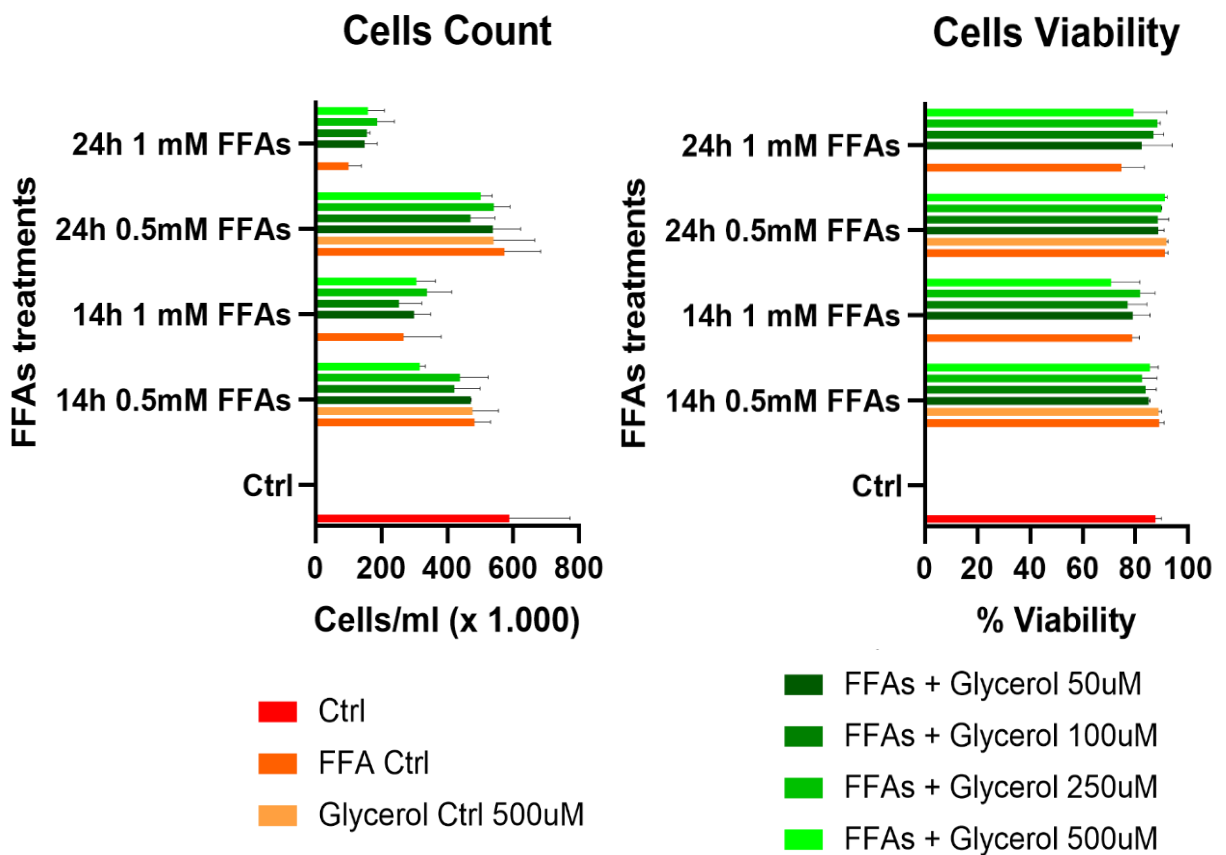
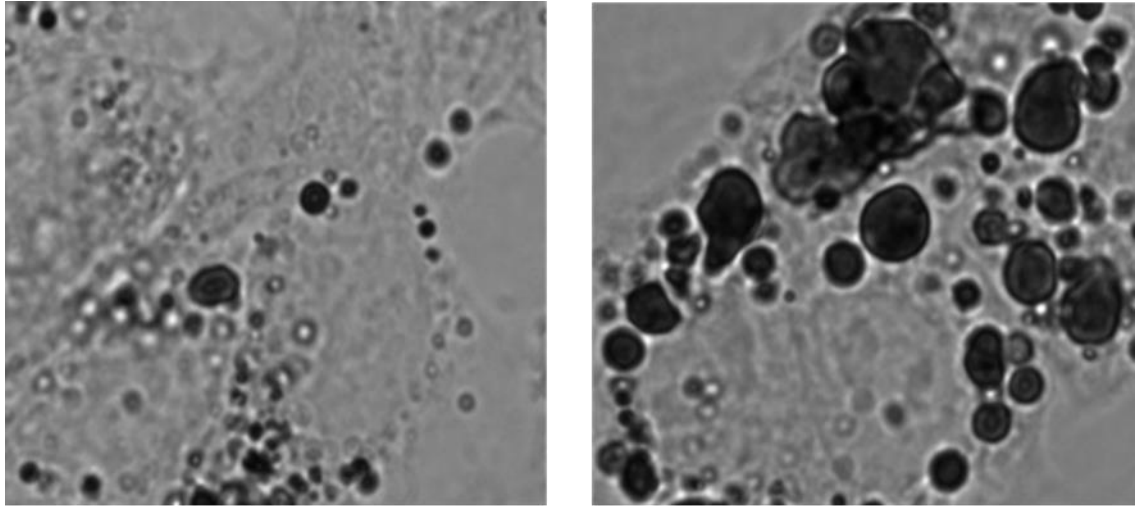


**Figure 15. Cells count and viability.** The graphs report cells count (left) and viability (right) in the different conditions analyzed. n=2, mean + SEM.



Ctrl

LO

**Figure 16. Lipid droplets staining with oil red O.** Cells in control (left) and lipid overload (right) were stained with oil red O. The vacuoles indicated by the red arrow are the lipid droplets in the cells, mostly produced in response to the treatment.

Ctrl

LO

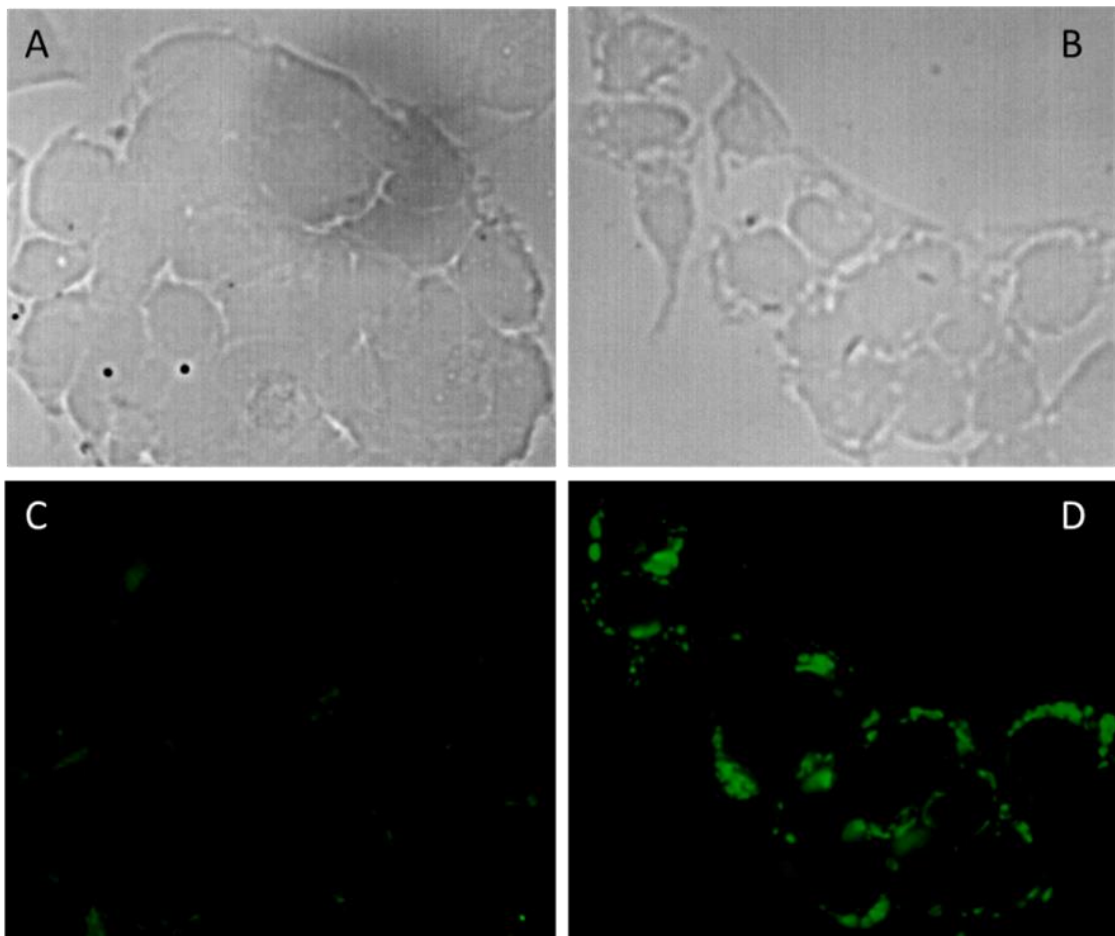


**Figure 17. Lipid droplets staining with Bodipy 493/503.** Panel A and B show the bright field images of control and lipid overload conditions, respectively. Panel C and D show the fluorescent signal of Bodipy of control and lipid overload conditions, respectively.

Time of the treatment and concentration of FFAs or glycerol are influencing the viability of the cells, as shown by **Figure 15**. 1mM FFAs treatment for 24 hours is lethal for the majority of the cells, independently from glycerol concentrations. 14h of 1mM FFAs treatment resulted safer, but glycerol concentrations seriously impaired cell viability in a dose-dependent manner. 0.5mM FFAs treatment is safe for the cells at both the time points and glycerol

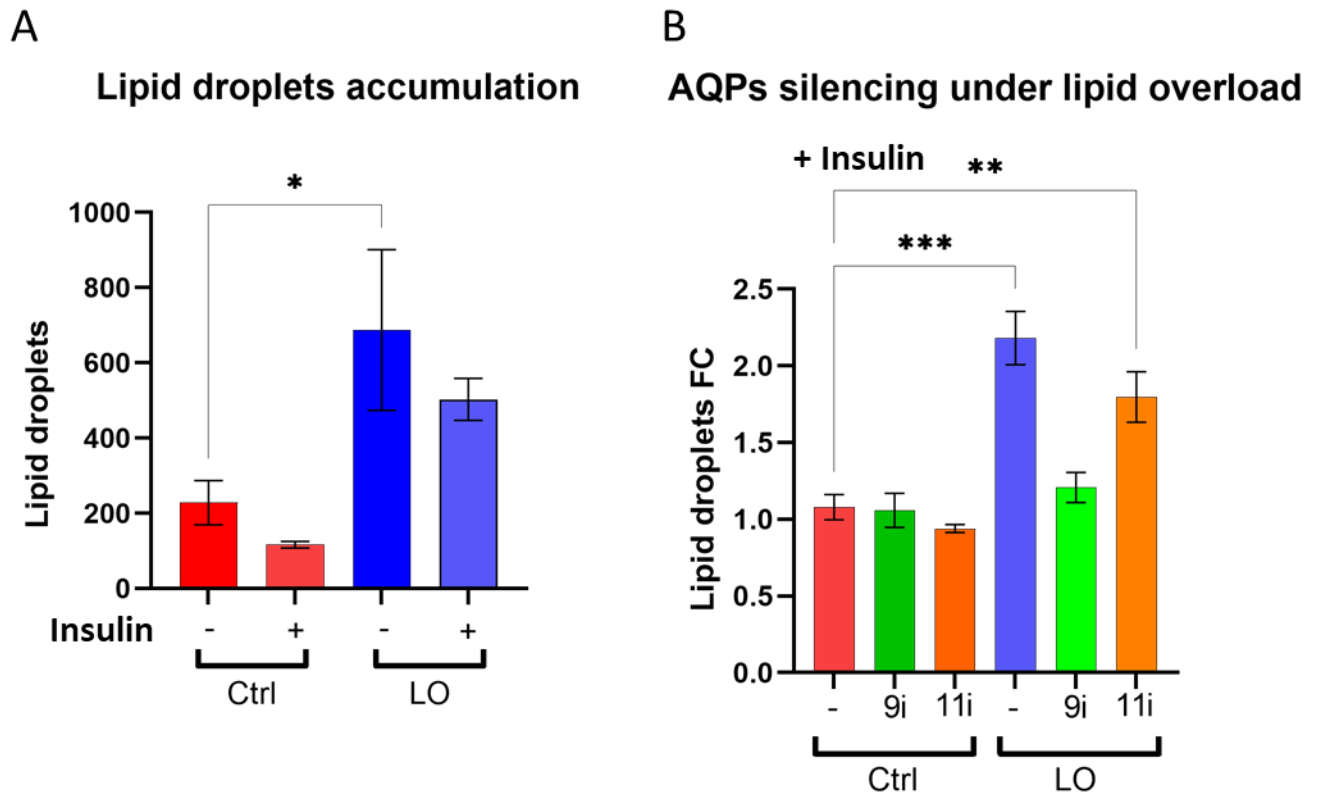


**Figure 18. Lipid droplets accumulation.** The figures show the variations in lipid droplets accumulation stained with Bodipy in the different conditions. Panel A compares the signal coming from the lipid droplets in Control and LO with or without insulin. Panel B exhibits lipid droplets fold change compared to the control in lipid overload conditions silencing AQP9 or AQP11. N=3, mean +SEM. One-way ANOVA applied, \*=0.05, \*\*=0.005, \*\*\*=0.0005

addition does not compromise the viability. After evaluation of all the data, 24h treatment was selected to be sure that the model efficiently mimics lipid overload conditions. The glycerol concentrations were chosen based on the best compromise between lipid droplet accumulation and viability, taking into consideration also the physiological free glycerol levels in obese patients. In **Figure 16** lipid droplet accumulation was analyzed in control and in the lipid overload final treatment. The induced phenotype is visible, with the lipid droplets (in black) extensively present in the lipid overload model. Additionally, the fluorescent labeling of neutral lipid droplets using the Bodipy probe (**Figure 17**), confirming the results with another

staining. Both the number and size of lipid droplets increase in the lipid overload model. Bodipy was used also to measure the impact of AQPs modulation on lipid droplet accumulation.

**Figure 18a** is showing that the lipid overload (LO) alone is able to increase by 2.5-fold the lipid droplet accumulation in HepG2 cells. When the (LO) is supplemented with insulin (+) to simulate the physiological conditions, the lipid accumulation is lower, reaching twice the level of the control. When silencing AQP9 in LO(+) samples the normal phenotype is restored, leading to a signal comparable to Ctrl(+) with silenced AQP9 (**Figure 18b**). The silencing of AQP11 in LO(+) does not induce the same effect, proving the limited involvement of the ER resident AQP in the lipid droplets accumulation. In this case the lipid droplets accumulation is almost twice the control, showing a narrow gap confronted to LO (+) but being significantly higher than the ctrl(+) with silenced AQP11.

#### 6.5 AQP9 upregulation in lipid overload HepG2 model activates apoptosis

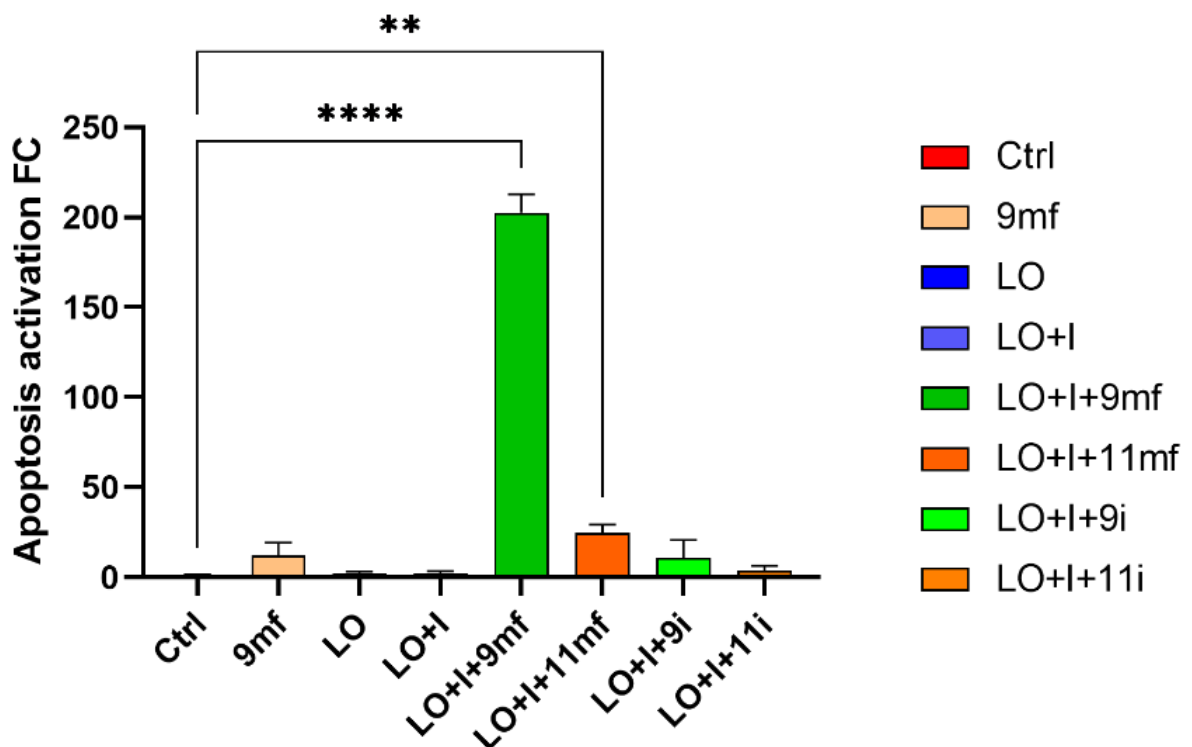


**Figure 19. Apoptosis activation.** The graph shows the fluorescent signal derived from the activity of Caspase 3 and 7, marker of an early apoptosis. Mean + SEM . n=3. One-way ANOVA, p value \*\* = 0.005 \*\*\*\*=0.00005

The effects of the modulation of AQP9 and AQP11 were explored also on the viability of the HepG2 cells, overexpressing or silencing them both in ctrl or lipid overload conditions (**Figure 19**). Checking the activation of Caspase 3 and 7, the early apoptosis activation was checked in the samples. The lipid overload treatment is safe, with no activation of apoptosis in lipid overload or lipid overload + insulin conditions, as for the control. The cells transfected with AQP9 show a slight activation of the apoptosis but not at a significant level. While AQP9 overexpression in LO (+) conditions gives a clear phenotype: an extremely high activation of Cas3/7, probably leading to cell death. Furthermore, AQP11 overexpression, in the lipid overload model is inducing the activation of the apoptotic pathway, even if in a limited way. On the other side, the silencing of both AQP9 and AQP11 in the lipid overload model is not inducing any clear apoptotic effect. Once again AQP9 is confirming its major role in the modulation of lipid overload and cell death. This experiment opened the path to study also AQP11, possibly involved in the complex lipid overload process.

#### 6.6 Insulin signaling influence on hydrogen peroxide flux

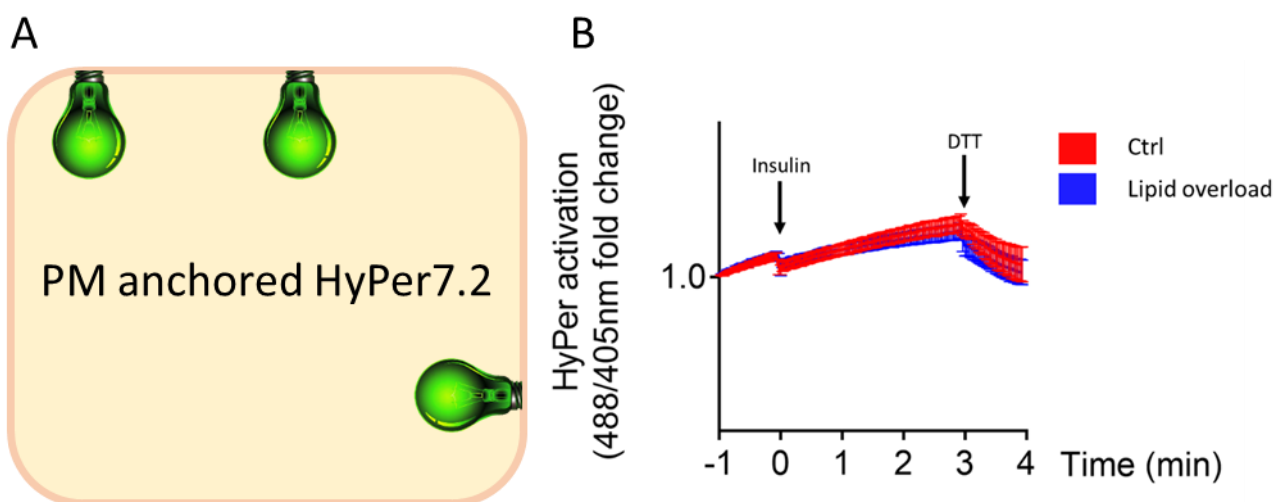


**Figure 20. Insulin-stimulated H<sub>2</sub>O<sub>2</sub> fluxes.** A – Graphical representation of plasma membrane anchored HyPer7.2. B – Time laps analysis of HyPer activation in control (Red) and Lipid overload (Blue) conditions. Mean +SEM. n=3.

With the availability of a valid lipid overload model and the proofs of AQP9 effects on it, the H<sub>2</sub>O<sub>2</sub> physiological fluxes induced by insulin addition were monitored. With the aim to understand if the lipid overload could impair the hydrogen peroxide flux typically produced by tyrosine kinase (TKRs) type receptors [23]. The probe used to check this flux was HyPer 7.2, an H<sub>2</sub>O<sub>2</sub> specific, genetically encoded ratiometric probe, in this case, anchored to the plasma membrane of the cells (**Figure 20a**). In this time-lapse experiment we observed the

oxidative state of the probe after the addition of insulin to the cells at time 0. The probe variation has been recorded for 3 minutes to monitor the flow of H<sub>2</sub>O<sub>2</sub>. At minute 3 DTT was added to reduce the probe and the reduction was monitored for another minute to confirm its functionality.

As shown in **Figure 20b**, a significant difference between the H<sub>2</sub>O<sub>2</sub> flux induced by insulin in control or lipid overload conditions was not detected. The reason behind it could be connected with the scarce response of the probe also in the control condition. Interesting is the behavior of the HyPer sensor before the addition of H<sub>2</sub>O<sub>2</sub>, showing already a basal oxidation slope reflecting active fluxes even before stimulation. The fast reduction operated by DTT confirm that the probe is performing correctly.

### 6.7 Lipid overload decrease the hydrogen peroxide transport in HepG2 liver cells

To increase the response of the probe the setup of the experiment was changed. First, the cytosolic version of HyPer 7.2 was used, which could grant a stronger signal. Second, Hydrogen peroxide was added in a known amount, checking the internalization rate thanks to HyPer 7.2. As shown in **Figure 21A**, the HyPer 7.2 signal in the control condition has an immediate response to the H<sub>2</sub>O<sub>2</sub> addition, confirming the presence of a transporter in the membrane of HepG2 cells. On the other side, we can see a decreased and delayed signal under lipid overload, supporting the idea of modulation of an H<sub>2</sub>O<sub>2</sub> transporter driven by the lipid droplets accumulation in HepG2 cells. DTT reduces HyPer in both conditions.

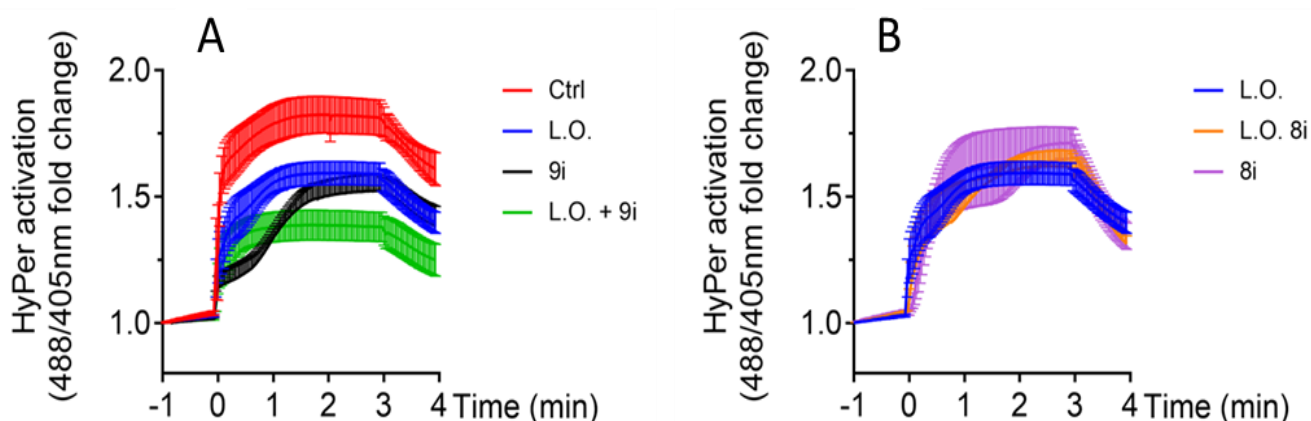


**Figure 21. H<sub>2</sub>O<sub>2</sub> transport inhibition.** This figure shows the activation of HyPer during a 5 minutes time lapse acquisition, with H<sub>2</sub>O<sub>2</sub> addition at minute 0 and DTT addition at minute 3. Panel A shows the H<sub>2</sub>O<sub>2</sub> transport in control (red) and lipid overload (blue), AQP9 inhibition (black) and lipid overload cells with silenced AQP9 (green). Panel B shows the possible role of AQP8 in the impaired transport of lipid overload cells adding AQP8 silencing (purple) and lipid overload on AQP8 silenced cells (orange). Mean and SEM, n=3.

Considering the effect of silencing AQP9 in control HepG2 cells, AQP9 could be partially involved in the effect seen in the lipid overload model. The delayed transport pattern between the two conditions endorses the idea of a possible modulation of the H<sub>2</sub>O<sub>2</sub> flow through this channel. The idea of AQP9 as a sole modulator of H<sub>2</sub>O<sub>2</sub> under lipid overload decayed soon after the analysis of the transport in lipid overload HepG2 cells with silenced AQP9. The response pathway, expected to be similar to the lipid overload and AQP9 silencing, showed a further decrease of H<sub>2</sub>O<sub>2</sub> changing the scenario. These results highlight the presence of another functional transporter, mainly responsible for the H<sub>2</sub>O<sub>2</sub> transport inhibition driven by lipids. Knowing AQP8 transport is redox modulated [52,65], AQP8 was inhibited in the lipid overload model (**Figure 21B**). The overall results cannot confirm that AQP8 or AQP9 alone are responsible for the H<sub>2</sub>O<sub>2</sub> transport inhibition in the LO model. Anyway, AQP8 involvement in this process cannot be excluded, since the similar transport shared by lipid overload, lipid overload with silenced AQP8 and AQP8 silencing. This opens to the presence of a third functional channel influencing the H<sub>2</sub>O<sub>2</sub> transport, in what seems to be an extremely controlled redox environment.

#### 6.8 Oxidative stress accumulation in the endoplasmic reticulum of Lipid overloaded HepG2 cells

Based on the literature, lipid overload in liver cells is promoting oxidative stress accumulation in the ER followed by ER stress development [75–77]. To check the possible insurgence of

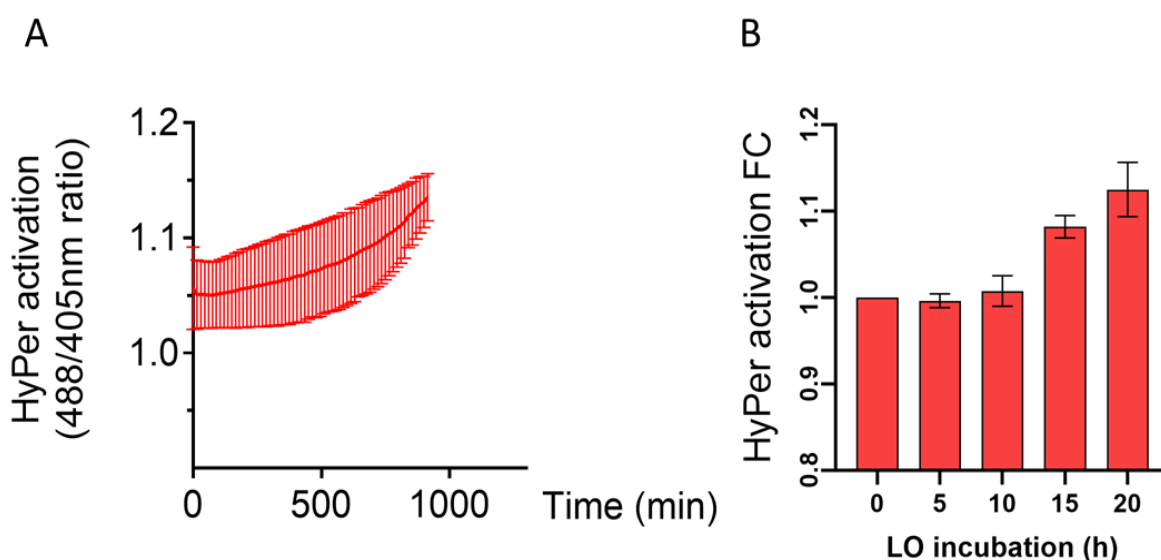


**Figure 22. Lipid-induced H<sub>2</sub>O<sub>2</sub> accumulation in the ER.** Hydrogen peroxide accumulation in the ER is here shown using an ER lumen resident H<sub>2</sub>O<sub>2</sub> version of HyPer. Fluorescence acquisition has been performed on cells under lipid overload for 20h. Panel A shows the average ratio values of the probe. Panel B shows the fold change of the ratio at different time points compared to the time zero. Mean + SEM, n=3.

redox stress accumulation in the ER, a fluorescence time-course experiment under lipid overload was performed. Using HyPer located in the lumen of the ER, the oxidation of the probe for the first 20 hours of the treatment was monitored (**Figure 22**). In the first half of the treatment, there were no significant variations in oxidative stress in the ER. In the last 8 hours, the  $H_2O_2$  is growing exponentially. This experiment confirms once again the validity of the lipid overload model, resembling the traits of an obese pre-diabetic patient.

### 6.9 Is there a reductive shield around the endoplasmic reticulum?

After the confirmation of the oxidative stress accumulation in the ER of HepG2 cells, the  $H_2O_2$  transport inside the ER and the oxidative state of the region surrounding the ER was studied. This time with the help of HyPer in the lumen of the ER and anchored outside the ER membrane. Checking the  $H_2O_2$  transportation in basal conditions (**Figure 23**) a particular behavior of the probe was detected. HyPer in the lumen of the ER is not reacting to the  $H_2O_2$

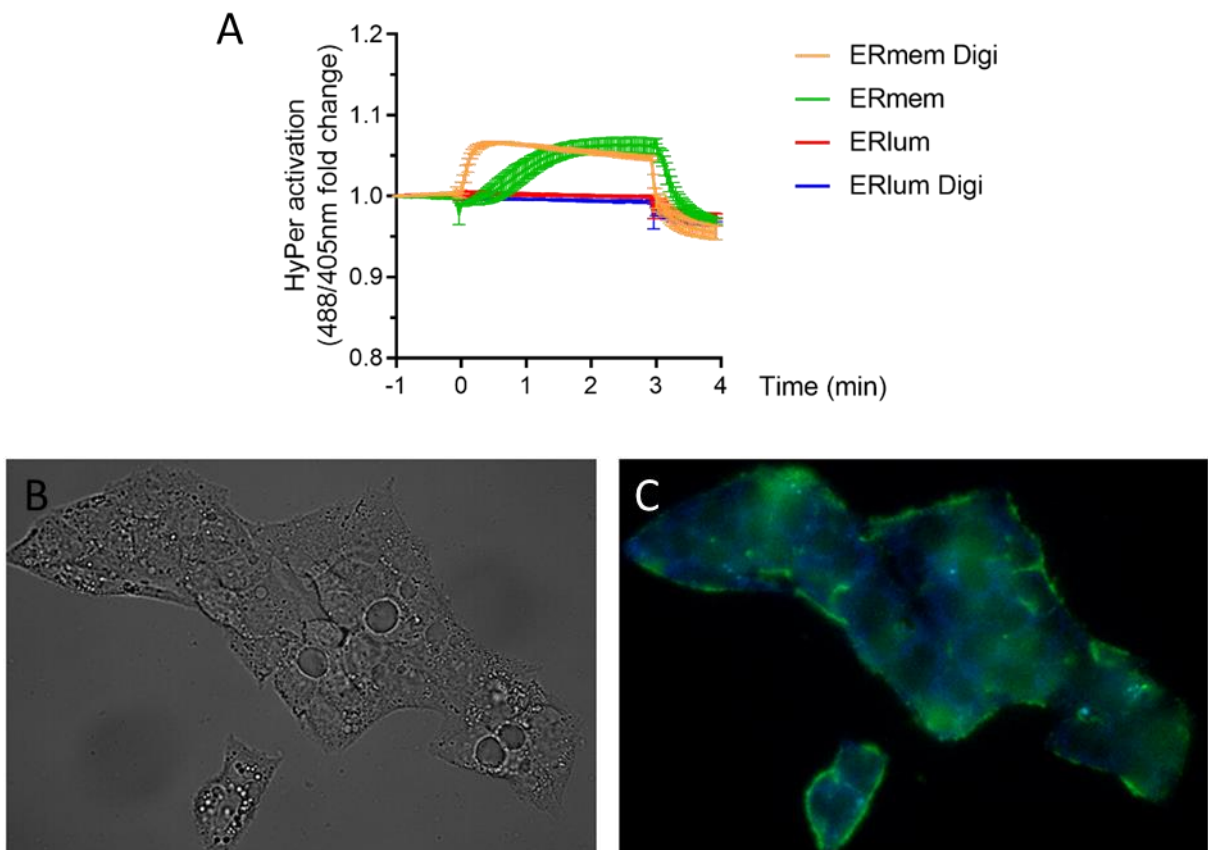


**Figure 23. HyPer responsiveness and basal state anomalies.** A – Oxidation of HyPer located in the ER lumen (red) or anchored on the cytosolic side of the ER membrane (green). The Effect of digitonin treatment on activation of HyPer in the ER lumen (blue) and anchored to the ER membrane (orange). B – Bright field image of HepG2 cyto stable cell line. C – Fluorescence image of HepG2 cyto at 405nm (blue) and 488nm (green) excitation wavelength.

addition, while the probe is reduced by DTT. HyPer anchored outside the plasma membrane showed a constant delay of 1 minute/1minute and a half in sensing H<sub>2</sub>O<sub>2</sub>. An attempt was done to decrease the delay, creating small pores in the plasma membrane with a digitonin treatment. The digitonin effect is deleting the delay, restoring the instantaneous response of the probe in the ER membrane. HyPer in the lumen of the ER remains non-responsive to the H<sub>2</sub>O<sub>2</sub>, but confirms the integrity of the ER membrane. This support the idea of a possible presence of a “reductive shield” around the membrane of the ER, which will be discussed.

Backing this consideration, a particular pattern of the cytosolic HyPer 7.2 was seen when stably integrated into the HepG2 cells (**Figure 23c**). Usually, HyPer is presenting a uniform oxidative state at the basal state when free-floating in the cytosol. Working with HepG2 cells a clear distinct pattern of oxidation was seen. An intense oxidation was localized next to the plasma membrane and the border of the cells. On the other side, an intense reducing environment was found in what resembles the deepest part of the cytosol, next to the ER. Further elucidations are needed of what could be a key component of cell life.

#### *6.10 Data Independent Acquisition (DIA) development II: Staggered windows width*

Despite the great results granted by the variable windows DIA, it has also some drawbacks. The major one is the lack of flexibility. The requirement of a project-specific ion library allows reaching noteworthy results, at the price of time, resources and sample consumption. For this reason, a library-free approach (directDIA) and the implementation of bioinformatics-based staggered windows method first developed on nanoLC and orbitrap-type instruments was considered. The development of this method on  $\mu$ LC and TripleTOF-type equipment required an extensive workload, but it constitutes a noteworthy step forward from the original method in terms of speed and reproducibility.

Ion libraries & windows schemes: starting point

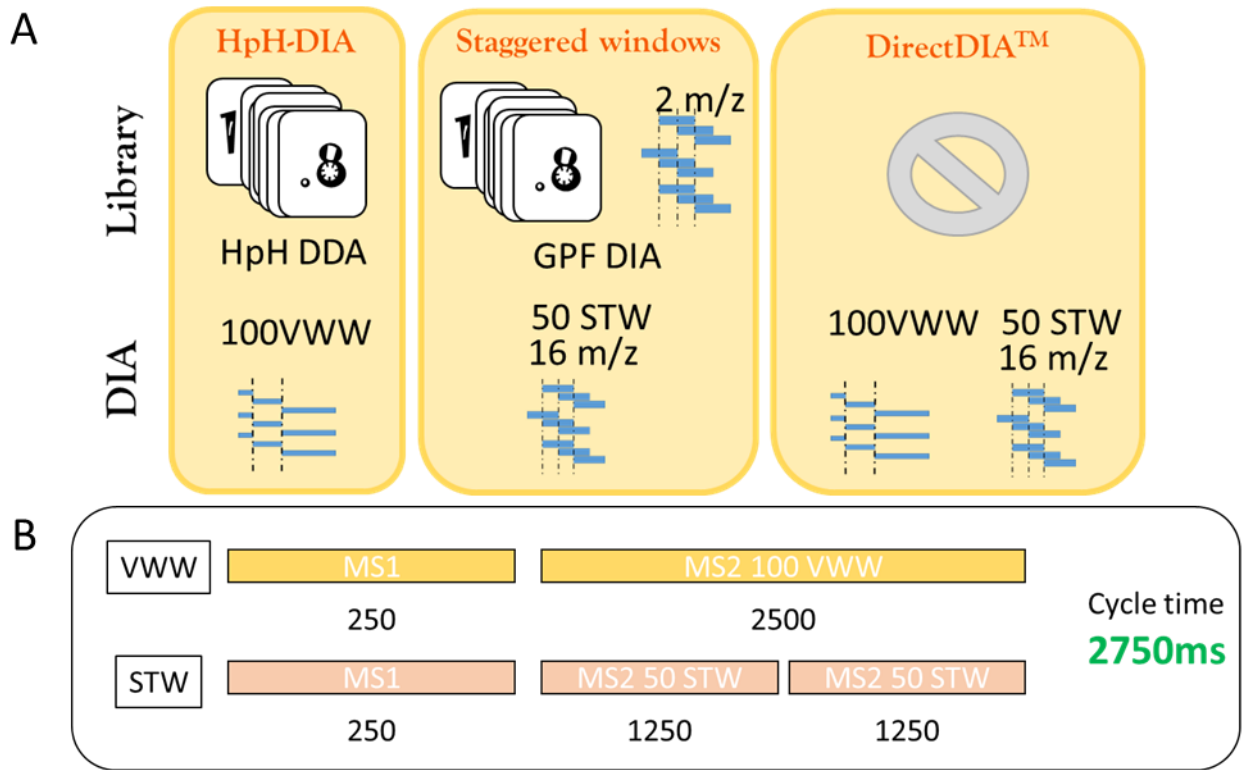


**Figure 24. DIA methods schemes.** A - Schematic representation of VWW, STW and directDIA methods. B – Scheme showing the equilibrated cycle time between the two methods.

The ion library is the key limiting step of the VWW-DIA originally developed, since it is based on an offline HpH fractionation with fraction concatenation and DDA acquisition of the fractions. The staggered windows method is based on the creation of an ion library with a gas-phase fractionation technique. A pooled sample was created taking a few microliters from each sample. The pooled sample was injected in the MS 8 times, creating 8 gas fractions

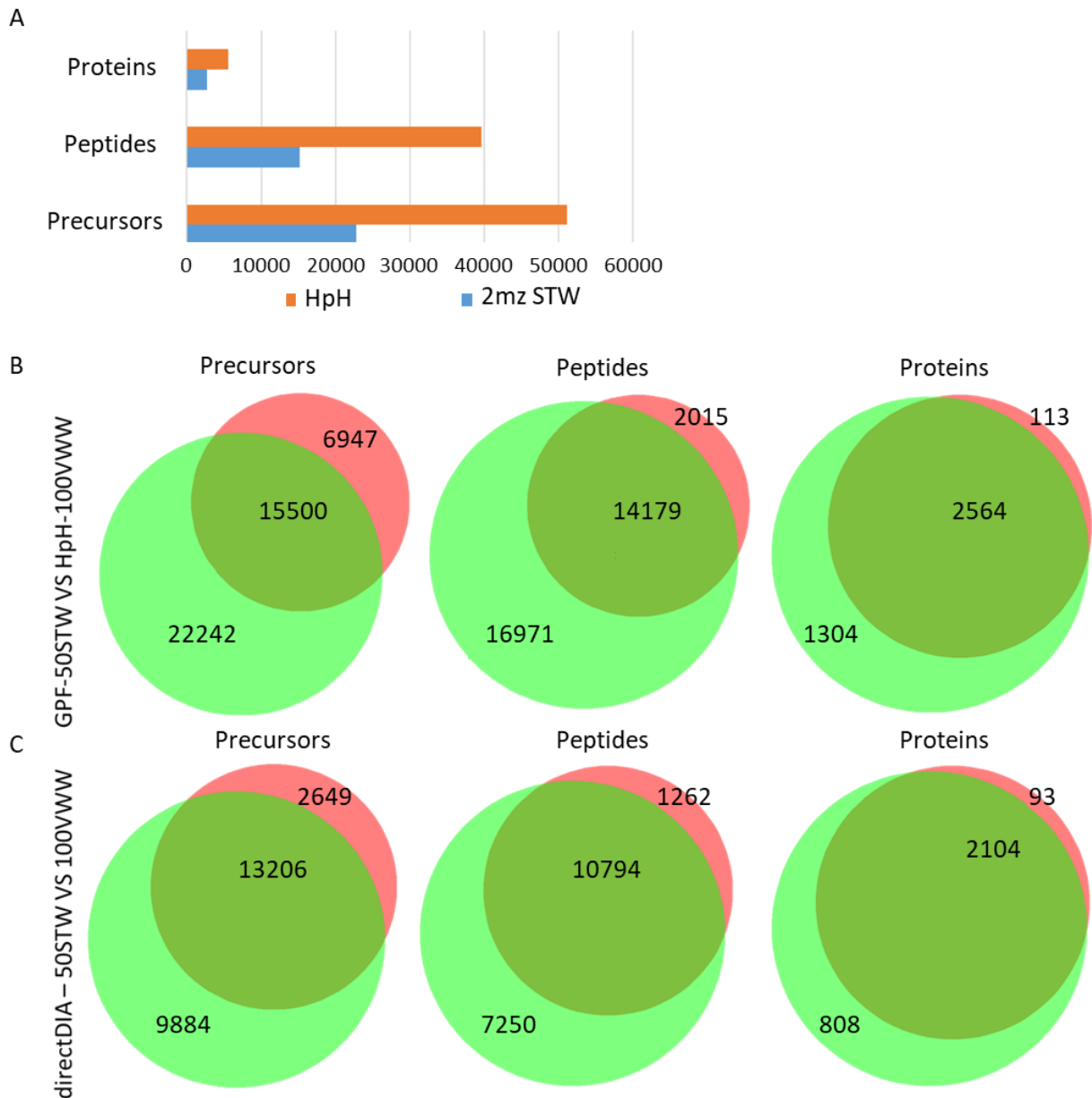


**Figure 25. Ion libraries depths and performances.** A. Precursors, peptides and proteins identified in 2mz GPF and HpH libraries. B- Precursors, peptides and proteins (left to right) identified in GPF-50STW (red) and HpH-100VWW (green) represented in Venn diagrams. C- Precursors, peptides and proteins (left to right) identified with directDIA on 50STW runs (red) and 100VWW runs (green) represented in Venn diagrams.

acquired via DIA. Each fraction covered 100mz, and thanks to the TripleTOF speed, this space was divided in 50STW, each one of 2mz (**Figure 24a**). The deconvolution of overlapped windows results in 1mz windows. 8 GPF library were compared with the 8 HpH fraction library (**Figure 25a**) and a relevant difference in the number of identified precursors, peptides and proteins was seen. To verify the performance of this library the DIA samples were run. The VWW method deployed 100 variable windows calculated with SwathTuner. To match the cycle times 50 STW of 16mz scheme was selected(**Figure 24b**). With a constant 25ms accumulation time in both the methods and a common MS1 accumulation time of 250ms the MS cycle time matched to 2.75s and 4.8 expected datapoints/peak at FWHM. This first version of STW did not give the expected results, with low performances for the identification of proteins, peptides and precursors, as shown in **Figure 25b**. The Venn diagrams highlight the big difference between GPF+50STW and HpH+100VWW, highlighting the need for further development steps. The analysis of these runs with directDIA showed all its limits, with a significant drop in the identification rate (**Figure 25c**). The similar disproportion visible in the Venn diagram clarifies that the difference is not due just to the libraries, but also to the DIA runs settings.

### 6.11 Ion libraries refinement

The first results showed the multiple problems connected with the first staggered windows approach. Proceeding by steps, first the scarce results of the first GPF library was solved.

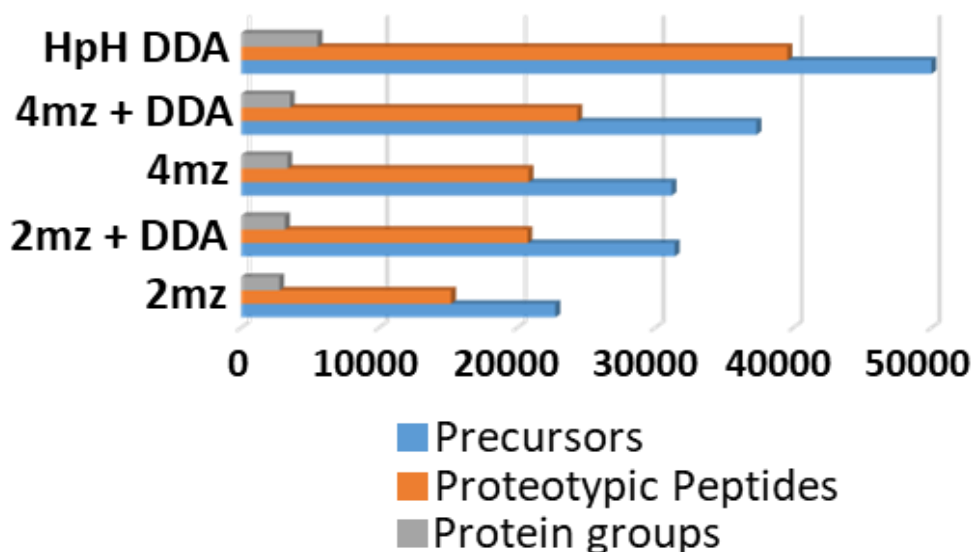


**Figure 26. Improved ion libraries depth.** Ion libraries identified precursors, peptides and proteins.

Increasing the dimension of the staggered windows to 4mz, decreasing the number of the windows from 50 to 25, and increasing the accumulation time a new library was produced. Then the inclusion of 3 DDA runs in both HpH and GPF libraries, created hybrid libraries. Both these modifications applied worked effectively to expand the libraries. **Figure 26** shows the libraries' depth in terms of proteins, peptides and precursors identified. The new 4mz library produced much more comforting results, improving by far the IDs compared to the 2mz library. DDA addition improves the coverage of all the libraries, especially the GPF libraries. Moreover, the DDA runs in GPF libraries help in the retention time alignment, improving the reproducibility of the library. Despite all the efforts, as expected, the HpH-DDA library results remain unreachable at the moment.

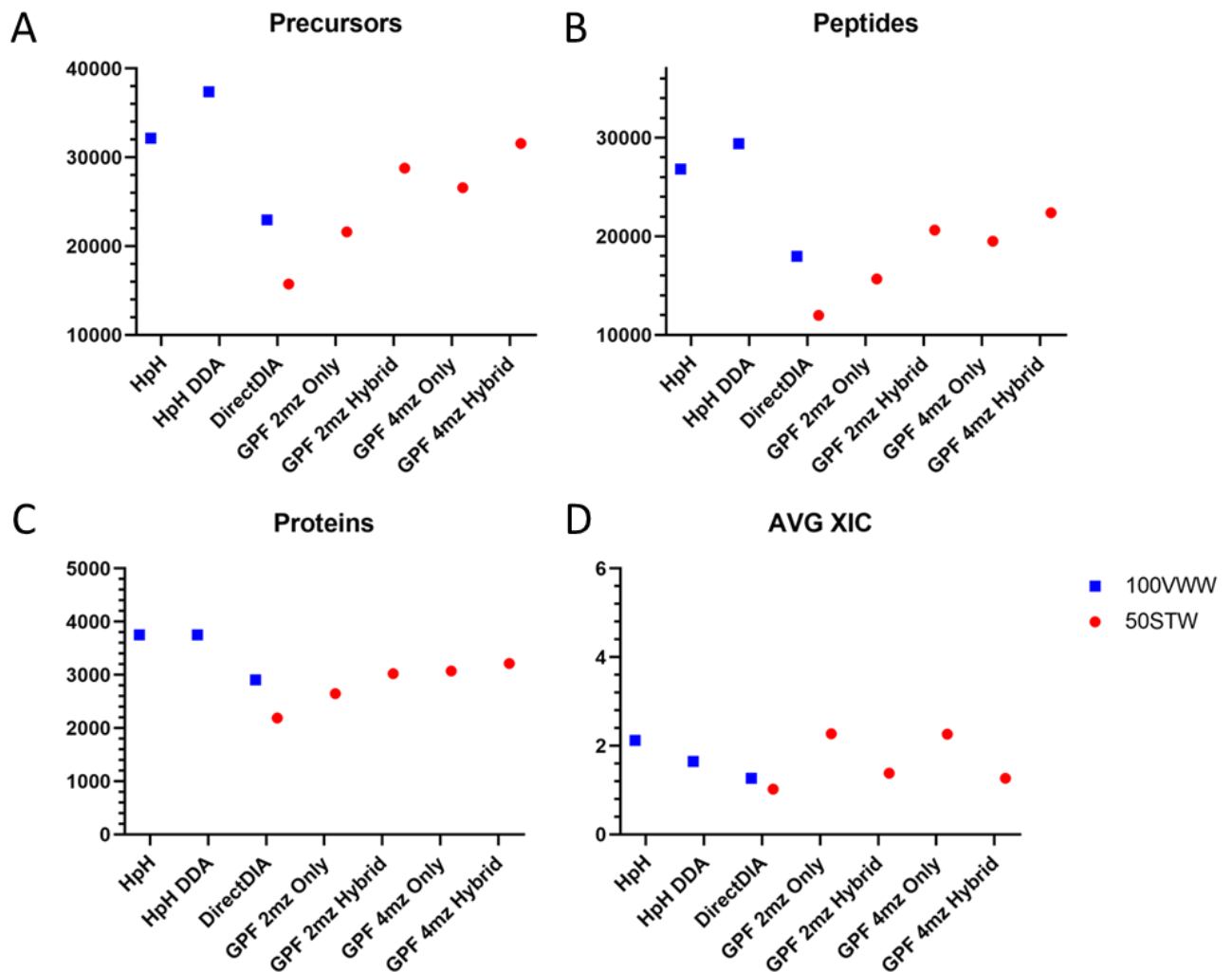


**Figure 27. Libraries yield comparison.** The picture shows the precursors (A), peptides (B) and proteins (C) identified with the different libraries in the 100VWW DIA runs (blue) and 50STW DIA runs (red). The average extracted ion chromatogram is shown in panel D.

The new libraries were used to analyze the 50 STW and 100 VWW runs and to understand the improvement associated with them. From the results shown in **Figure 27**, the significant difference promoted by the 4mz library is visible. Comparing it to the simple 2mz library, the average identified precursors increase to 123%, the identified peptides to 124% and the identified proteins to 116%. The scheme with larger windows and an increased accumulation time gave the expected results.

The validity of the hybrid libraries was checked. Both 2mz and 4mz hybrid libraries showed an improved coverage of precursors, peptides, and proteins, promising an important advancement. The presence of 3 DDA runs gives multiple benefits to these libraries, from the push in the identification rate to the gain in the retention time stability. Moreover, it has been able to push the yield of the 2mz library, reaching 133% of precursors, 131% peptides and 114% proteins. The 4mz hybrid library is reaching significant results, covering 118% precursors, 114% peptides and 105% proteins compared to the normal 4mz library. When compared to the original 2mz library, the 4mz hybrid yield is 146% for precursors, 143% for peptides and 121% for proteins. The HpH Hybrid library gains identifications of precursors and peptides thanks to the DDA stochastic nature too. It hits 120% of precursors and 113% of peptides identified by the HpH library. Being already near to the plateau, the DDA runs are not able to add a significant amount of identified proteins to the library. The average extracted ion chromatogram (**Figure 27d**) window for individual precursors was comparable between HpH and GPF-only libraries. Interestingly, the hybrid libraries drastically improved the AVG XIC, decreasing it by approx. 40% in STW and 20% in VWW. The XIC improvement is granted by the increased retention time precision of the libraries carrying DDA runs. The GPFs for their nature are not detecting all the iRTs in each fraction, impairing the retention time precision of the library. The fact that both the GPFs and the DDA runs were supplemented with iRT peptides, contributed to the increased coordination of the retention times in-between the GPFs. This led to the noteworthy improvements of hybrid libraries' retention time and, consequently, identifications. These encouraging results elect the 4mz GPF Hybrid library as the best candidate for the STW final method.

## 6.12 Windows scheme refinement

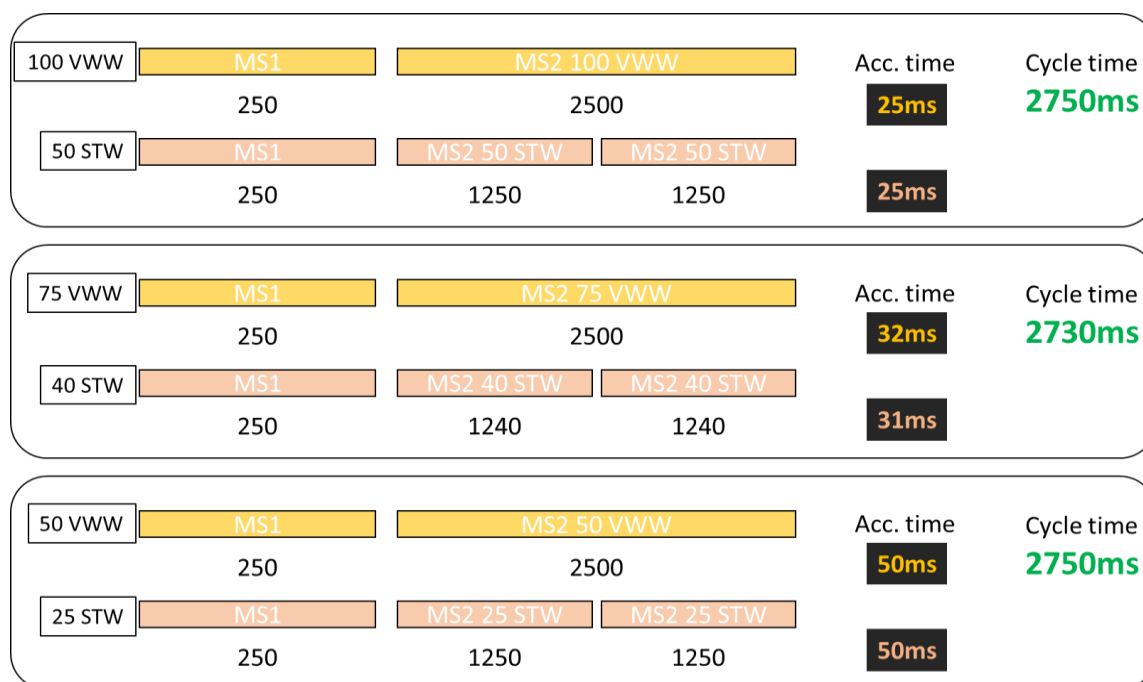


**Figure 28. DIA cycle times comparisons.** Scheme representing the cycle time and accumulation time in the different DIA approach used.

Once found the best library, the focused switched to the windows scheme. The cycle time of 50STW to the 100VWW matched, but the windows schemes were not modified. So the dimension of the STW and the number of the VWW were changed to gain more identifications through a better noise deconvolution. Two VWW conditions, with 75 and 50 windows, and 2 STW conditions, were added with 40 and 25 windows. The accumulation time was tweaked to obtain a comparable cycle time also in the new settings coupled like this: 75VWW - 40STW and 50VWW – 25STW (**Figure 28**). The analysis of the DIA runs was performed on the best libraries, the hybrid ones. **Figure 29** is showing that the results are influenced by the different DIA approaches in a limited way compared to the difference induced by the different libraries. Despite this, modifying the windows width influence the results, especially for the staggered windows. The 50STW resulted to be inferior setting for STW. Both the new options interestingly offer a relevant increase in the identification of precursors, peptides and proteins. An improvement was seen also in the VWW with the two new schemes, even if to a lesser extent. Considering the identification power, the best option seems to be the couple 75VWW and 40STW. Both these schemes give

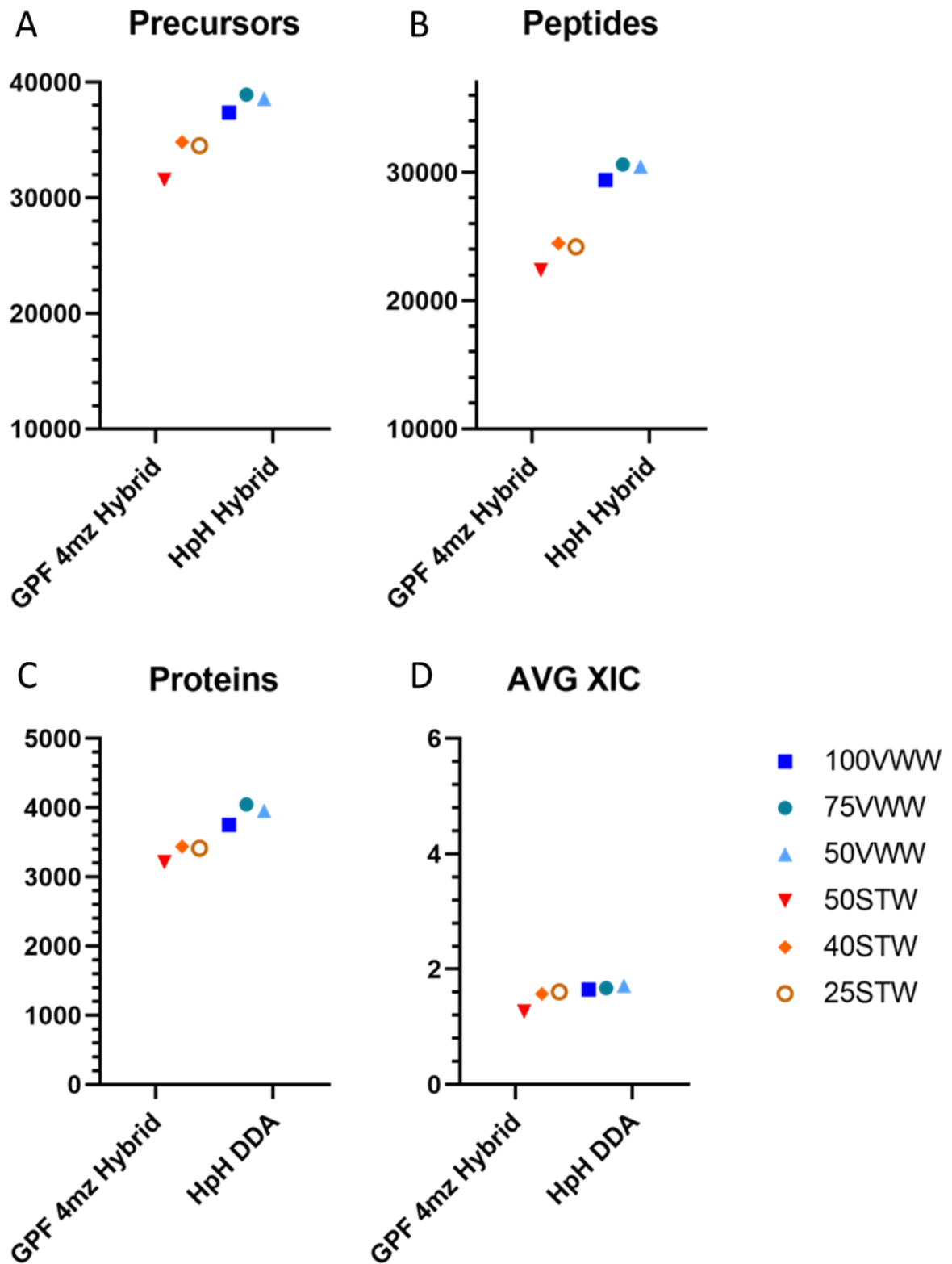


**Figure 29. Windows schemes improvements.** The figure shows the identification of precursors (A), peptides (B) and proteins (C) with the different windows schemes for both VWW and STW. The average extracted ion chromatogram is shown in (D). Mean of 3 technical replicates.

the best results in the identifications of precursors, peptides and proteins. The average XIC is stable for all 5 schemes except the 50STW, which has a slightly lower value.

### 6.13 Coefficient of variation and ID m/z distribution

Based on the identifications, the 2 best methods were selected both on the classical side (HpH-DDA + 75VWW) and the advanced one (4mz-GPFs-DDA + 40STW). Those two evidenced noteworthy advantages compared to all the other versions. Before confirming them as final choices, the coefficient of variations (CVs) and the distribution of the identifications were compared between all the windows schemes (**Figure 30**). All methods display good reproducibility (A), having a starting point at 10.1% median for GPF-4mz-Hybrid 50STW

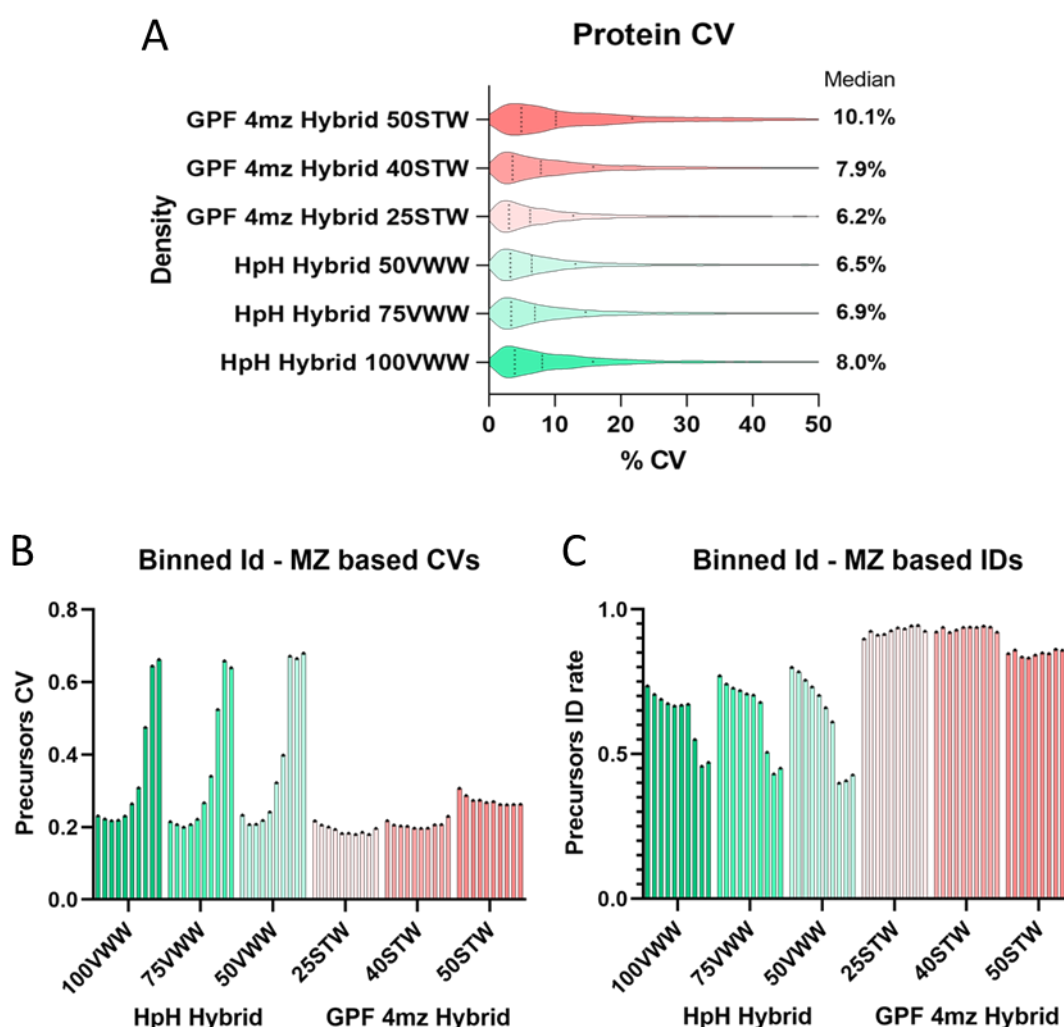


**Figure 30. CVs and IDs analysis in different windows schemes.** A – Protein CVs distribution. B – Binned CVs. 400-1200 m/z range is split in 10 bins. C. Binned Id rate. 400-1200 m/z range is split in 10 bins. STWs in red colours and VWWs in green colours.

and 8% for HpH-Hybrid 100VWW. The optimizations have been able to reach as low as 6.2% and 6.5% median, for GPF-4mz-Hybrid 25STW and HpH-Hybrid 50VWW combinations, respectively. Analysis of %CV dependence on the precursor m/z (B) revealed that VWW methods suffer from increased %CV for the precursors above 800m/z, due to the progressively bigger windows at higher m/z values. STW-based approach displays superior control over %CV across the full m/z range when analyzed with 4m/z GPF-Hybrid library or DirectDIA™ (DNS). In particular, the combination GPF 40STW can reach optimal values of CV keeping it controlled also at high m/z ranges. Similarly, precursor ID rate (C) drops at higher m/z values for 100VWW, while it is stable across the m/z range for STW-based methods. Among STW schemes, 40STW displays the best overall stability for both the %CV and %ID distribution.

These results once again confirm the indications given by the analysis of the identification. The 4mz-GPFs-DDA 40STW approach is a valid approach for the DIA analysis.

#### 6.14 Biological experiment validation

In the end, we decided to compare the behavior of the two different approaches in a biological

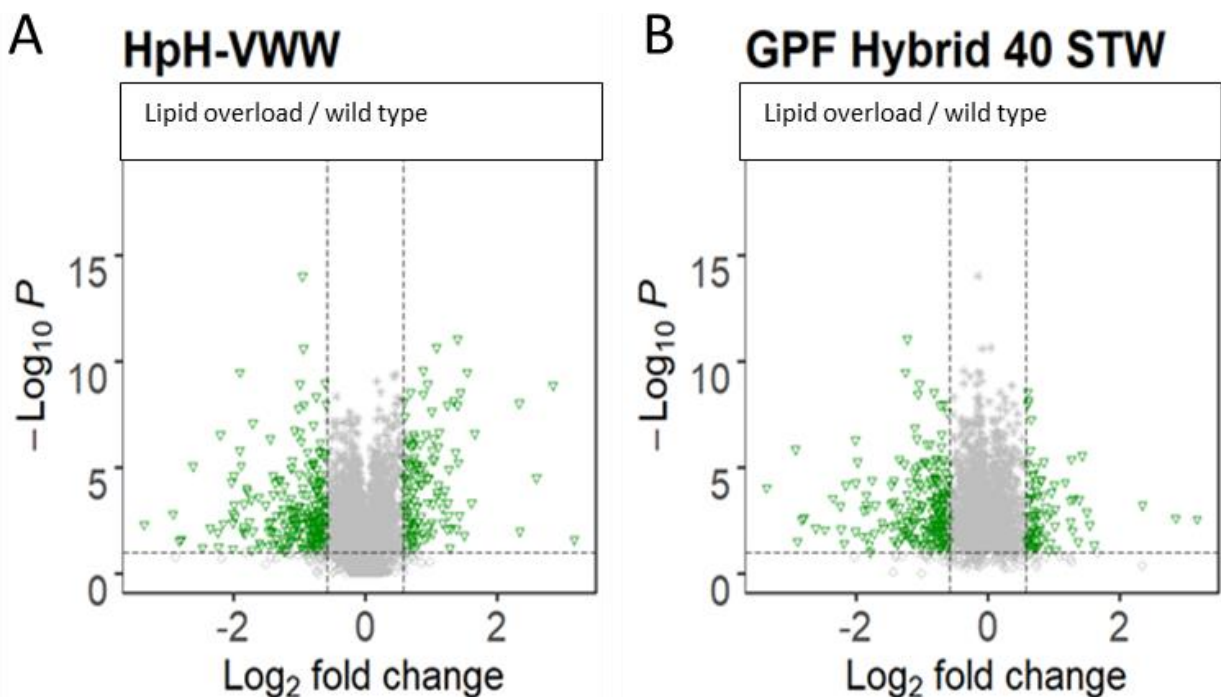


**Figure 31. HpH-VWW and GPF-40STW performance comparison in a biological experiment.** Volcano plots representing under or overexpressed proteins in LO compared to basal state. log2 fold change of 0.58 and  $-\text{Log p-value}$  of 1.3 thresholds have been applied. Panel A shows results obtained with HpH Hybrid-VWW and panel B the results obtained with GPF Hybrid 40STW

experiment (**Figure 31**). We prepared samples from HepG2 wt. and HepG2 treated with lipid overload. The experiment was run in triplicate with the variable windows approach and with the staggered windows one. With a log<sub>2</sub> fold change of 0.58, -log<sub>10</sub> p-value > 1.3, and at least 2 peptides per protein, the HpH/100VWW identified 365 significant candidates, while the best STW identified 313 candidates, respectively. Despite the lower number of candidates identified, the GPF Hybrid/40 STW results are of better quality with a lower %CV of Log<sub>2</sub> fold change estimation (11% vs 13%).

#### 6.15 *Untargeted proteomics analysis of HepG2 under lipid overload and with AQP9 modulation*

With the help of the staggered windows method, we performed a DIA proteomics analysis on HepG2 cells to understand the proteomics variations in the four different conditions of interest:

- HepG2 in control conditions
- HepG2 under LO(+)
- HepG2 under LO(+) with the overexpression of AQP9
- HepG2 under LO(+) with the silencing of AQP9

The significant proteins are listed in the supplementary materials.

##### 6.15.1 LO(+) vs Ctrl

The first comparison sees lipid overload + insulin against control HepG2, to clarify the effects of the lipid overload on HepG2 cells. Variations in some key proteins suggest an insurgence of mitochondrial dysfunction and a decrease of the oxidative phosphorylation. There was an upregulation of GPX4 and a downregulation of CASP8, of the NADH:ubiquinone oxidoreductases subunits NDUFA13 and NDUFB6, of SURF1 (cytochrome C oxidase assembly factor), TXN2 (Thioredoxin 2) and ubiquinol-cytochrome c reductase, complex III subunit XI (UQCR11).

The sirtuin signalling pathways seems to be affected by the treatment. An upregulation of Histone 3A and PRKAA2 (prot kin amp-activated catalytic subunit alpha 2) and a downregulation of NDUFA13, NDUFB6, BAX (BCL2 associated X, apoptosis regulator) and mitochondrial transporters TIMM9-10 and TOMM6 were detected. There are indications of an interferon signalling, with the downregulation of BAX and TAP1 (transporter 1, ATP binding cassette) and the upregulation of PTPN2 (protein tyrosine phosphatase non-receptor

type 2). In general, analysing the cellular functions, there is an increase of the proteins promoting the activity of lipid accumulation TAG concentration (PNPLA2). Perilipin 2 (PLIN2) is five times more abundant in LO(+) cells than in the Ctrl, confirming the same pattern seen previously in IGT and T2D patients. The data regarding AQP11 are interesting. The ER resident aquaporin, in an environment with a growing mitochondrial dysfunction and oxidative stress, is downregulated of 2.5 times compared to the control. Another downregulated protein is Rab5b, a mediator of the formation of the early endosomes, showing a reduced endocytosis in LO(+) cells.

Altogether, the analysis confirms the data experimentally obtained before. Cells under LO(+) show an upregulation of the pathways connected with lipid accumulation and mitochondrial dysfunction. Despite this, the oxidative stress remains limited.

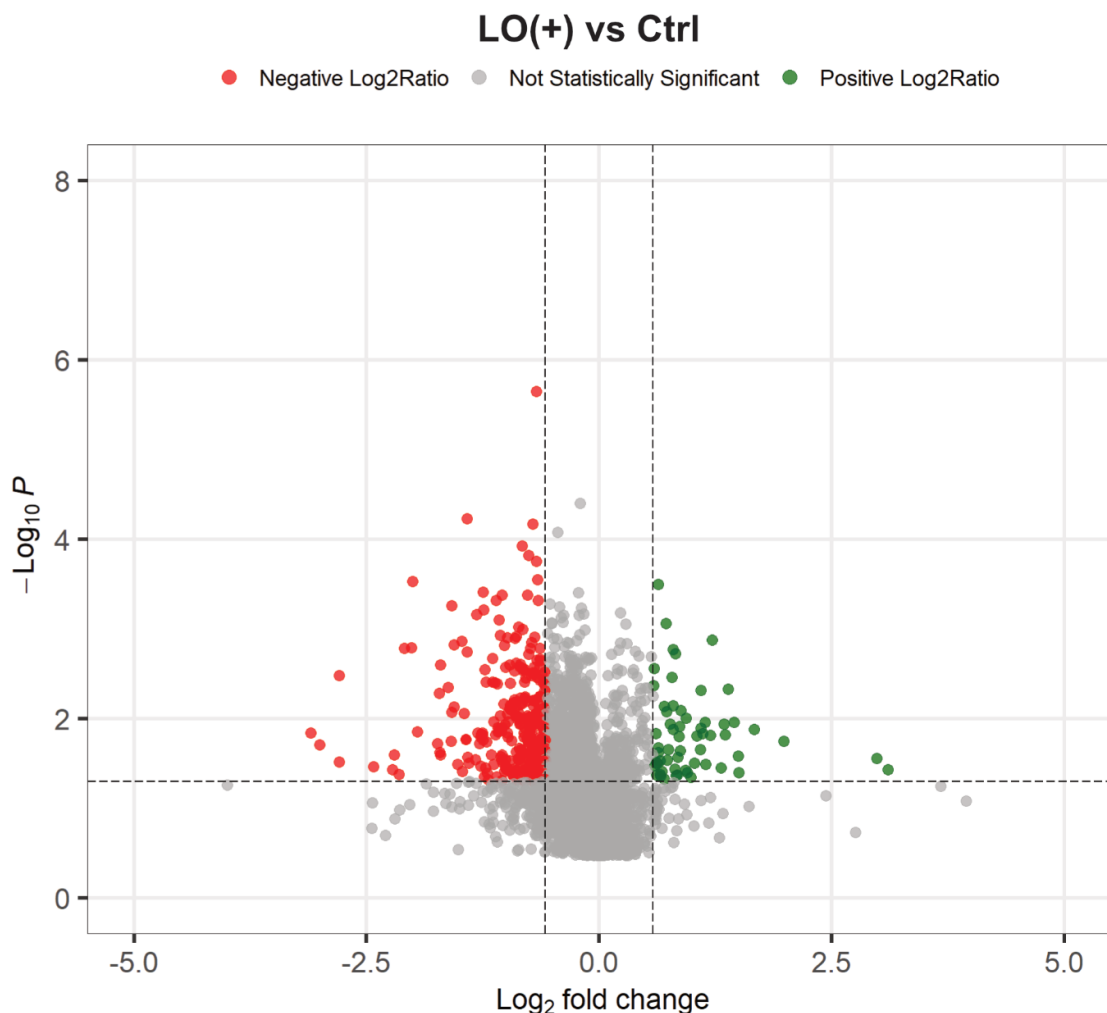


**Figure 32. LO (+) VS Ctrl.** Volcano plots representing under (red) or overexpressed (green) proteins in LO compared to basal state. log<sub>2</sub> fold change of 0.58 and -Log p-value of 1.3 thresholds have been applied.

### 6.15.2 LO(+) + AQP9 vs LO(+)

The aim of this comparison is highlighting the variations induced by AQP9 overexpression, a physiological mechanism seen in human liver of IGT or T2D patients. IPA analysis suggest a downregulation of the Clathrin-mediated endocytosis signalling, with lower levels of actin alpha 2 (ACTA2), actine beta (ACTB), actin gamma 1 (ACTG1), adaptor related protein complex 1 subunit gamma 2 (AP1G2), actin related protein 2/3 complex subunit 3 (ARPC3), casein kinase 2 beta (CSNK2B), coagulation factor 2 (F2), orosomucoid 1 (ORM1), phosphatidylinositol binding clathrin assembly protein (PICALM), protein phosphatase 3 catalytic subunit alpha (PPP3CA), retinol binding protein 4 (RBP4), SH3GL1, SH3GLB1, SNX9, SRC, TFRC. An activation of ATF4 was supported by a modulation of 3 proteins dependent from it. This suggests an activation of the unfolded protein response (UPR) in the ER. This pathway of the UPR leads to the modulation of amino acid metabolism, redox homeostasis and apoptosis. Furthermore, there are hints of the activation of SP1, since 4 proteins were under its regulation. SP1 is connected with the cellular response to insulin stimulus. The downregulation of proteins directly involved in insulin signalling (IGF2) or metabolic processes (HNF4A, ASNS) supports the influence of AQP9 overexpression in the development of insulin resistance. The analysis shows the upregulation of HNF1A, a modulator of the bile acid biosynthesis, the fatty acid transport and biosynthesis, the glucose homeostasis and import. The upregulation of both FABP1, through HNF1A, and HNF1A supports AQP9 participation in promoting the accumulation of lipid droplets. Furthermore, we are describing an upregulation of the Nrf2 mediated oxidative stress response, supported by the downregulation of multiple stress connected proteins (ABCC1, ACTA2, ACTB, ACTG1, AKR7A2, DNAJC10, FKBP5, HSP90AB1, MAPK3, MGST2, MGST3) and the upregulations of those involved in the regulation of oxidative stress (PRXCA, RALB, SCARB1, SOD2). This could be the consequence of the overexpression of peroxiporin (AQP9) at the level of plasma membrane or the outcome of the increased lipid accumulation and subsequent mitochondrial ROS generation, caused by AQP9 overexpression as well. Furthermore, the pathways analysis highlights the downregulation of the oxidative phosphorylation, the glutathione redox reactions, the chemokine signalling, IL-8 signalling and STAT3. Three acylCoA dehydrogenases (ACADS, ACADSB, ACADVL) and long-chain (ACSL1-3-5) and short-chain (ACSS1-2) acylCoA synthetases are upregulated, suggesting increased expression of mitochondrial  $\beta$ -oxidation enzymes due to lipid overload. In LO(+) + AQP9 cells AQP11 is expressed 56% more than in LO(+).

AQP9 overexpression seems to be connected with a downregulation of the clathrin mediated endocytosis signalling and an increased expression of the mitochondrial beta-oxidation enzymes. The overexpression of this protein promotes an increase of the oxidative stress and an activation of the UPR system in the ER. AQP9 overexpression could promote the lipid accumulation. Taken together, the above data suggest an environment under high lipidic and oxidative pressure, promoting inflammatory states and cells death.

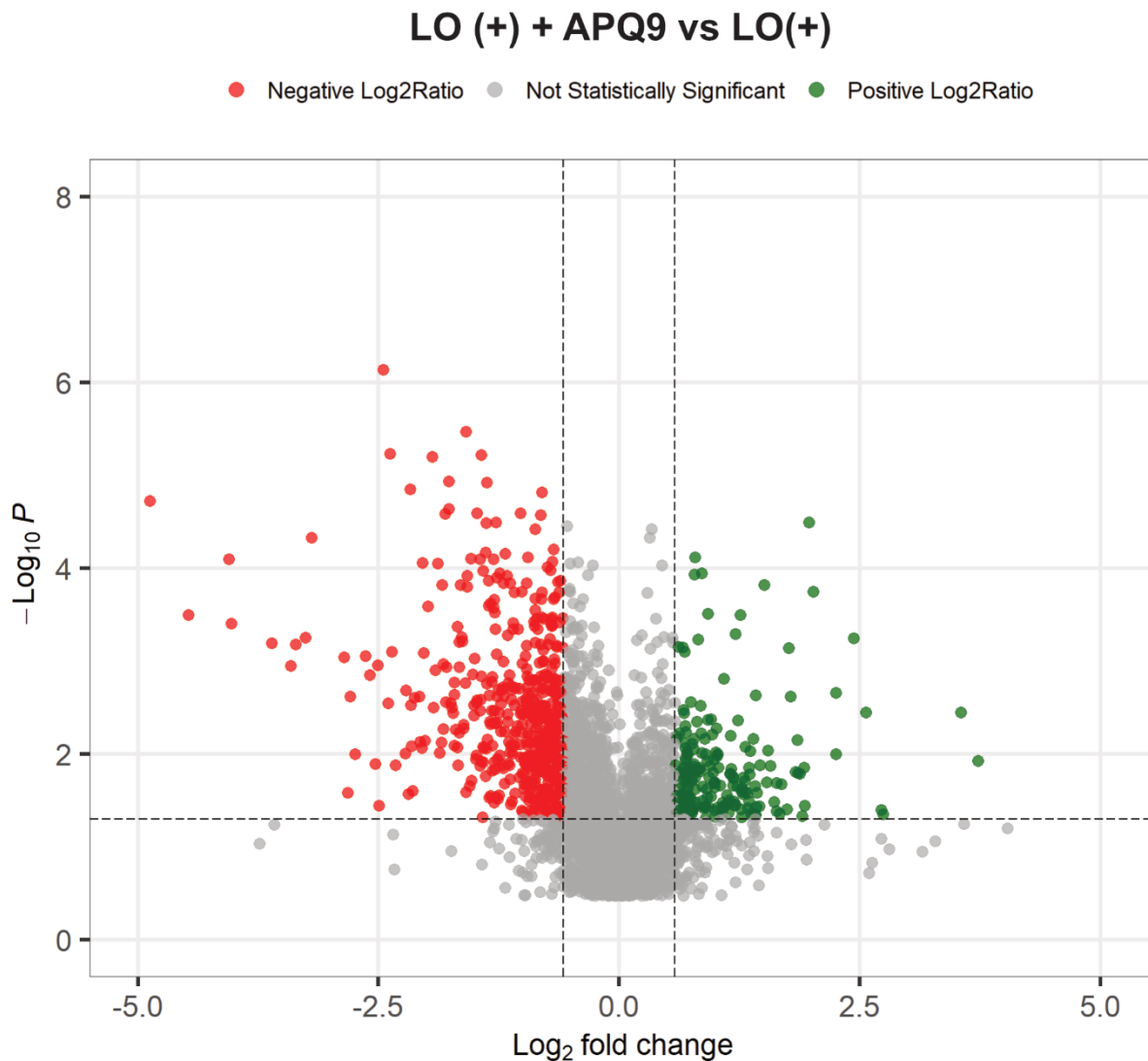


**Figure 33. LO (+) + AQP9 VS LO(+).** Volcano plots representing under (red) or overexpressed (green) proteins in LO compared to basal state. log<sub>2</sub> fold change of 0.58 and -Log p-value of 1.3 thresholds have been applied.

### 6.15.3 LO(+) + AQP9i vs LO(+)

Silencing of AQP9 in lipid overload conditions was performed trying to validate AQP9 as a possible target in insulin resistance and type-2 diabetes development.

The pathway analysis suggests a downregulation of the insulin receptor signalling pathway after silencing AQP9. The approx. 2-fold downregulation of GSK3B was noted in LO(+)+AQP9i cells as compared to the normal LO(+) control. GSK3B is part of the insulin signalling cascade. This is suggesting a connection of AQP9 with insulin signalling, probably thanks to its porin characteristics. The upregulation of the related proteins ABCB11 and APOA support an increased efflux of lipids or bile salts. The downregulation of Keap1, the main modulator of Nrf2, under AQP9 silencing suggests an early activation of the antioxidant response of the cells. This indicates a lower level of inflammation and oxidative stress, being at an early stage of activation of the antioxidant response. This activation could be the result of the closure of AQP9 channels, probably involved in H<sub>2</sub>O<sub>2</sub> efflux from the cells. Furthermore, silencing of AQP9 is promoting upregulation of proteins connected with lipid efflux and downregulation of fatty acids importers FABP1 and FABP5. This confirms the lower levels of lipid droplets in the cells under AQP9 silencing, limiting the oxidative stress too. AQP11 is here 2-fold more expressed than in LO(+), supporting the connection between the expression of AQP9 and AQP11. An involvement of ATF4 is suggested also in this case, but in a limited manner.

The analysis shows a downregulation of GSK3B, one of the proteins of the insulin signalling cascade in absence of AQP9. In the same way, AQP9 absence is associated with a downregulation of FABP1 and 5, free fatty acids importers. In absence of AQP9, AQP11 is more expressed. AQP9 downregulation in a condition of lipid overload seems to bring potential beneficial effects on hepatic cells, decreasing the lipid accumulation and consequently limiting the oxidative stress accumulation and the redox unbalance.

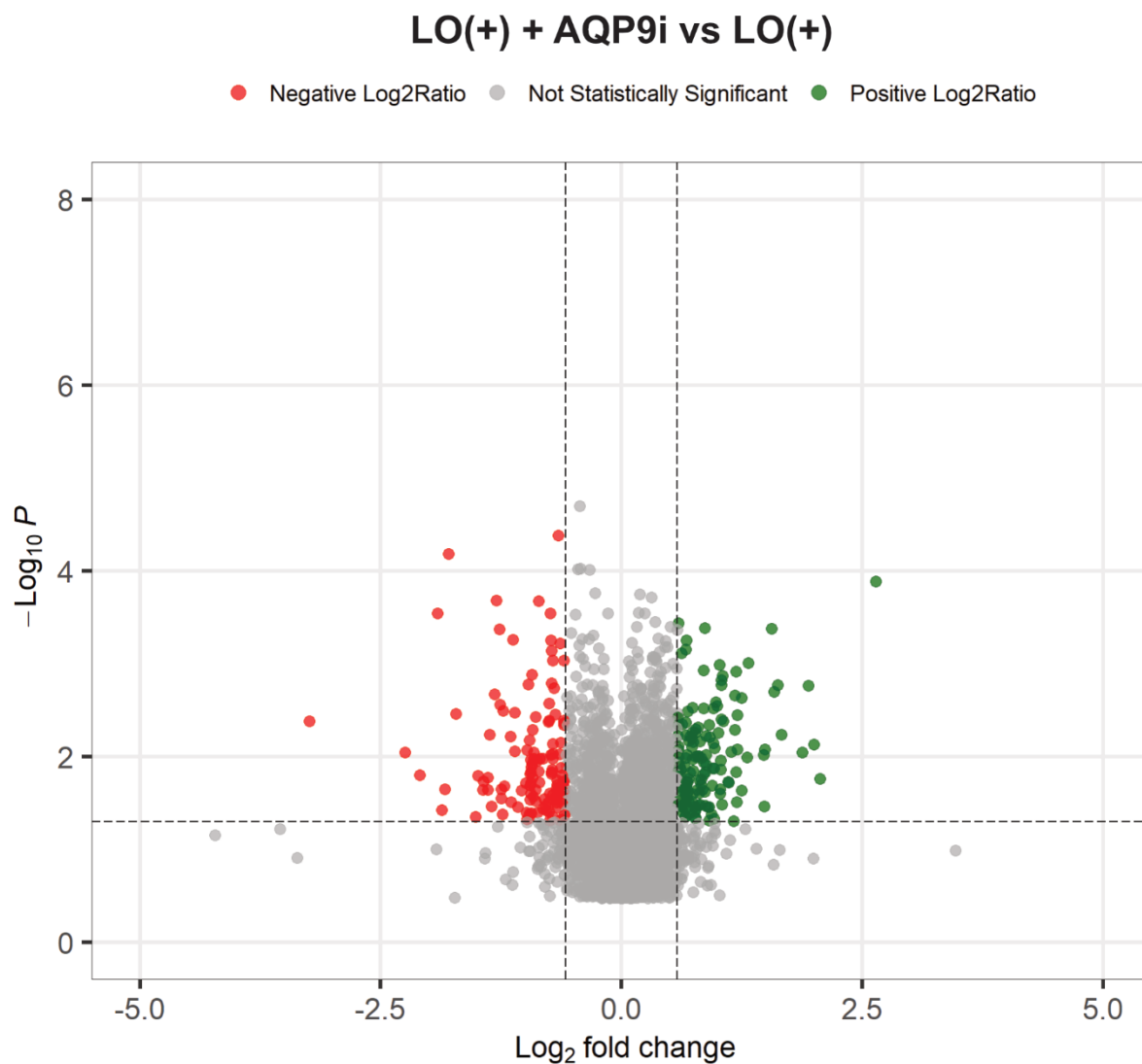


**Figure 34. LO (+) + AQP9i VS LO(+).** Volcano plots representing under (red) or overexpressed (green) proteins in LO compared to basal state. log<sub>2</sub> fold change of 0.58 and -Log p-value of 1.3 thresholds have been applied.

#### 6.15.4 LO(+) + AQP9 VS LO(+) + AQP9i

The last comparison is used to maximize the effect given by the modulation of AQP9 and seeing the pathways and proteins affected more by its presence or absence.

As for the second comparison, upstream regulator analysis revealed activation of SP1 and HNF1A, important in insulin signalling and lipid metabolism. The Clathrin-mediated endocytosis signalling downregulation is confirmed as well. Interesting is the slight downregulation of the Nrf2 mediated oxidative stress response in LO(+) + AQP9 compared to LO(+) + AQP9i. A pathway modification not seen before is the upregulation of the ferroptosis signalling pathway. The extreme conditions of oxidative stress and lipid accumulation bring the cells to the activation of the ferroptosis signal. There is also an upregulation of the apoptosis signalling, another confirmation of the deadly effect of the overexpression of AQP9 under lipid overload. Downregulation of the ERK/MAPK signalling pathway is present as well. The downregulation of the ERK/MAPK signalling goes along with the downregulation of IL-1 and IL-8 signalling pathways. We noticed a downregulation of the glutathione redox reactions when overexpressing AQP9 as compared with AQP9 downregulation, highlighting the problems of the cells in controlling the redox homeostasis and limiting the lipid peroxidation. The attempts of the cells to control the extreme high levels of fatty acids activate pathways of lipid biosynthesis as the stearate biosynthesis 1 pathways, upregulated under AQP9 overexpression. Some key proteins up and downregulation are reported here. SOD1, SOD2 and the mitochondrial transporter TOMM6 are upregulated, suggesting the presence of an extremely high oxidative stress.

The analysis reveals the activation of SP1 and HNF1A, involved in insulin signalling and lipid metabolism. The upregulation of ferroptosis and apoptosis in LO(+) + AQP9 compared to AQP9i suggest the lethality of AQP9 upregulation in LO conditions. Furthermore, the upregulation of SODs confirms the oxidative stress accumulation.

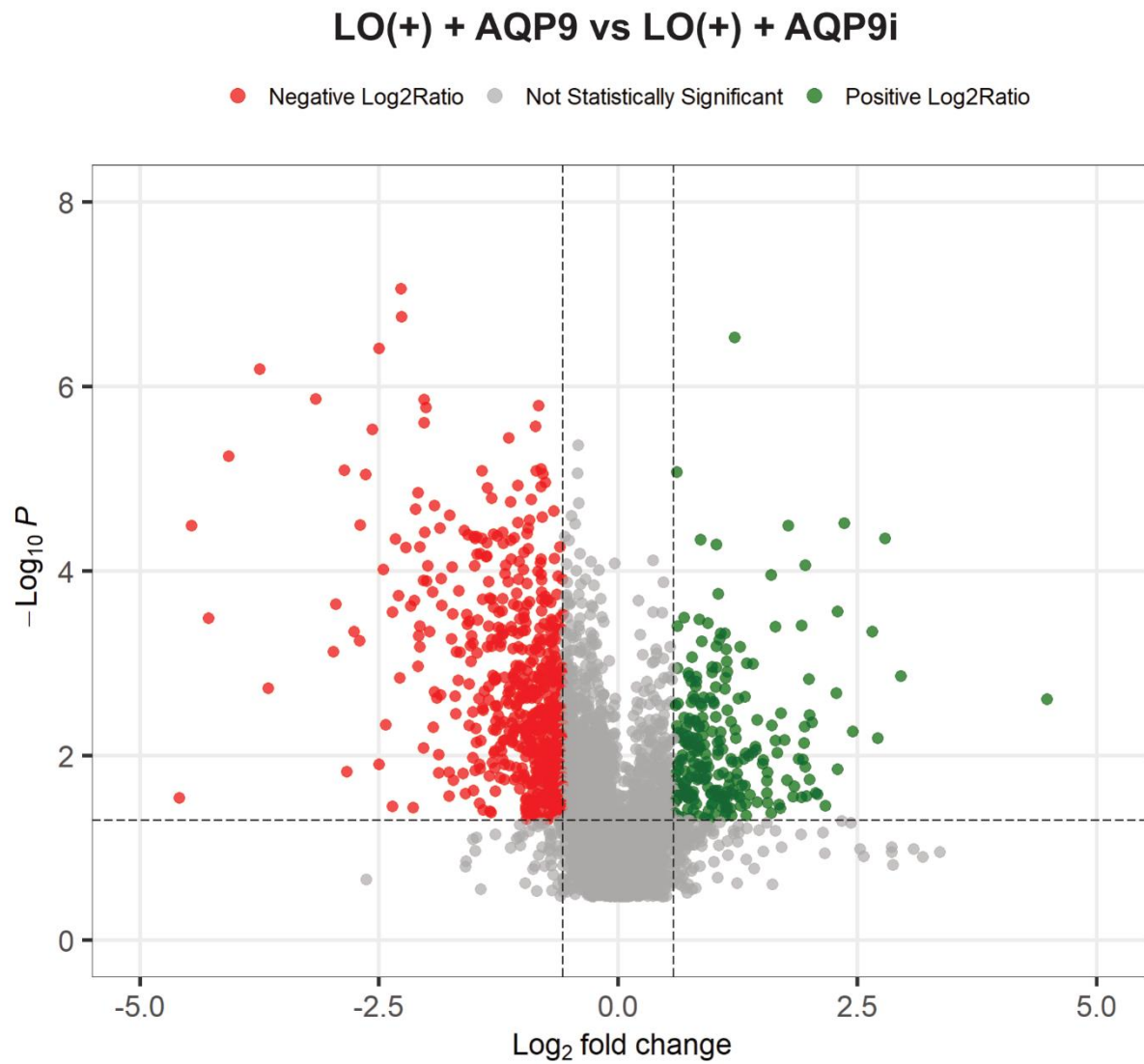


**Figure 35. LO (+) + AQP9 VS LO(+) + AQP9i.** Volcano plots representing under (red) or overexpressed (green) proteins in LO compared to basal state. log<sub>2</sub> fold change of 0.58 and  $-\text{Log}$  p-value of 1.3 thresholds have been applied.

## 7 Discussion

Obesity induced insulin resistance and type 2 diabetes are raising steadily between the population and the discovery of innovative key molecular target is of primary importance. Since the pleiotropic effects of AQPs were not well described earlier, they have been of relative interest. For this reason, there is a need to perform omics studies to better describe the molecular effects of AQPs modulation in the model of hepatic lipid overload. To achieve the best results, it is necessary to improve the current methodologies, which could be then applied to a broader range of samples, including clinical ones.

### 7.1 MS method development

The optimization of parameters in LC-MS is a long and complicated process. Unfortunately, understanding the right time to consider it satisfying is difficult. Therefore, a process following a logic flow was used, starting from liquid chromatography separation, passing through the MS source settings and concluding with the CE. The windows scheme for DIA deserve a separate discussion.

Efficient peptide ionization is more complicated in the  $\mu$ LC regime as compared to nanoflowLC due to greater mass flow of the solvent which requires implementation of additional steps for similar efficiency of ionization. In case of nanoLC, microscopic tip of the glass electrode creates a meniscus with the diameter of approx. 10-20  $\mu$ m, which directly releases droplets into Tylor cone. NanoLC ESI offers the best sensitivity due to highly efficient ionization, which in turn, depends on the initial size of the Tylor cone droplet. Moving towards higher flow rates resolves many problems of the nanoflow LC, namely, ionization instabilities, obstructed electrodes, minute leaks and long system equilibration times due to small flow volumes. Yet in traditional setups, it imposes a significant penalty on ionization efficiency, leading to the decrease in sensitivity, sometimes by the order of a magnitude. To obtain comparable ionization efficiency in proteomic applications in microflow range, as compared to nanoflow range, additional steps of solvent evaporation need to be applied. Initial method development step was performed to optimize source nitrogen flow with the use of a peptide calibration mixture (PepCalMix, **Figure 4**). Nitrogen supplied as Gas 1 was used as nebulizer gas, which when optimized offers better signal stability as compared to pure nanoLC ESI. Nitrogen supplied as Gas 2 was heated to various temperature levels to aid the evaporation of the solvent and subsequently augment the ionization. Nitrogen Curtain Gas was applied to prevent neutral particles from entering the ion optics of the mass

spectrometer and as a counter current removing neutral compounds from the ion stream. The optimal signal intensity was achieved by lowering the nebulizer nitrogen flow (Gas 1) from 35 to 25 when combined with an increase of the Curtain nitrogen gas from 25 to 30. The modification of the Gas 2 flow at its default temperature (RT) didn't impact in any relevant way the ion current signal, probably due to the already efficient ionization in the  $\mu$ LC setup used for the analysis. After the optimization of the nitrogen gases, the temperature and ionization voltage were manipulated to further increase ion current for the selected peptides. Considering only the ion current signal, the best configuration was achieved at high temperature of Gas 2 nitrogen heating gas flow (150°C) and voltage (5000V). Although the optimal conditions guaranteed efficient ionization comparable to nanoflow ESI, the high temperature and ionization voltage quickly degrades ESI probes which needed frequent exchange. The optimal balance between efficiency of ionization and longevity of the ionization probes was achieved at 75°C of nitrogen heating Gas 2 supply and 4500V of ionization voltage. Whenever the priority is to spare the ionization tip, the temperature should be set to 0°C.

The LC approach adopted in the current study, was designed as a trap-elute to ensure the samples' superior cleaning and the protection of the analytical column from particulates. The trap-elute approach significantly prolongs the useful life of the analytical column. As shown in **Table II** and **Figure 5**, 7 different gradients were tested in the aim to obtain the best possible chromatographic resolution of the sample peptides. As compared to targeted sample analysis, non-targeted proteomic analysis requires optimum peak shapes and column resolution across the whole gradient, not only around the retention time of the compounds of interest. The optimization was performed in steps to identify the best performing one. The starting point was set at 2% ACN, matching the organic phase percentage in the sample solvent. The presence of a small amount of ACN allows the wash out of impurities during the trap loading, without an accidental elution of highly hydrophilic peptides. The definition of the 2 step elution gradient (4.5-27.9 and 27.9-40.5) was the crucial step. The starting point of the resolving gradient was set at 4.5% ACN. Which allowed for better resolution of the peaks in the range 4.5-27.9 %ACN where the majority of the sample peptides were eluted from the column. The increased resolving power has been shown through an analysis of the FWHM of selected peptides. In the second step of the elution, some of the peptides were staying in the column till the washing step. For this reason, an increase in the %ACN to 40.5 in 5min yielding non-continuous, stepped gradient was applied. Improving the gradient's start- and

endpoint decreased the FWHM values and increased the identification of peptides. The final minutes of the gradient were used to re-equilibrate the column at the starting ACN concentration. The time needed for the column equilibration was also used for the autosampler wash and sample draw, which allowed for the sample-to sample injection time lasting 1h, with sample loading included. Fully optimized sample loading and resolution on the chromatographic column allows for the processing of 24 samples/day, which is significantly faster than compared to traditional DDA runs lasting approx. 2-4 hours (equipment-dependent), and yielding similar results regarding the number of identified proteins.

The collision energy adaptation described in **table III**, is performed to improve the matching of MS2 peptide fragment ions between the chromatogram ion library collected in DDA mode and MS2 peptide fragment ions collected during DIA sample runs. The standard CE equations used for calculation of collision energy during CID events depend on the  $m/z$  values of the precursor and its charge state. Charge-dependent CID ensures that the optimal fragmentation energy is applied to multiply-charged ions, which in turn generates possibly a richer MS2 spectrum. This results in the ion chromatogram library where each of the library precursor peptide is described by multitude of its product ions. The DIA analysis through its window-based nature performs collision-induced fragmentation simultaneously for all the ions selected within a given mass window, using the CE equation usually applied for double-charged peptide ions. This means that the DIA analysis is not able to reach the fragmentation performance of the charge-optimized DDA analysis. As a result, the fragment-rich ion library created on the basis of charge-optimized DDA runs will contain multitude of the peptide fragment ions which - although having the same mass - will not correspond in the number and intensity to the fragments generated with DIA runs. As both the mass, number and intensity ratios of the fragments need to match between library peptide and the sample peptide for the proper identification by sequence search engine, the mismatch results in a low percentage of identified peptides. To increase the so called library coverage (the percentage of identified library entries present in an experimental sample), the CE equations used for DDA analysis should yield peptide fragment ions similar in distribution and with mutual signal ratios to the ones obtained during windowed DIA fragmentation. To resolve this issue, CE equations were modified to employ significantly softer fragmentation in a charge-independent manner. By softening fragmentation in DDA mode during the library creation step, the resulting library contains a lower number of identified proteins. Still in reality, the library is

missing peptides that would not be efficiently fragmented in the DIA runs, yet the ones included display enhanced similarity of the fragmentation pattern between DDA library and DIA runs, as shown in **Figure 6**. The optimization of collision energies allowed to improve the identification rate of the sample peptides analyzed in DIA mode, reaching a significantly higher yield and library coverage as compared to the standard settings.

## 7.2 *Isolation windows in DIA proteomics*

The efficient design of isolation windows and the proper utilization MS cycle time are crucial for a successful application of DIA-type assays. Windowing schemes employed for DIA are one of the most recently explored features by researchers. Recently, there have been multiple innovations, starting from the introduction of the concept of variable windows [88]. The advances in bioinformatics supported the introduction of new concepts methods, such as MSX or staggered windows [82,86,89,91]. The first widely used windowed DIA approach was introduced by Sciex together with TripleTOF 5600 range of mass spectrometers. The approach called SWATH-MS (Sequential Window Acquisition of All Theoretical Mass Spectra) employed fixed windows covering a mass range approx. 800m/z wide (400-1200 m/z) which contains the majority of peptides resulting from a typical trypsin digestion of the cellular proteome [112]. Subsequently, SWATH-MS was refined to the variable windows approach, which is based on the uneven distribution of window widths, with smaller windows employed in the m/z mass range occupied by the greater number of peptide ions. The efficiency of fragmentation of ions contained within a given window boundaries, and the complexity of the resulting product spectrum is strictly connected with the number of ions present in that window. A fixed wide windows scheme generates very complex MS<sub>2</sub> product spectra, which are dominated by product ions originating from peptides of the highest abundance within a given window. This limits the efficiency of the identification of low-quantity peptides as their fragments are lost in the noise. The results would see some windows flooded with ions and noise and others with an underrepresentation of the peptides. The first idea to optimize the process was the introduction of variable windows. Decreasing the dimension of the windows in m/z regions, with higher ion density, and expanding the windows dimension, in ion-poor m/z range, allows for the efficient management of available MS cycle time and significantly improves the identification and quantitation of the sample proteome [88]. This approach is currently regarded as the gold standard for DIA proteomic analysis on TOF-based instruments. Future improvements will aim towards an increased sensitivity and cycle time, which will allow for a higher number of windows assayed in the

shorter possible time. Regarding the current study, the R tool Swath Tuner was employed to calculate the windows based on the MS1 ion density distribution of a previously acquired DDA sample run (**Figure 7**). This tool facilitates the preparation of the variable windows scheme granting the chance to customize it for different clinical samples or cellular lines.

After establishing the untargeted variable window width method, it was applied to an explorative experiment performed on human liver samples. The HpH-based ion chromatogram library was constructed with an offline fractionation and DDA acquisition of the pooled fractions. The orthogonal features of the HpH fractionation compared to the other peptide fractionation methods grants the best possible distribution of peptides between all the collected fractions and unifies the overall peptide quantity inside of each fraction (**Figure 8**). This approach results in a chromatogram library containing a significant portion of the cellular proteome, granting a uniform identification of proteins in the different conditions, and a controlled CV (**Figure 9**). DIA is naturally controlling the CVs distribution compared to the stochastic DDA. It has been reached a uniform and controlled CV, with a median as low as 10%. This experiment was a way to test the validity of the technique on clinical samples and the best way to launch the current research on AQPs involvement in liver lipid overload. Despite the limited number of preliminary samples, the DIA approach provided excellent reproducibility and a significant proteome coverage at 4433 proteins, showing all the potential of the untargeted approach. With the possibility to check the pathways and all the identified proteins, key candidates in insulin resistance development were identified for the present study.

### *7.3 Untargeted analysis of human liver samples*

Preliminary analysis directed toward the observation of the alternation of large scale protein expression pattern revealed that AQP9 was significantly overexpressed. This channel is connected with both hydrogen peroxide transport and glycerol transport and its overexpression in insulin-resistant T2D obese patients appears to be of major importance (**Figure 10**). Obesity-driven lipid droplets accumulation in hepatic cells and oxidative stress accumulation are two connected events in the development of the disease. Both factors can be influenced by AQP9, whose overexpression could be connected with a response to oxidative stress accumulation. At the same time, the constant overabundance of plasma free glycerol and FFAs in obese patients under ROS-driven overexpression of AQP9 can stimulate hepatic lipid accumulation. In other words, it could lead to a vicious cycle of lipid accumulation promoting oxidative stress and which in turn promotes lipid accumulation. Interesting

observation is the enhanced N-terminal acetylation of AQP9 protein in Met-1 in IGT and T2D conditions. The N-terminal acetylation of AQP9 could be connected with an elevated presence of AQP9 in the plasma membrane. The PTM modification of the N-term of AQP9 protein and the molecular effect of this alternation requires further studies on a larger cohort of patients. Similarly, to AQP9 overexpression, FABPs are up-regulated in IGT patients as compared to ND, showing signs of a coordinated response of those two transporters involved in the lipid droplets accumulation. As T2D patients from the preliminary study received antidiabetic medication, the restoration of the normal phenotype in T2D patients agrees with presented theory (**Figure 11**). A possible modulation of AQP9 expression driven by excessive oxidative stress allows for the continuous access of glycerol, promoting an increased accumulation of lipid droplets. In **Figure 12** we analyzed the enzymes part of the DAG synthetic pathway. None of the two enzymes involved in the first and second steps of the pathways are modulated in IGT and T2D patients. While lipid droplet associated protein LPIN2 is strongly upregulated in IGT and T2D patients. LIPIN2 is responsible for crucial rate-limiting step in DAG and TAG de-novo synthesis, and strong its upregulation suggest extensive activation of this pathway [113]. **Figure 13** is taking into consideration the known markers of oxidative stress in the hepatic cells. Those proteins are part of the cellular antioxidant response displaying up-regulation in presence of redox stress [114,115]. The figure is showing a general tendency to the upregulation of those 3 markers, especially HMOX2 and TXN. The only statistically significant difference is the upregulation of HMOX2 in IGT patients compared to the ND ones, probably due to the small cohort of patients. As expected, we are seeing an increase in the oxidative stress in the liver cells of IGT and T2D patients, which is a common feature of both the insulin resistant state and T2D [75,116]. The oxidative stress accumulation and the overexpression of a hydrogen peroxide transporter as AQP9 open up to its possible role as a relief valve for the excessive accumulation of oxygen radicals in the cells. This would suggest a possible modulation of the AQP9 expression controlled by the oxidative stress, controlled by antioxidant response element.

#### *7.4 In-silico analysis of the promoter of AQP9*

Initial proteomic analysis of the hepatic tissue from IGT and T2D patients suggested that AQP9 expression is regulated by oxidative stress. A bioinformatics analysis of the AQP9 promoter, was performed to test this hypothesis. With the analysis performed on the Lasagna tool, possible transcription factor binding sites were identified in the AQP9 promoter region

**(Figure 14).** The prediction of Nrf2 binding sites with a high score and a low p-value support the theory of direct control of AQP9 expression in response to oxidative stress, suggesting a role of antioxidant response element in the expression of this protein. We found a predicted binding site for Tal1, a transcription factor connected to the family of the NFkB pathway, which is also a modulator of the cellular response to the excessive stress in the liver [117]. This binding site has been confirmed experimentally in erythroid populations from fetal liver cells by Kassouf et al. [117]. AQP9 could be one of the molecules involved in the cells' life/death control, possibly promoting a pro-survival signal thanks to its role as a hydrogen peroxide transporter. Important observation is also the presence of a predicted binding site for STAT1, a transcription factor activated by the EGF signaling cascade and modulating the response of genes important for cell signaling [118]. Furthermore, STAT1 is activated by oxidative stress, bringing to 2 the possible transcription factors modulating AQP9 expression in response to oxidative stress [119]. The two binding sites predicted for CHOP::CEBPA have to be considered too. CEBPA modulates lipogenesis and gluconeogenesis in the liver, CHOP is involved in the ER stress response and is known to negatively regulate the expression of genes induced by CEBPA [120]. Knowing that the lipogenesis is upregulated in the liver cells to cope with FFAs accumulation, an upregulation of AQP9 would promote the entry of glycerol and the production of diacylglycerol and triacylglycerol in the hepatic cells, as confirmed by observation of excessive lipid droplet accumulation [121]. This would promote an overload of the  $\beta$ -oxidation chain, excessive generation of oxidative stress and promotion of ER stress [122–124]. At this point CHOP would bind CEBPA, stopping the upregulation of AQP9. On the other side, the accumulation of oxidative stress could upregulate this channel through NRF2-dependent mechanism, hampering the attempts to limit the accumulation of lipids. In the long term, this would lead to insulin resistance and T2DM, and possibly, hepatic steatosis and NAFLD (non-alcoholic fatty liver disease) development. This underlines the possible role of AQP9 in the regulation of both the redox and the lipid homeostasis of the liver cells.

### *7.5 AQP9 involvement in lipids accumulation in HepG2 cells*

The study of AQP9 role in lipid overload was performed on the HepG2 cell line, a hepatocellular carcinoma cell line. A lipid overload model was developed to simulate the condition of the hepatocytes in obese individuals, exposed to high concentrations of FFAs and free glycerol. The determination of the FFAs ratio used to induce lipid overload, 18:1/16:0 – 2/1 has been chosen to mimic plasma rations of oleate and palmitate. Moreover, above ratio

was proven to stimulate lipogenesis in the hepatic cells and to induce only modest FFA-related toxicity in the hepatic cells [125]. The conjugation of FFA with BSA increases bioavailability of FFA, mimicking FFA transport mechanisms observed in plasma. Different concentrations of FFAs and glycerol were evaluated before deciding the final treatment, observing their physiological relevance. The final condition has been chosen based on its ability to induce a visible effect of lipid overload preserving the viability of the cells. A long treatment of 24 hours has been privileged on the 14h to grant the accumulation of lipids and the development of the lipid overload features. The higher concentration of FFAs especially at longer times decreased cellular viability. Despite the high viability in the different conditions, the number of the viable cells dropped by 50% in 1mM FFAs at 14h and a by 70% 1mM FFAs at 24, denoting a significant FFA-related toxicity. The selected 0.5 mM FFA concentration resulted in acceptable cellular viability and mimicked portal vein absorptive state of FFA concentration (**Figure 15**). The effect of the selected treatment on hepatic cell lipid droplet accumulation was determined microscopically, through two types of assays: by the oil red O stain (**Figure 16**) and by the fluorescent Bodipy probe stain (**Figure 17**) [126,127]. Both experiments confirmed the effectiveness of the treatment. The lipid overload is inducing the accumulation of lipids in the HepG2 cells shown by the increased number of lipid droplets labeled by both the assays. The difference is not limited to the number of lipid droplets in the cells, but it is marked by a bigger average diameter of the lipid droplets in lipid overload conditions. Establishing the best conditions for the lipid overload model was essential in the following study of AQP9 in hepatic lipid accumulation. The lipid overload model was always supplemented with insulin treatment. In physiological conditions of obesity and insulin resistance, the hepatic lipid overload is always accompanied by an increase of the circulating insulin [10]. Insulin concentration in the cell medium was chosen to respect the physiological concentrations of insulin in portal vein of insulin-resistant patients [128,129]. The analysis of the lipid droplets accumulation under AQP9 and AQP11 downregulation under lipid, glycerol and insulin overabundance suggests the role of those AQPs and their relevance to insulin resistance (**Figure 18**). The insulin stimulation promotes the secretion of lipids from HepG2 cells, resulting in a very slight decrease of lipid droplets. The real difference is visible after silencing AQP9, where an almost control phenotype is restored. Silencing AQP11 we can see that the phenotype is strictly connected with AQP9 since the decrease is not significant compared to LO+I. The strong phenotype we see in this condition proposes AQP9 as an important regulator of lipid droplets accumulation. Its overexpression in

IGT patients could be connected with hepatic lipid accumulation, and should be considered as a possible new molecular target for the treatment of obesity-related liver steatosis.

This HepG2 cell-line based model was the foundation of the subsequent experiments performed in the study of the involvement of AQP channels in hepatic lipid overload. Lipid-induced liver cirrhosis is the next step of the liver damage following NAFLD. Healthy liver tissue is significantly damaged by continuous hepatic cell death, cellular proliferation and the deposition of extracellular fibrous matrix. Due to continuous stimulation of the cellular proliferation, cirrhosis often leads to hepatic carcinogenesis. **Figure 19** presents the activation of the early apoptosis response in the different states of AQP modulation. Once again, the lipid overload treatment and AQP9 overexpression in normal cells is proven safe. The interesting event is the strong activation of apoptosis at in AQP9 overexpressed HepG2 cells under the lipid overload, which is 200 times higher than the control. Given the role of AQP9 as the glycerol transporter, this could be interpreted as the effect of glycerol overabundance. The high amount of AQP9 in the cells and glycerol in the medium could lead to glycerol poisoning due to extensive lipogenesis and unregulated accumulation of lipid droplets. By overexpression of AQP9 the HepG2 cells were flooded simultaneously with glycerol which led to the programmed death of the cells. A possible involvement of AQP9 to promote the cell's death cannot be excluded at this point and has to be considered for future studies. Another interesting point is the slight induction of apoptosis stimulated in cells under lipid overload and overexpression of AQP11. AQP11 could be involved in the oxidative stress accumulation in the ER, collecting the hydrogen peroxide produced by the mitochondrial dysfunction due to the excessive generation of oxygen radicals by mitochondrial  $\beta$ -oxidation under lipid overload. The AQP11 overexpression acting as safety mechanism for the increased mitochondrial ROS emission could drive to a faster accumulation of  $H_2O_2$  inside the ER, promoting ER stress. The decreased access of glycerol, due to physiological levels of AQP9, seems to limit the damages induced by this overexpression. On the other side, the silencing of both AQP9 and AQP11 in two different samples under lipid overload did not bring to the activation of apoptosis in a significant way. The strong effect connected with AQP9 modulation has to be considered in the evaluation of insulin resistance development. The upregulation of this channel is lethal in this cellular model and the upregulation of AQP9 was noticed in both IGT and T2D patients compared to ND. A possible lack of control in the down-modulation of AQP9 could be connected with the development of liver insulin resistance and subsequently type-2 diabetes. The multiple predicted binding sites for

transcription factors involved in oxidative stress signaling and lipids accumulation, and the strong effect given by its upregulation in the lipid overload model highlights the key role of AQP9 and the importance of its fine modulation. AQP9 modulation seems to be strictly connected to the expression levels, but the possibility of a PTM modulation cannot be excluded at this stage.

#### 7.6 *AQP9 and oxidative stress*

The oxidative stress flows and accumulation were analyzed. Using HyPer 7.2 as a H<sub>2</sub>O<sub>2</sub> sensitive probe to track its accumulation and flow, the aim was seeing the H<sub>2</sub>O<sub>2</sub> wave induced by the activation of the insulin receptor in a live imaging experiment. We expected to see a decrease in the H<sub>2</sub>O<sub>2</sub> flow coming from the insulin receptor under lipid overload, due to a possible oxidative stress downregulation of the insulin signaling cascade. Being INSR a TKR, AQP9 could be modulated in a way similar to AQP8, closing the pore and impairing the signaling in presence of an oxidative stress [23]. As shown in **Figure 20** technical difficulties that limited the sensitivity of the probe and impeded us to see significant differences in the conditions. The diminished signal after the addition of DTT, a reducing agent, was expected, but the ramp before the addition of insulin was not. It could be due to the already high signaling activity coming from EGFR or other TKRs, making it harder to distinguish a signal coming from insulin from the other background signaling. For future approaches, the introduction of a starvation phase has to be considered before the acquisition. Lowering the basal signal could allow us to see differences in H<sub>2</sub>O<sub>2</sub> flow induced by insulin and lipid overload treatment. Furthermore, a version of HyPer 7.2 linked to the plasma membrane has been used, which has a lower signal compared to the counterpart floating in the cytosol and could produce more noise. Using HyPer in the cytosol could help in detecting a stronger signal. Alternatively, the creation of a chimera carrying HyPer linked to AQP9 could help to increase the sensitivity on the H<sub>2</sub>O<sub>2</sub> flow through this AQP.

The analysis of the transport capacities of the cells under different treatments (**Figure 21**) has been performed using HyPer 7.2 in the cytosol of HepG2 cells. The aim was to determine if the lipid overload could influence the flow of H<sub>2</sub>O<sub>2</sub> in a relevant way. The experiment is set to check the transport from the outside to the inside of the cell through the AQP channel, because it is the most feasible approach to control multiple parameters, such as the concentration of extracellular hydrogen peroxide added during the experiment. This does not exclude the difference is physiologically relevant on the reversed flow of H<sub>2</sub>O<sub>2</sub>. Most probably both influx and efflux of H<sub>2</sub>O<sub>2</sub> are contributing to the modulation of the porixporins

by cells trying to keep the redox homeostasis. The partial but significant decrease in  $\text{H}_2\text{O}_2$  transport under lipid overload could be an example of a balanced modulation of the  $\text{H}_2\text{O}_2$  levels influenced by multiple transporters. At the current state of the knowledge regarding AQP9 physiology, it is possible that one of the AQP transporters is closed by oxidative stress (as observed in case of AQP8), another non-modulated one could allow for the transport of  $\text{H}_2\text{O}_2$  (e.g. AQP9). Testing both of them we could see a different modulation, with AQP8 probably involved in the partial inhibition of the transport under lipid overload. We cannot confirm AQP9 participation in it, but neither completely exclude it. The silencing of AQP9 under lipid overload shows that there is still hydrogen peroxide transport in this condition associated with AQP9 presence. It is plausible that AQP9 is not the main actor in the inhibition of  $\text{H}_2\text{O}_2$  transport under lipid overload. A similar pattern of transportation of lipid overload and lipid overload with silenced AQP8 supports a possible role of AQP8 in the closure of the transport, especially knowing that this AQP is modulated by oxidative stress [65]. Nevertheless, we can't exclude the co-participation of other transporters, as AQP3, a known  $\text{H}_2\text{O}_2$  transporter and involved in the insulin signaling of McArdle hepatocytes [22].

Lipid overload of hepatic cells is associated with obesity and is known to induce oxidative stress and ER stress in the liver cells (**Figure 22**) [75,116,130]. The lipid overload induced in HepG2 can mimic the conditions typical of insulin-resistant patients. The  $\text{H}_2\text{O}_2$  exponentially accumulates in the ER starting after around 10 hours. This result is supporting the idea of AQP11 as a channel connecting ER and mitochondria in certain situations, especially considering AQP11 presence in the mitochondrial associated membranes (MAMs) [51]. The mitochondrial dysfunction induced by the lipid overload and the parallel increase of the  $\text{H}_2\text{O}_2$  in the ER suggests the fact that AQP11 is channeling the  $\text{H}_2\text{O}_2$  in excess inside the ER to buffer the oxidative stress in the cell. This compensatory mechanism would temporarily preserve the cells from oxidative stress and at the same time, it would promote the activation of the ER stress to actively find a solution to this problem.

**Figure 23** helps us to achieve a better understanding of the oxidative environment of HepG2 cells. Using HyPer in the ER lumen and anchored to the membrane outside the ER lumen we could elaborate a theory regarding the presence of a reductive shield around the ER membrane. The delay in the reaction of HyPer to the  $\text{H}_2\text{O}_2$  just outside the ER membrane suggests the presence of a highly-reductive environment provoking a difference oxidative state of HyPer when it is in the proximity of the ER membrane. Furthermore, a digitonin treatment disrupts this effect, granting an efficient activation of the probe and suggesting the

cytosol-soluble nature of the molecular factor responsible for the presence of the reductive shield. The presence of ER lumen inside the ER confirms the integrity of the ER after the treatment with digitonin. In support of this theory, we show an abnormal oxidative state of HyPer 7.2 when stably expressed in the cytosol of HepG2 cells. The completely different distribution of HyPer when excited at 405 or 488 in the same cells is of extreme interest. The super-oxidized and super-reduced state of HyPer in different parts of the cytosol supports the idea of an extremely reductive environment in the deeper part of the cytosol, right next to the ER, with oxidative conditions present on the outskirts of the cell body. The reductive shield around the ER could be essential for the preservation of the cellular physiology and the optimal function of the ER. A possible perturbation of this shield driven by the oxidative stress due to the lipid overload could be fundamental in the onset of insulin resistance and T2D. Another point to be discussed is the inability of the cells to transport H<sub>2</sub>O<sub>2</sub> inside of the ER. HyPer is functional in the ER of HeLa cells. On the other side, it has been published that HyPer is not working in the ER of secretory cells because of the extreme oxidative environment of the ER [131]. In the 20 hours acquisitions performed in this research to unveil the oxidative stress accumulation in the ER, HyPer was oxidated by the accumulation of hydrogen peroxide in the ER. For this reason, it can be stated that the probe is functional in the ER of the cells and the oxidizing environment of the ER is not impairing its function. The problem seems to be connected with the transportation of externally added H<sub>2</sub>O<sub>2</sub> arriving from the cytosol, where AQP11 should grant its access. AQP11 could be isolated in the MAMs in the secretory cells in a normal state, limiting the access of cytoplasmic H<sub>2</sub>O<sub>2</sub>. In this way, it would be impossible to transport external added H<sub>2</sub>O<sub>2</sub>, but it would be plausible to discharge the H<sub>2</sub>O<sub>2</sub> produced by the lipids-induced mitochondrial dysfunction directly in the ER. The other possibility would be active filtering of H<sub>2</sub>O<sub>2</sub> by the reductive shield, but it seems much less probable since HyPer on the ER membrane is still sensing the H<sub>2</sub>O<sub>2</sub> variation even if delayed.

### *7.7 Advanced DIA development*

To further elucidate the involvement of AQP modulation on HepG2 under lipid overload the untargeted proteomic approach was employed to identify possible other molecular players. To gain major flexibility, essential for the analysis of different experiments, the DIA approach was further developed. The second step of an advanced DIA saw a heavy introduction of in-silico work. The previously developed approach was already working at optimal levels but requiring extensive preparatory work connected with the creation of the ion library. The

building of extensive and extremely accurate libraries requires the investment of instrument and operator times. All this preparatory work is justified just in the case of extensive utilization of the libraries. The DIA proteomics world is lately opening to increase the flexibility of this method relying on bioinformatics development. New software and methods become available every few months, continuously pushing the boundaries of this discipline. Two different types of approach were analyzed in this phase: a completely in silico method that does not require the preparation of an ion library (directDIA) and a hybrid approach requiring the preparation of a chromatogram library starting from gas phase fractions run in DIA mode (Staggered windows). We did not expect those approaches to improve the results obtained from the first method developed. The goal was to find the best method to match the results obtained with the current time-consuming and burdensome method. The staggered windows method has been developed on orbitrap-type instruments, with a deconvolution algorithm optimized to give its best in these instruments. The challenge was to adapt and optimize the settings on TripleTOF 6600+ to obtain the best results possible with the original deconvolution algorithm. As an additional complication, the instrument employs a  $\mu$ LC HPLC connected to the TripleTOF, implementing for the first time this combination to an advanced DIA workflow. As shown in **Figure 24** the starting point for the staggered windows method development was the preparation of ion library. Starting from a configuration that theoretically should give optimum results. The speed of the TripleTOF allowed for the implementation of gas phase fractionation approach with the use of very narrow 2 m/z overlapping windows. After combining all the GPF runs it translated to a library based on 1 m/z windows. On the DIA runs the fastest possible acquisition was selected, deploying all the speed of the TripleTOF to split the 400-1200 m/z range into 16 m/z windows, for a total of 50 staggered windows (total of 100) collected for 25ms, with the initial MS1 full scan collected for 250ms. This translated to a cycle time of approx. 2.8 seconds, yielding approx. 10 data points per chromatographic peak. Particular care was taken in the equilibration of the cycle time of the tested methods, and unification of all the MS-related settings to not favor any of the methods. The directDIA was tested on both the variable windows and staggered windows approaches, to test the performance of the current library-less approach with the use of different windowing schemes. The preliminary analysis of the ion libraries' depth evidenced significant distance between the two approaches as this initial step, where the gas phase library was able to cover only a third of the HpH library identifications (**Figure 25**). The performance of the STW-based approach was not comparable to VWW approach as well, with a huge disproportion of the yield toward the HpH/VWW approach. The huge coverage of

the HpH library shows all its power in the Venn diagram, where the variable windows width runs hit a significantly higher number of proteins, peptides and precursors compared to the staggered window runs. Moreover, over 90% of the proteins identified by the staggered windows runs are identified also by the variable windows width runs. These results show that the VWW is better when compared to the 2mz-50STW approach, and there is some variability in the identifications dependent on the method used for running the samples. The directDIA also showed the limitations of the faster approach at its current implementation, reaching results inferior to the ones of the staggered windows. Interestingly, the difference in the yield between variable windows and the staggered windows approach is consistent.

To improve the library depth and STW analysis results, both the dimension of the windows of GPF runs and STW runs and collection time (dwell time) was increased. GPF runs collected with 4 m/z windows significantly improved the coverage of the library, showing that using all the speed of the TripleTOF is not feasible as combined with  $\mu$ LC HPLC. This non-favorable outcome of 2m/z GPF library combined with 50STW method could be result of lower sensitivity imposed by higher source eluent flow, as compared to nanoLC setup and shorter-than optimal collection times enforced by very fast window switching. Doubling both the window width and collection time (to 4m/z and 50ms, respectively), significantly improved library performance.

To improve the library depth and STW analysis results, both the dimension of the windows of GPF runs and STW runs and collection time (dwell time) was increased. GPF runs collected with 4 m/z windows significantly improved the coverage of the library, showing that using all the speed of the TripleTOF is not feasible as combined with  $\mu$ LC HPLC. This non-favorable outcome of 2m/z GPF library combined with 50STW method could be result of lower sensitivity imposed by higher source eluent flow, as compared to nanoLC setup and shorter-than optimal collection times enforced by very fast window switching. Doubling both the window width and collection time (to 4m/z and 50ms, respectively), significantly improved library performance. Other possible drawback of pure GPF library is the misalignment of the retention times between individual GPF runs, which are not corrected by the addition of iRT peptides due to narrow coverage of the individual GPF fractions. To correct this issue GPF library was supplemented with DDA runs covering the full m/z range of GPF fractions (**Figure 26**). The addition of 3 DDA runs to the GPFs significantly improved the coverage of both the 2 and 4 m/z libraries, bringing the 4 m/z library to levels more than acceptable. To ensure similar treatment for both the methods of library generation, DDA runs

were also added to the HpH library runs. The wide m/z coverage of each of the HpH fraction runs did not leave much margin for the improvement, but it gained some IDs from the addition of the DDA runs. Even more interesting is the significant improvement of the retention time alignment of the GPFs due to the DDA runs inclusion. The presence of iRTs peptides in GPFs and DDA runs helps the coordination of the GPF on the full range covered by the DDA runs. This improves also the reproducibility of the retention time of this library, allowing to reuse of the same GPF library multiple times. One of the minor limitations of the previous implementations of GPF based libraries was the necessity to run the library runs every time in the middle of the DIA-based sequence to ensure the precise retention time match between DIA runs and GPFs [90,91].

The results of the analysis of 100VWW and 50STW using the different libraries confirmed the hints given by the libraries' depth. The hybrid GPF+DDA libraries improve the identifications of precursors, peptides and proteins in all the conditions except for the proteins identified by 100VWW. The precision of the retention time alignment of this library grants the identification of the same number of proteins without. The staggered windows chromatogram library is based on 2 steps: the implementation of the 4 m/z windows and the addition of DDA runs. Both of these actions brought positive results (**Figure 27**). The analysis of the width of extracted ion chromatograms (XIC) confirms the improved retention time stability achieved in both VWW and STW. The directDIA approach displays inferior performance, especially with the staggered windows approach.

The optimization of the windowing schemes of the DIA runs was performed to improve the performances of the 50STW approach. The VWW schemes were improved as well to ensure the maximum comparability. Methods were compared based on the similar collection time e.g. 40STW VS 75VWW (approx. 30ms dwell time per window) and 25STW VS 50VWW (approx. 50ms dwell time per window). A similar cycle time was ensured for all the 6 schemes (**Figure 28**). The number of comparisons was limited analyzing the new windows schemes runs on the best performing libraries. This refinement step improved both VWW results and STW results, working best for the latter. The 50STW displayed the best results with significant improvements as compared to other STW-based methods at the level of precursors, peptides and proteins (**Figure 29**). This final STW method closed the gap between HpH/VWW approach and GPF/STW-based approach, yet the STW approach yielded results significantly faster, due lack of time-consuming HpH sample fractionation. Despite this, the extremely encouraging results show the good performance of this setup of the STW method.

Comparing the statistics of the new methodologies, the STW show good results. Checking the CVs at the level of the quantified proteins (**Figure 30**) we notice the persistent problems of the 50STW approach, which are corrected by increase in the width of STW windows and collection time. All the others have similar CVs, with the lowest median CV reached by the 25STW. Binning the CVs based on m/z ranges we could notice the real improvement brought by the STW methods as compared to VWW ones. STWs grant major control on the stability of the CV along the m/z range. In detail, the VWW loses control of the CV at high m/z values due to the increasing width of windows in the higher mass ranges, while it is extremely controlled by the staggered windows. Similarly, by binning the identification rate along the m/z range STW show another advantage. VWW at high m/z ranges shows not only the inferior control of the CVs, but also of inferior identification efficiency which drops almost by a third compared to lower m/z ranges. Once again, the STW shows a more regular pattern, keeping a constant identification efficiency also at high m/z ranges.

The methods were validated running a biological experiment with both the best DIA approaches: HpH Hybrid library with 75VWW and GPF Hybrid library with 40STW. We compared 2 conditions from HepG2 cells, the control and the lipid overload. From the analysis of the results, we could say that the STW approach reaches satisfying results granting a high number of identified precursors, peptides and proteins. The analysis of the volcano plots (**Figure 31**) shows an equilibrated distribution of proteins with both the MS techniques and highlights a similar pattern in the distribution of under- and over-expressed proteins. The slightly inferior yield of the new approach is compensated by its superior speed and a higher quality of the results, as confirmed by a lower CV% of the quantified proteins.

#### *7.8 Untargeted analysis of HepG2 under lipid overload and AQP9 modulation*

The untargeted analysis performed on the different conditions aimed to investigate the main changes induced by the lipid overload on the cells and the effects that the modulation of AQP9 could bring. This analysis confirmed the main effects of the LO(+) treatment, as underlined by the altered protein expression of mitochondrial proteins indicating the induction of mitochondrial dysfunction and reduction of oxidative phosphorylation, together with an upregulation of the proteins involved in the the biosynthesis of diacylglycerol and the accumulation of lipid droplets. This trend generally follows what was seen in the preliminary study on human liver samples, with a similar upregulation of the same key enzyme of DAG and TAG synthesis - PLIN2.

We showed with microscopy experiments on HepG2 cells that AQP9 overexpression in cells under lipid overload had dramatic effects, leading straight to strong activation of an apoptotic signal, probably connected with an extreme redox unbalance. The proteomic analysis performed with the use of the preferred GPF/STW method confirms the previous discovery, adding some information. Results suggest the insurgence of mitochondrial dysfunction and reduced oxidative phosphorylation, together with an accumulation of lipid droplets. The lipids accumulation could be aggravated as some of the enzymes are upregulated compared to the normal LO(+). The worsening of the conditions is supported by an upregulation of the Nrf2 mediated antioxidant response, a probable activation of the unfolded protein response and the traces of apoptotic signals. The fact that AQP9 upregulation is connected with the modulation of proteins connected with insulin signaling and lipid droplets accumulation underlines its fundamental role in the development of hepatic insulin resistance. The direct connection between AQP9 upregulation and HNF1A upregulation and its target FABP1 upregulation constitute a strong clue of an AQP9 role in modulating the access of FFA entry into HepG2. Moreover, clathrin-mediated endocytosis facilitates the uptake of nutrients and the internalization and recycling of various receptors on the surface of the cells. This upregulation following AQP9 overexpression could be connected with an attempt to block the nutrients uptake. On the other side, blocking the recycling of tyrosine kinase receptors could be involved in the development of insulin resistance, given the TKR nature of the INSR.

Silencing of the AQP9 protein in HepG2 cells under the lipid overload is producing beneficial effects compared to the lipid overload condition. There is no detectable apoptosis activation or a strong upregulation of the antioxidant response. The activation of the antioxidant response is at an early stage since it is reported a downregulation of the Keap1, Nrf2 switch. Interestingly, there is an association between the silencing of AQP9 and the downregulation of the insulin receptor signaling pathway, inferring a possible role of AQP9 in the insulin signaling cascade. This would be based on its peroxiporin properties of the AQP9, in a way similar to the one described for AQP8 first and AQP3 later [22,23,52,65]. Most important, the downregulation of AQP9 seems connected with an improved lipid efflux from the hepatic cells and a decreased import of FFA as suggested by FABP1 and FAB5 downregulation. This, together with the increased accumulation of lipids under the AQP9 overexpression, confirms the strict relationship between AQP9 channel and the lipid droplet accumulation. Microscope experiments on HepG2 cells confirmed the decrease of lipid accumulation in AQP9-silenced cells under lipid overload. On the other side, AQP9

overexpression promoted a higher accumulation of lipids. Based on all of these confirmations, AQP9 can be proposed as the main regulator of FFA import in the HepG2 cells, gaining an important role in the lipid overload and the development of insulin resistance. The result of all of this is a diminution of the oxidative stress and an improved resistance of HepG2 to a lipid challenge.

The direct comparison between overexpressed and silenced AQP9 states unveiled additional information. Between all the confirmed pathways seen before overexpression AQP9, a particular downregulation of Nrf2 mediated oxidative stress response was observed. This result is opposite to the one seen in the second comparison, suggesting that sensitive redox system deserves more elaborated reasoning. A possible explanation could be connected with the modulation of AQP9. The silencing of AQP9, with the subsequent trapping of H<sub>2</sub>O<sub>2</sub> inside the cells, could pre-activate the antioxidant response. The high levels of antioxidants could limit the oxidative stress in the AQP9 silenced condition, showing higher levels of HMOX1 compared to LO(+) with AQP9 overexpression. The upregulation of the ferroptosis signalling pathway is another message of the high stress in these cells. The mitochondrial dysfunction and significant ROS accumulation in LO(+) + AQP9 leads to lipid peroxidation and induction of ferroptosis-driven cell death. The downregulation of MAPK, IL-1 and IL-8 signalling in this comparison has to be considered as well. AQP9 could have a role in disrupting the signalling cascade at the level of receptors, underlining its possible importance also in cancer development.

Last, but not least, AQP11 modulation has to be considered. The variations in the expression of AQP11 under lipid overload suggest the relevance of this porin in the cells under lipid overload. It's contrasting modulation when AQP9 is over or under expressed is the first experimental correlation supporting the theory of an AQPs network in hepatic cells proposed previously [132]. Lipid overload heavily downregulates the expression of AQP11 by approximately 2.5 fold. A slight upregulation of AQP11 is visible when under AQP9 overexpression compared to LO(+). When AQP9 is silenced, AQP11 is upregulated, reaching over 2 fold compared to LO(+). This suggests a downregulation of AQP11 under stress and extreme stress conditions. When silencing AQP9, heavily limiting the effects of lipid overload and stress, AQP11 is upregulated, restoring expression levels similar to the control condition. AQP9 and AQP11's strict relationship with hydrogen peroxide makes their crosstalk essential in maintaining redox homeostasis in the HepG2 cells.

Considering the information collected the theory of an AQP's network involved in insulin resistance and T2D development finds another confirmation [132]. Both AQP9 and AQP11 look to be involved in the process of lipid droplets accumulation and the subsequent oxidative stress accumulation derived from it. A common modulation of those AQPs cannot be shown at the moment, but the effects induced by lipid overload could modulate both the proteins strictly involved in oxidative stress.

#### *7.9 AQPs relevance in lipid overload and insulin resistance development in hepatic cells*

The results of the multifaceted research leads to a variety of conclusions. Starting from the analysis of a limited number of human liver samples from obese patients at the preliminary stage of the work, a project to study the lipid overload effects on HepG2 cells was developed. The proteomics analysis on a limited number of obese IGT or T2D individuals confirmed currently known information about the stages of this disease, as the overexpression of proteins connected with the lipids accumulation and the development of oxidative stress in the liver. AQP9 assumes a main role for its possible participation in both lipid accumulation and oxidative stress. The bioinformatics analysis of the promoter of AQP9 gene predicted binding sites for Nrf2, Tal1 and STAT1 between the others, three transcription factors involved in the antioxidant response, NFkB pathway and signaling respectively. Furthermore, CHOP::CEBPA binding sites highlight a possible involvement of AQP9 with ER stress and lipid accumulation. AQP9 was studied on HepG2 cells, where a successful model of lipid overload mimicking the physiological lipid overload in the liver of obese patients was established. The development process allowed for the selection of the best conditions: 0.5mM of FFA mix (Oleic acid : Palmitic acid - 2:1) for 24h supplemented with 100µM glycerol and 15mM glucose. This treatment promotes the accumulation of lipids preserving the viability of the cells. The analysis of the activation of the early apoptosis confirms the safety of the treatment for the cells. The upregulation of the AQP9 under lipid overload as observed in the limited number of clinical samples results in toxicity for the cells, showing an extremely high activation of the Caspases 3 and 7. The upregulation of AQP11 increases the apoptotic signal too, but in a limited way as compared to AQP9. The silencing of these two AQPs does not induce a significant apoptosis activation. Interestingly, the downregulation of AQP9 under lipid overload prevents the accumulation of lipid droplets, restoring almost completely the control phenotype. The silencing of AQP11 in the same conditions does not produce the same effect, suggesting that AQP11 is not involved in controlling lipids accumulation in HepG2 cells.

We also enriched the knowledge about the peroxiporins, despite we could not detect a difference between control and lipid overload HepG2 cells in the  $H_2O_2$  levels after the stimulation with insulin. It was demonstrated that the lipid overload is limiting the flow of hydrogen peroxide through the membrane of the HepG2 cells. The impaired transportation is not attributable only to AQP9, but more probably to AQP8 modulation. The possibility of the participation of another AQP, as AQP3, cannot be excluded until further experiments are performed. The lipid overload is inducing an increase of oxidative stress in the endoplasmic reticulum, mirroring the consequences induced by the lipid overload in human hepatocytes. Analyzing the behavior of HyPer around the ER membrane the presence of a reductive shield around this membrane is hypothesized. The probe reactivity is lower than expected around the ER membrane indicating that a strong reducing environment limit the effect of the hydrogen peroxide added. The normal reactivity can be restored by permeabilizing the plasma membrane with digitonin, which supports the volatile essence of the reductive shield. Moreover, HyPer seems more reduced at the basal state in the inner part of the cytoplasm, next to the ER membrane, while it is essentially oxidized next to the plasma membrane, which indicates that antioxidative shield in HepG2 displays intracellular gradient towards the important cellular organelles such as nuclei.

Taken together, all presented data confirms a primary role of AQP9 in the lipid droplets accumulation in HepG2 cells under lipid overload, revealing it as a crucial gatekeeper of the cells whose modulation is crucial for the cells' life. It also suggests a possible role of AQP9 in the lipid-driven development of insulin resistance and T2D, given by a possible deregulation of a multitask protein involved in both lipid accumulation and hydrogen peroxide flow. AQP11, as the main  $H_2O_2$  transporter of the endoplasmic reticulum, is a candidate to have a role in oxidative stress accumulation under lipid overload. Both of them deserve to be studied as possible targets in the development of insulin resistance in the human liver.

In the course of this project, the untargeted proteomics analysis for experimental HepG2 and clinical samples was developed. First, a time-consuming but very precise method was established, ensuring a deep coverage of the cellular proteome of both the HepG2 cells and clinical samples. The real innovation of this first part was connected with the LC method used for the approach. An efficient DIA method connected with a micro LC system was studied and applied, shortening the overall analysis times but keeping extremely high performance of more traditional VWW approach. The combination of MS parameters optimization together

with  $\mu$ LC and variable windows schemes resulted in a high-throughput, reliable and stable method for the analysis of the experimental and clinical samples.

The second step of development involved the application of the staggered windows approach, a bioinformatics-based DIA method, on a TOF-based mass spectrometer which was not previously achieved by other research groups. The adaptation of this approach required the elaboration of multiple windowing schemes for the GPF fractionated library and the STW runs. The results were similar to the ones obtained with the extended method, granting a relevant spare of time and resources. The combination of the hybrid chromatogram library with the 40STW windows schemes showed the best results in terms of identifications and coefficient of variation. STW ensured also major stability in the control of identifications and CV at higher  $m/z$  compared to the standard method.

In conclusion, we developed two valid and efficient approaches for the untargeted proteomics analysis, combining the most recent advances in the proteomics world. The test of the GPF-STW method with the HpH-VWW was performed on a simple biological experiment and then applied to the study of AQP9 modulation in the HepG2 model of lipid overload.

## 8 Conclusions

The results of this research allowed for the formulation of the following conclusions:

- AQP9 was upregulated in IGT and T2D patients in preliminary proteomics analysis of human liver samples from morbidly obese patients.
- In a HepG2 model of lipid overload, which resembles the lipid overload condition in the liver of obese patients, upregulation of the AQP9 in HepG2 results in toxicity for the cells, showing an extremely high activation of the Caspases 3 and 7.
- The downregulation of AQP9 in HepG2 under lipid overload prevents the accumulation of lipid droplets, and decreases activation of the Caspases 3 and 7, which suggests that AQP9 plays a major role in hepatic lipid accumulation and its harmful cellular effects.
- The lipid overload is limiting the flow of hydrogen peroxide through the membrane of the HepG2 cells, yet it triggers the accumulation of hydrogen peroxide in the endoplasmic reticulum, mirroring the consequences induced by the lipid overload in human hepatocytes.
- Proteomic analysis confirmed, that lipid overload in HepG2 cells induces molecular mechanisms connected with excessive lipid synthesis, accumulation and mitochondrial dysfunction. AQP9 overexpression in HepG2 cells under lipid overload up-regulated proteins involved in mitochondrial  $\beta$ -oxidation, oxidative stress and ER-related unfolded protein response (UPR), whereas AQP9 silencing downregulates hepatic fatty acid importers and glycogen synthase kinase 3 (GSK3B) suggesting beneficial effects on lipid accumulation and insulin sensitivity.
- Newly-developed DIA proteomics approach based on the staggered windows (STW) principle allows for precise analysis of experimental and clinical samples with significantly less time and resources required, as compared to variable window width (VWW) counterpart.

## 9 Bibliography

- [1] World Health Organization, Obesity and overweight, (2020).  
[https://www.who.int/news-room/fact-sheets/detail/obesity-and-overweight#:~:text=In 2016%2C more than 1.9 billion adults aged 18 years,women\) were obese in 2016.](https://www.who.int/news-room/fact-sheets/detail/obesity-and-overweight#:~:text=In 2016%2C more than 1.9 billion adults aged 18 years,women) were obese in 2016.)
- [2] Apovian CM., Obesity: definition, comorbidities, causes, and burden., *Am J Manag Care.* 22 (2016) s176-85.
- [3] C. Lefranc, M. Friederich-Persson, R. Palacios-Ramirez, A.N.D. Cat, Mitochondrial oxidative stress in obesity: Role of the mineralocorticoid receptor, *J. Endocrinol.* 238 (2018) R143–R159.  
[https://doi.org/10.1530/JOE-18-0163.](https://doi.org/10.1530/JOE-18-0163)
- [4] N. Stefan, A.L. Birkenfeld, M.B. Schulze, Global pandemics interconnected — obesity, impaired metabolic health and COVID-19, *Nat. Rev. Endocrinol.* 2021 173. 17 (2021) 135–149.  
[https://doi.org/10.1038/s41574-020-00462-1.](https://doi.org/10.1038/s41574-020-00462-1)
- [5] P. Arner, M. Rydén, Fatty acids, obesity and insulin resistance, *Obes. Facts.* 8 (2015) 147–155. [https://doi.org/10.1159/000381224.](https://doi.org/10.1159/000381224)
- [6] G. Wang, Raison d'être of insulin resistance: the adjustable threshold hypothesis, *J. R. Soc. Interface.* 11 (2014) 20140892.  
[https://doi.org/10.1098/rsif.2014.0892.](https://doi.org/10.1098/rsif.2014.0892)
- [7] C. Robinson, W. V. Tamborlane, D.G. Maggs, S. Enoksson, R.S. Sherwin, D. Silver, G.I. Shulman, S. Caprio, Effect of insulin on glycerol production in obese adolescents, *Am. J. Physiol. - Endocrinol. Metab.* 274 (1998).  
[https://doi.org/10.1152/ajpendo.1998.274.4.e737.](https://doi.org/10.1152/ajpendo.1998.274.4.e737)
- [8] A.U. Blachnio-Zabielska, M. Chacinska, M.H. Vendelbo, P. Zabielski, The Crucial Role of C18-Cer in Fat-Induced Skeletal Muscle Insulin

- Resistance, *Cell. Physiol. Biochem.* 40 (2016) 1207–1220.  
<https://doi.org/10.1159/000453174>.
- [9] P. Zabielski, J. Daniluk, H.R. Hady, A.R. Markowski, M. Imierska, J. Górski, A.U. Blachnio-Zabielska, The effect of high-fat diet and inhibition of ceramide production on insulin action in liver, *J. Cell. Physiol.* 234 (2019) 1851–1861. <https://doi.org/10.1002/jcp.27058>.
- [10] P. Zabielski, H.R. Hady, M. Chacinska, K. Roszczyc, J. Gorski, A.U. Blachnio-Zabielska, The effect of high fat diet and metformin treatment on liver lipids accumulation and their impact on insulin action, *Sci. Rep.* 8 (2018). <https://doi.org/10.1038/s41598-018-25397-6>.
- [11] J. Shi, Y. Zhang, W. Gu, B. Cui, M. Xu, Q. Yan, W. Wang, G. Ning, J. Hong, Serum Liver Fatty Acid Binding Protein Levels Correlate Positively with Obesity and Insulin Resistance in Chinese Young Adults, *PLoS One.* 7 (2012). <https://doi.org/10.1371/journal.pone.0048777>.
- [12] R.M. Fisher, K. Gertow, Fatty acid transport proteins and insulin resistance, *Curr. Opin. Lipidol.* 16 (2005) 173–178.  
<https://doi.org/10.1097/01.mol.0000162322.39548.b1>.
- [13] A.S. Verkman, Aquaporins in Clinical Medicine, *Annu. Rev. Med.* 63 (2012) 303–316. <https://doi.org/10.1146/annurev-med-043010-193843>.
- [14] J.M. Carbrey, D.A. Gorelick-Feldman, D. Kozono, J. Praetorius, S. Nielsen, P. Agre, Aquaglyceroporin AqP9: Solute permeation and metabolic control of expression in liver, *Proc. Natl. Acad. Sci. U. S. A.* 100 (2003) 2945–2950. <https://doi.org/10.1073/pnas.0437994100>.
- [15] A.M. Rojek, M.T. Skowronski, E.M. Füchtbauer, A.C. Füchtbauer, R.A. Fenton, P. Agre, J. Frøkiær, S. Nielsen, Defective glycerol metabolism in aquaporin 9 (AQP9) knockout mice, *Proc. Natl. Acad. Sci. U. S. A.* 104 (2007) 3609–3614. <https://doi.org/10.1073/pnas.0610894104>.

- [16] N. Maeda, T. Hibuse, T. Funahashi, Role of aquaporin-7 and aquaporin-9 in glycerol metabolism; Involvement in obesity, *Handb. Exp. Pharmacol.* 190 (2009) 233–249. [https://doi.org/10.1007/978-3-540-79885-9\\_12](https://doi.org/10.1007/978-3-540-79885-9_12).
- [17] A.T. Matthews, M.K. Ross, Oxylradical Stress, Endocannabinoids, and Atherosclerosis, *Toxics*. 3 (2015) 481–498. <https://doi.org/10.3390/TOXICS3040481>.
- [18] I.G. Ryoo, S.H. Lee, M.K. Kwak, Redox Modulating NRF2: A Potential Mediator of Cancer Stem Cell Resistance, *Oxid. Med. Cell. Longev.* 2016 (2016). <https://doi.org/10.1155/2016/2428153>.
- [19] H. Sies, Hydrogen peroxide as a central redox signaling molecule in physiological oxidative stress: Oxidative eustress, *Redox Biol.* 11 (2017) 613–619. <https://doi.org/10.1016/J.REDOX.2016.12.035>.
- [20] H. Sies, D.P. Jones, Reactive oxygen species (ROS) as pleiotropic physiological signalling agents, *Nat. Rev. Mol. Cell Biol.* 21 (2020) 363–383. <https://doi.org/10.1038/S41580-020-0230-3>.
- [21] Y. Hoshino, H. Sonoda, R. Nishimura, K. Mori, K. Ishibashi, M. Ikeda, Involvement of the NADPH oxidase 2 pathway in renal oxidative stress in *Aqp11*<sup>-/-</sup> mice, *Biochem. Biophys. Reports*. 17 (2019) 169–176. <https://doi.org/10.1016/j.bbrep.2019.01.003>.
- [22] X. Wu, K. Chen, K.J. Williams, An oxide transport chain essential for balanced insulin action, *Atherosclerosis*. 298 (2020) 42–51. <https://doi.org/10.1016/j.atherosclerosis.2020.02.006>.
- [23] M. Bertolotti, S. Bestetti, J.M. García-Manteiga, I. Medraño-Fernandez, A. Dal Mas, M.L. Malosio, R. Sitia, Tyrosine Kinase signal modulation: A matter of H<sub>2</sub>O<sub>2</sub> membrane permeability?, *Antioxidants Redox Signal.* 19 (2013) 1447–1451. <https://doi.org/10.1089/ars.2013.5330>.

- [24] Y. Wang, X. Zhang, H. Yao, X. Chen, L. Shang, P. Li, X. Cui, J. Zeng, Peroxisome-generated succinate induces lipid accumulation and oxidative stress in the kidneys of diabetic mice, *J. Biol. Chem.* 298 (2022) 101660. <https://doi.org/10.1016/J.JBC.2022.101660>.
- [25] M.H. Elbatreek, H. Mucke, H.H.H.W. Schmidt, NOX Inhibitors: From Bench to Naxibs to Bedside, *Handb. Exp. Pharmacol.* 264 (2021) 145–168. [https://doi.org/10.1007/164\\_2020\\_387](https://doi.org/10.1007/164_2020_387).
- [26] H. Sies, Oxidative stress: oxidants and antioxidants, *Exp. Physiol.* 82 (1997) 291–295. <https://doi.org/10.1113/EXPPHYSIOL.1997.SP004024>.
- [27] S. Desaint, S. Luriau, J.C. Aude, G. Rousselet, M.B. Toledano, Mammalian antioxidant defenses are not inducible by H<sub>2</sub>O<sub>2</sub>, *J. Biol. Chem.* 279 (2004) 31157–31163. <https://doi.org/10.1074/JBC.M401888200>.
- [28] M.M. Goyal, A. Basak, Human catalase: looking for complete identity, *Protein Cell.* 1 (2010) 888–897. <https://doi.org/10.1007/S13238-010-0113-Z>.
- [29] L. Miao, D.K. St. Clair, Regulation of superoxide dismutase genes: implications in disease, *Free Radic. Biol. Med.* 47 (2009) 344–356. <https://doi.org/10.1016/J.FREERADBIOMED.2009.05.018>.
- [30] S.G. Rhee, Overview on Peroxiredoxin, *Mol. Cells.* 39 (2016) 1–5. <https://doi.org/10.14348/MOLCELLS.2016.2368>.
- [31] H. Ghareeb, N. Metanis, The Thioredoxin System: A Promising Target for Cancer Drug Development, *Chemistry.* 26 (2020) 10175–10184. <https://doi.org/10.1002/CHEM.201905792>.
- [32] H. Sies, Glutathione and its role in cellular functions, *Free Radic. Biol. Med.* 27 (1999) 916–921. [https://doi.org/10.1016/S0891-5849\(99\)00177-](https://doi.org/10.1016/S0891-5849(99)00177-)

X.

- [33] H.J. Forman, H. Zhang, A. Rinna, Glutathione: overview of its protective roles, measurement, and biosynthesis, *Mol. Aspects Med.* 30 (2009) 1–12. <https://doi.org/10.1016/J.MAM.2008.08.006>.
- [34] J.H. No, Y.-B. Kim, Y.S. Song, Targeting nrf2 signaling to combat chemoresistance, *J. Cancer Prev.* 19 (2014) 111–117. <https://doi.org/10.15430/JCP.2014.19.2.111>.
- [35] J. Patwardhan, P. Bhatt, Flavonoids Derived from *Abelmoschus esculentus* Attenuates UV-B Induced Cell Damage in Human Dermal Fibroblasts Through Nrf2-ARE Pathway, *Pharmacogn. Mag.* 12 (2016) 129. <https://doi.org/10.4103/0973-1296.182175>.
- [36] H.K. Bryan, A. Olayanju, C.E. Goldring, B.K. Park, The Nrf2 cell defence pathway: Keap1-dependent and -independent mechanisms of regulation, *Biochem. Pharmacol.* 85 (2013) 705–717. <https://doi.org/10.1016/J.BCP.2012.11.016>.
- [37] J.D. Hayes, M. McMahon, S. Chowdhry, A.T. Dinkova-Kostova, Cancer chemoprevention mechanisms mediated through the Keap1-Nrf2 pathway, *Antioxid. Redox Signal.* 13 (2010) 1713–1748. <https://doi.org/10.1089/ARS.2010.3221>.
- [38] H.G. Glitsch, Electrophysiology of the sodium-potassium-ATPase in cardiac cells, *Physiol. Rev.* 81 (2001) 1791–1826. <https://doi.org/10.1152/PHYSREV.2001.81.4.1791>.
- [39] S.W. Graves, Sodium regulation, sodium pump function and sodium pump inhibitors in uncomplicated pregnancy and preeclampsia, *Front. Biosci.* 12 (2007) 2438–2446. <https://doi.org/10.2741/2245>.
- [40] X. Chen, R. Cao, W. Zhong, Host Calcium Channels and Pumps in Viral

- Infections, Cells. 9 (2019). <https://doi.org/10.3390/CELLS9010094>.
- [41] M. Brini, T. Cali, D. Ottolini, E. Carafoli, Calcium pumps: why so many?, *Compr. Physiol.* 2 (2012) 1045–1060.  
<https://doi.org/10.1002/CPHY.C110034>.
- [42] W.S. Trimble, S. Grinstein, Barriers to the free diffusion of proteins and lipids in the plasma membrane, *J. Cell Biol.* 208 (2015) 259.  
<https://doi.org/10.1083/JCB.201410071>.
- [43] U.K. Kar, M. Simonian, J.P. Whitelegge, Integral membrane proteins: bottom-up, top-down and structural proteomics, *Expert Rev. Proteomics.* 14 (2017) 715–723. <https://doi.org/10.1080/14789450.2017.1359545>.
- [44] P.D. Bosshart, D. Fotiadis, Secondary Active Transporters, in: *Subcell. Biochem.*, Springer New York, 2019: pp. 275–299.  
[https://doi.org/10.1007/978-3-030-18768-2\\_9](https://doi.org/10.1007/978-3-030-18768-2_9).
- [45] S. Edamana, F.H. Login, S. Yamada, T.H. Kwon, L.N. Nejsum, Aquaporin water channels as regulators of cell-cell adhesion proteins, *Am. J. Physiol. Cell Physiol.* 320 (2021) C771–C777.  
<https://doi.org/10.1152/AJPCELL.00608.2020>.
- [46] K. Murata, K. Mitsuoka, T. Hiral, T. Walz, P. Agre, J.B. Heymann, A. Engel, Y. Fujiyoshi, Structural determinants of water permeation through aquaporin-1, *Nature.* 407 (2000) 599–605.  
<https://doi.org/10.1038/35036519>.
- [47] A.S. Verkman, B. Yang, Y. Song, G.T. Manley, T. Ma, Role of water channels in fluid transport studied by phenotype analysis of aquaporin knockout mice, *Exp. Physiol.* 85 S (2000). <https://doi.org/10.1111/j.1469-445x.2000.tb00028.x>.
- [48] M.H. Beall, J.P.H.M. van den Wijngaard, M.J.C. van Gemert, M.G. Ross,

- Amniotic Fluid Water Dynamics, *Placenta*. 28 (2007) 816–823.  
<https://doi.org/10.1016/j.placenta.2006.11.009>.
- [49] T. Nguyen, J. Toussaint, Y. Xue, C. Raval, L. Cancel, S. Russell, Y. Shou, O. Sedes, Y. Sun, R. Yakobov, J.M. Tarbell, K.M. Jan, D.S. Rumschitzki, Aquaporin-1 facilitates pressure-driven water flow across the aortic endothelium, *Am. J. Physiol. - Hear. Circ. Physiol.* 308 (2015) H1051–H1064. <https://doi.org/10.1152/ajpheart.00499.2014>.
- [50] A. Engel, T. Wszpalz, Y. Fujiyoshi, The AQP structure and functional implications, *Handb. Exp. Pharmacol.* 190 (2009) 31–56.  
[https://doi.org/10.1007/978-3-540-79885-9\\_2](https://doi.org/10.1007/978-3-540-79885-9_2).
- [51] S. Bestetti, M. Galli, I. Sorrentino, P. Pinton, A. Rimessi, R. Sitia, I. Medraño-Fernandez, Human aquaporin-11 guarantees efficient transport of H<sub>2</sub>O<sub>2</sub> across the endoplasmic reticulum membrane, *Redox Biol.* 28 (2020).
- [52] S. Bestetti, I. Medraño-Fernandez, M. Galli, M. Ghitti, G.P. Bienert, G. Musco, A. Orsi, A. Rubartelli, R. Sitia, A persulfidation-based mechanism controls aquaporin-8 conductance, *Sci. Adv.* 4 (2018).  
<https://doi.org/10.1126/sciadv.aar5770>.
- [53] T. Laloux, B. Junqueira, L.C. Maistriaux, J. Ahmed, A. Jurkiewicz, F. Chaumont, Plant and mammal aquaporins: Same but different, *Int. J. Mol. Sci.* 19 (2018). <https://doi.org/10.3390/ijms19020521>.
- [54] H. Nishimura, Y. Yang, Aquaporins in avian kidneys: function and perspectives, *Am J Physiol Regul Integr Comp Physiol.* 305 (2013) 1201–1214. <https://doi.org/10.1152/ajpregu.00177.2013.-For>.
- [55] N. Maeda, T. Funahashi, I. Shimomura, Cardiovascular-metabolic impact of adiponectin and aquaporin, *Endocr. J.* 60 (2013) 251–259.  
<https://doi.org/10.1507/endocrj.EJ13-0016>.

- [56] M. Ikeda, E. Beitz, D. Kozono, W.B. Guggino, P. Agre, M. Yasui, Characterization of aquaporin-6 as a nitrate channel in mammalian cells. Requirement of pore-lining residue threonine 63, *J. Biol. Chem.* 277 (2002) 39873–39879. <https://doi.org/10.1074/jbc.M207008200>.
- [57] U. Laforenza, M.F. Scaffino, G. Gastaldi, Aquaporin-10 Represents an Alternative Pathway for Glycerol Efflux from Human Adipocytes, *PLoS One.* 8 (2013) e54474. <https://doi.org/10.1371/journal.pone.0054474>.
- [58] M. Hara-Chikuma, A.S. Verkman, Aquaporin-3 functions as a glycerol transporter in mammalian skin, *Biol. Cell.* 97 (2005) 479–486. <https://doi.org/10.1042/bc20040104>.
- [59] C. Li, W. Wang, Molecular biology of aquaporins, in: *Adv. Exp. Med. Biol.*, Springer New York LLC, 2017: pp. 1–34. [https://doi.org/10.1007/978-94-024-1057-0\\_1](https://doi.org/10.1007/978-94-024-1057-0_1).
- [60] K. Ishibashi, Y. Tanaka, Y. Morishita, The role of mammalian superaquaporins inside the cell, *Biochim. Biophys. Acta - Gen. Subj.* 1840 (2014) 1507–1512. <https://doi.org/10.1016/j.bbagen.2013.10.039>.
- [61] I. Medraño-Fernandez, R. Sitia, Aquaporins: Gatekeepers in the borders of oxidative stress and redox signaling, Elsevier Inc., 2019. <https://doi.org/10.1016/B978-0-12-818606-0.00011-0>.
- [62] A.B. Chepelinsky, Structural function of mip/aquaporin 0 in the eye lens; Genetic defects lead to congenital inherited cataracts, *Handb. Exp. Pharmacol.* 190 (2009) 265–297. [https://doi.org/10.1007/978-3-540-79885-9\\_14](https://doi.org/10.1007/978-3-540-79885-9_14).
- [63] N. Koyama, K. Ishibashi, M. Kuwahara, N. Inase, M. Ichioka, S. Sasaki, F. Marumo, Cloning and functional expression of human aquaporin8 cDNA and analysis of its gene, *Genomics.* 54 (1998) 169–172. <https://doi.org/10.1006/geno.1998.5552>.

- [64] M. Bertolotti, G. Farinelli, M. Galli, A. Aiuti, R. Sitia, AQP8 transports NOX2-generated H<sub>2</sub>O<sub>2</sub> across the plasma membrane to promote signaling in B cells, *J. Leukoc. Biol.* 100 (2016).  
<https://doi.org/10.1189/jlb.2AB0116-045R>.
- [65] I. Medraño-Fernandez, S. Bestetti, M. Bertolotti, G.P. Bienert, C. Bottino, U. Laforenza, A. Rubartelli, R. Sitia, Stress Regulates Aquaporin-8 Permeability to Impact Cell Growth and Survival, *Antioxidants Redox Signal.* 24 (2016) 1031–1044. <https://doi.org/10.1089/ars.2016.6636>.
- [66] X. Huang, G. Liu, J. Guo, Z.Q. Su, The PI3K/AKT pathway in obesity and type 2 diabetes, *Int. J. Biol. Sci.* 14 (2018) 1483.  
<https://doi.org/10.7150/IJBS.27173>.
- [67] M. Hara-Chikuma, M. Tanaka, A.S. Verkman, M. Yasui, Inhibition of aquaporin-3 in macrophages by a monoclonal antibody as potential therapy for liver injury, *Nat. Commun.* 11 (2020) 1–14.  
<https://doi.org/10.1038/s41467-020-19491-5>.
- [68] K. Kishida, H. Kuriyama, T. Funahashi, I. Shimomura, S. Kihara, N. Ouchi, M. Nishida, H. Nishizawa, M. Matsuda, M. Takahashi, K. Hotta, T. Nakamura, S. Yamashita, Y. Tochino, Y. Matsuzawa, Aquaporin adipose, a putative glycerol channel in adipocytes, *J. Biol. Chem.* 275 (2000) 20896–20902. <https://doi.org/10.1074/jbc.M001119200>.
- [69] A. Rodríguez, V. Catalán, J. Gómez-Ambrosi, G. Frühbeck, Aquaglyceroporins serve as metabolic gateways in adiposity and insulin resistance control, *Cell Cycle.* 10 (2011) 1548–1556.  
<https://doi.org/10.4161/cc.10.10.15672>.
- [70] Z. R, Z. R, E. TO, K. SD, H. G, L. A, M. F, FAT SIGNALS--lipases and lipolysis in lipid metabolism and signaling, *Cell Metab.* 15 (2012) 279–291. <https://doi.org/10.1016/J.CMET.2011.12.018>.

- [71] H. L, G. PJ, The regulation of hepatic fatty acid synthesis and partitioning: the effect of nutritional state, *Nat. Rev. Endocrinol.* 15 (2019) 689–700. <https://doi.org/10.1038/S41574-019-0256-9>.
- [72] A. Rodríguez, V. Catalán, J. Gómez-Ambrosi, S. García-Navarro, F. Rotellar, V. Valentí, C. Silva, M.J. Gil, J. Salvador, M.A. Burrell, G. Calamita, M.M. Malagón, G. Frühbeck, Insulin- and Leptin-Mediated Control of Aquaglyceroporins in Human Adipocytes and Hepatocytes Is Mediated via the PI3K/Akt/mTOR Signaling Cascade, *J. Clin. Endocrinol. Metab.* 96 (2011) E586–E597. <https://doi.org/10.1210/jc.2010-1408>.
- [73] J. Lebeck, Metabolic impact of the glycerol channels AQP7 and AQP9 in adipose tissue and liver, *J. Mol. Endocrinol.* 52 (2014) R165–R178. <https://doi.org/10.1530/JME-13-0268>.
- [74] F. Iena, J. Lebeck, Implications of Aquaglyceroporin 7 in Energy Metabolism, *Int. J. Mol. Sci.* 19 (2018) 154. <https://doi.org/10.3390/ijms19010154>.
- [75] U. Ozcan, Q. Cao, E. Yilmaz, A.-H. Lee, N.N. Iwakoshi, E. Ozdelen, G. Tuncman, C. Gorgun, L.H. Glimcher, G.S. Hotamisligil, Endoplasmic Reticulum Stress Links Obesity, Insulin Action, and Type 2 Diabetes, *Science* (80-. ). 1 (2012) 11–25.
- [76] N. Kawasaki, R. Asada, A. Saito, S. Kanemoto, K. Imaizumi, Obesity-induced endoplasmic reticulum stress causes chronic inflammation in adipose tissue, *Sci. Reports* 2012 21. 2 (2012) 1–7. <https://doi.org/10.1038/srep00799>.
- [77] S. Ezquerro, S. Becerril, C. Tuero, L. Méndez-Giménez, F. Mocha, R. Moncada, V. Valentí, J.A. Cienfuegos, V. Catalán, J. Gómez-Ambrosi, K. Piper Hanley, G. Frühbeck, A. Rodríguez, Role of ghrelin isoforms in the mitigation of hepatic inflammation, mitochondrial dysfunction, and

- endoplasmic reticulum stress after bariatric surgery in rats, *Int. J. Obes.* 44 (2020) 475–487. <https://doi.org/10.1038/s41366-019-0420-2>.
- [78] G. Frühbeck, I. Balaguer, L. Méndez-Giménez, V. Valentí, S. Becerril, V. Catalán, J. Gómez-Ambrosi, C. Silva, J. Salvador, G. Calamita, M.M. Malagón, A. Rodríguez, Aquaporin-11 Contributes to TGF- $\beta$ 1-Induced Endoplasmic Reticulum Stress in Human Visceral Adipocytes: Role in Obesity-Associated Inflammation, *Cells*. 9 (2020). <https://doi.org/10.3390/cells9061403>.
- [79] M. Galli, A. Hameed, A. Żbikowski, P. Zabielski, Aquaporins in insulin resistance and diabetes: More than channels!, *Redox Biol.* 44 (2021) 102027. <https://doi.org/10.1016/J.REDOX.2021.102027>.
- [80] S.B. Breitkopf, S.J.H. Ricoult, M. Yuan, Y. Xu, D.A. Peake, B.D. Manning, J.M. Asara, A relative quantitative positive/negative ion switching method for untargeted lipidomics via high resolution LC-MS/MS from any biological source, *Metabolomics*. 13 (2017). <https://doi.org/10.1007/S11306-016-1157-8>.
- [81] M. Ghaste, R. Mistrik, V. Shulaev, Applications of Fourier Transform Ion Cyclotron Resonance (FT-ICR) and Orbitrap Based High Resolution Mass Spectrometry in Metabolomics and Lipidomics, *Int. J. Mol. Sci.* 17 (2016). <https://doi.org/10.3390/IJMS17060816>.
- [82] C. Ludwig, L. Gillet, G. Rosenberger, S. Amon, B.C. Collins, R. Aebersold, Data-independent acquisition-based SWATH - MS for quantitative proteomics: a tutorial , *Mol. Syst. Biol.* 14 (2018) 1–23. <https://doi.org/10.15252/msb.20178126>.
- [83] R. Bruderer, O.M. Bernhardt, T. Gandhi, Y. Xuan, J. Sonderrmann, M. Schmidt, D. Gomez-Varela, L. Reiter, Optimization of experimental parameters in data-independent mass spectrometry significantly increases

- depth and reproducibility of results, *Mol. Cell. Proteomics*. 16 (2017) 2296–2309. <https://doi.org/10.1074/mcp.RA117.000314>.
- [84] S. Gessulat, T. Schmidt, D.P. Zolg, P. Samaras, K. Schnatbaum, J. Zerweck, T. Knaute, J. Rechenberger, B. Delanghe, A. Huhmer, U. Reimer, H.C. Ehrlich, S. Aiche, B. Kuster, M. Wilhelm, Prosit: proteome-wide prediction of peptide tandem mass spectra by deep learning, *Nat. Methods*. 16 (2019) 509–518. <https://doi.org/10.1038/S41592-019-0426-7>.
- [85] C.C. Tsou, D. Avtonomov, B. Larsen, M. Tucholska, H. Choi, A.C. Gingras, A.I. Nesvizhskii, DIA-Umpire: comprehensive computational framework for data-independent acquisition proteomics, *Nat. Methods*. 12 (2015) 258–264. <https://doi.org/10.1038/NMETH.3255>.
- [86] J.D. Egertson, A. Kuehn, G.E. Merrihew, N.W. Bateman, B.X. MacLean, Y.S. Ting, J.D. Canterbury, D.M. Marsh, M. Kellmann, V. Zabrouskov, C.C. Wu, M.J. MacCoss, Multiplexed MS/MS for Improved Data Independent Acquisition, *Nat. Methods*. 10 (2013) 744. <https://doi.org/10.1038/NMETH.2528>.
- [87] C. Zhou, B.L. Schulz, Glycopeptide variable window SWATH for improved data independent acquisition glycoprotein analysis, *Anal. Biochem*. 597 (2020) 113667. <https://doi.org/10.1016/J.AB.2020.113667>.
- [88] Y. Zhang, A. Bilbao, T. Bruderer, J. Luban, C. Strambio-De-Castillia, F. Lisacek, G. Hopfgartner, E. Varesio, The Use of Variable Q1 Isolation Windows Improves Selectivity in LC-SWATH-MS Acquisition, *J. Proteome Res*. 14 (2015) 4359–4371. <https://doi.org/10.1021/acs.jproteome.5b00543>.
- [89] D. Amodei, J. Egertson, B.X. MacLean, R. Johnson, G.E. Merrihew, A. Keller, D. Marsh, O. Vitek, P. Mallick, M.J. MacCoss, Improving Precursor Selectivity in Data-Independent Acquisition Using Overlapping

- Windows, J. *Am. Soc. Mass Spectrom.* 30 (2019) 669–684.  
<https://doi.org/10.1007/s13361-018-2122-8>.
- [90] L.K. Pino, B.C. Searle, H.Y. Yang, A.N. Hoofnagle, W.S. Noble, M.J. MacCoss, Matrix-Matched Calibration Curves for Assessing Analytical Figures of Merit in Quantitative Proteomics, *J. Proteome Res.* 19 (2020) 1147–1153. <https://doi.org/10.1021/acs.jproteome.9b00666>.
- [91] B.C. Searle, L.K. Pino, J.D. Egertson, Y.S. Ting, R.T. Lawrence, B.X. MacLean, J. Villén, M.J. MacCoss, Chromatogram libraries improve peptide detection and quantification by data independent acquisition mass spectrometry, *Nat. Commun.* 9 (2018). <https://doi.org/10.1038/s41467-018-07454-w>.
- [92] C.C. Christianson, C.J.L. Johnson, S.R. Needham, The advantages of microflow LC-MS/MS compared with conventional HPLC-MS/MS for the analysis of methotrexate from human plasma, *Bioanalysis.* 5 (2013) 1387–1396. <https://doi.org/10.4155/BIO.13.73>.
- [93] A.J. Kleinnijenhuis, M. Ingola, J.H. Toersche, F.L. Van Holthoon, W.D. Van Dongen, Quantitative bottom up analysis of infliximab in serum using protein A purification and integrated  $\mu$ LC-electrospray chip IonKey MS/MS technology, *Bioanalysis.* 8 (2016) 891–904.  
<https://doi.org/10.4155/BIO-2015-0015>.
- [94] OptiFlow Turbo V, (n.d.). <https://sciex.com/products/ion-sources/optiflow-turbo-v> (accessed December 28, 2021).
- [95] Nexera Mikros | Shimadzu Scientific Instruments, (n.d.).  
<https://www.ssi.shimadzu.com/products/liquid-chromatography-mass-spectrometry/nexera-mikros.html> (accessed December 28, 2021).
- [96] J. Zhang, W. Shou, T. Ogura, S. Li, H. Weller, Optimization of microflow LC-MS/MS and its utility in quantitative discovery bioanalysis,

- Bioanalysis. 11 (2019) 1117–1127. <https://doi.org/10.4155/bio-2019-0076>.
- [97] P.E. Geyer, E. Voytik, P. V Treit, S. Doll, A. Kleinhempel, L. Niu, J.B. Müller, M. Buchholtz, J.M. Bader, D. Teupser, L.M. Holdt, M. Mann, Plasma Proteome Profiling to detect and avoid sample-related biases in biomarker studies, *EMBO Mol. Med.* 11 (2019).  
<https://doi.org/10.15252/EMMM.201910427>.
- [98] R. Bruderer, J. Muntel, S. Müller, O.M. Bernhardt, T. Gandhi, O. Cominetti, C. Macron, J. Carayol, O. Rinner, A. Astrup, W.H.M. Saris, J. Hager, A. Valsesia, L. Dayon, L. Reiter, Analysis of 1508 Plasma Samples by Capillary-Flow Data-Independent Acquisition Profiles Proteomics of Weight Loss and Maintenance, *Mol. Cell. Proteomics.* 18 (2019) 1242.  
<https://doi.org/10.1074/MCP.RA118.001288>.
- [99] F. Coscia, S. Doll, J.M. Bech, L. Schweizer, A. Mund, E. Lengyel, J. Lindebjerg, G.I. Madsen, J.M.A. Moreira, M. Mann, A streamlined mass spectrometry–based proteomics workflow for large-scale FFPE tissue analysis, *J. Pathol.* 251 (2020) 100–112.  
<https://doi.org/10.1002/PATH.5420>.
- [100] M. Xu, J. Deng, K. Xu, T. Zhu, L. Han, Y. Yan, D. Yao, H. Deng, D. Wang, Y. Sun, C. Chang, X. Zhang, J. Dai, L. Yue, Q. Zhang, X. Cai, Y. Zhu, H. Duan, Y. Liu, D. Li, Y. Zhu, T.R.D.J. Radstake, D.M.W. Balak, D. Xu, T. Guo, C. Lu, X. Yu, In-depth serum proteomics reveals biomarkers of psoriasis severity and response to traditional Chinese medicine, *Theranostics.* 9 (2019) 2475.  
<https://doi.org/10.7150/THNO.31144>.
- [101] Y. Zhu, T. Weiss, Q. Zhang, R. Sun, B. Wang, X. Yi, Z. Wu, H. Gao, X. Cai, G. Ruan, T. Zhu, C. Xu, S. Lou, X. Yu, L. Gillet, P. Blattmann, K. Saba, C.D. Fankhauser, M.B. Schmid, D. Rutishauser, J. Ljubicic, A.

- Christiansen, C. Fritz, N.J. Rupp, C. Poyet, E. Rushing, M. Weller, P. Roth, E. Haralambieva, S. Hofer, C. Chen, W. Jochum, X. Gao, X. Teng, L. Chen, Q. Zhong, P.J. Wild, R. Aebersold, T. Guo, High-throughput proteomic analysis of FFPE tissue samples facilitates tumor stratification, *Mol. Oncol.* 13 (2019) 2305. <https://doi.org/10.1002/1878-0261.12570>.
- [102] I.R. Leon, V. Schwammle, O.N. Jensen, R.R. Sprenger, Quantitative assessment of in-solution digestion efficiency identifies optimal protocols for unbiased protein analysis, *Mol. Cell. Proteomics.* 12 (2013) 2992–3005. <https://doi.org/10.1074/mcp.M112.025585>.
- [103] M. Hernandez-Valladares, E. Aasebø, O. Mjaavatten, M. Vaudel, Ø. Bruserud, F. Berven, F. Selheim, Reliable FASP-based procedures for optimal quantitative proteomic and phosphoproteomic analysis on samples from acute myeloid leukemia patients, *Biol. Proced. Online.* 18 (2016) 1–10. <https://doi.org/10.1186/S12575-016-0043-0/TABLES/1>.
- [104] J. Rappsilber, M. Mann, Y. Ishihama, Protocol for micro-purification, enrichment, pre-fractionation and storage of peptides for proteomics using StageTips, *Nat. Protoc.* 2007 28. 2 (2007) 1896–1906. <https://doi.org/10.1038/nprot.2007.261>.
- [105] N.A. Kulak, G. Pichler, I. Paron, N. Nagaraj, M. Mann, Minimal, encapsulated proteomic-sample processing applied to copy-number estimation in eukaryotic cells, *Nat. Methods* 2014 113. 11 (2014) 319–324. <https://doi.org/10.1038/nmeth.2834>.
- [106] B. Schilling, B.W. Gibson, C.L. Hunter, Generation of high-quality SWATH® acquisition data for label-free quantitative proteomics studies using tripleTOF® mass spectrometers, *Methods Mol. Biol.* 1550 (2017) 223–233. [https://doi.org/10.1007/978-1-4939-6747-6\\_16](https://doi.org/10.1007/978-1-4939-6747-6_16).
- [107] C. Lee, C.H. Huang, LASAGNA-Search: an integrated web tool for

- transcription factor binding site search and visualization, *Biotechniques*. 54 (2013) 141–153. <https://doi.org/10.2144/000113999>.
- [108] C. Lee, C.H. Huang, LASAGNA-Search 2.0: integrated transcription factor binding site search and visualization in a browser, *Bioinformatics*. 30 (2014) 1923–1925. <https://doi.org/10.1093/BIOINFORMATICS/BTU115>.
- [109] T. Hulsen, BioVenn – an R and Python package for the comparison and visualization of biological lists using area-proportional Venn diagrams, *Data Sci.* 4 (2021) 51–61. <https://doi.org/10.3233/DS-210032>.
- [110] S.R. and M.L. Kevin Blighe, EnhancedVolcano: Publication-ready volcano plots with enhanced colouring and labeling., (2019). <https://github.com/kevinblighe/EnhancedVolcano>.
- [111] B. Plevoda, F. Sherman, N-terminal Acetyltransferases and Sequence Requirements for N-terminal Acetylation of Eukaryotic Proteins, *J. Mol. Biol.* 325 (2003) 595–622. [https://doi.org/10.1016/S0022-2836\(02\)01269-X](https://doi.org/10.1016/S0022-2836(02)01269-X).
- [112] L.C. Gillet, P. Navarro, S. Tate, H. Röst, N. Selevsek, L. Reiter, R. Bonner, R. Aebersold, Targeted data extraction of the MS/MS spectra generated by data-independent acquisition: A new concept for consistent and accurate proteome analysis, *Mol. Cell. Proteomics*. 11 (2012) 1–17. <https://doi.org/10.1074/mcp.O111.016717>.
- [113] J.M. Kwiatek, G.S. Han, G.M. Carman, Phosphatidate-mediated regulation of lipid synthesis at the nuclear/endoplasmic reticulum membrane, *Biochim. Biophys. Acta. Mol. Cell Biol. Lipids*. 1865 (2020). <https://doi.org/10.1016/J.BBALIP.2019.03.006>.
- [114] J. Lu, A. Holmgren, The thioredoxin antioxidant system, *Free Radic. Biol. Med.* 66 (2014) 75–87.

<https://doi.org/10.1016/J.FREERADBIOMED.2013.07.036>.

- [115] J.K. Kim, H.D. Jang, Nrf2-mediated HO-1 induction coupled with the ERK signaling pathway contributes to indirect antioxidant capacity of caffeic acid phenethyl ester in HepG2 cells, *Int. J. Mol. Sci.* 15 (2014) 12149–12165. <https://doi.org/10.3390/ijms150712149>.
- [116] O. U, C. Q, Y. E, L. AH, I. NN, O. E, T. G, G. C, G. LH, H. GS, Endoplasmic reticulum stress links obesity, insulin action, and type 2 diabetes, *Science*. 306 (2004) 457–461. <https://doi.org/10.1126/SCIENCE.1103160>.
- [117] M.T. Kassouf, J.R. Hughes, S. Taylor, S.J. McGowan, S. Soneji, A.L. Green, P. Vyas, C. Porcher, Genome-wide identification of TAL1's functional targets: Insights into its mechanisms of action in primary erythroid cells, *Genome Res.* 20 (2010) 1064. <https://doi.org/10.1101/GR.104935.110>.
- [118] E. Butturini, A.C. de Prati, S. Mariotto, Redox Regulation of STAT1 and STAT3 Signaling, *Int. J. Mol. Sci.* 21 (2020) 1–18. <https://doi.org/10.3390/IJMS21197034>.
- [119] M. Grohmann, F. Wiede, G.T. Dodd, E.N. Gurzov, G.J. Ooi, T. Butt, A.A. Rasmiena, S. Kaur, T. Gulati, P.K. Goh, A.E. Treloar, S. Archer, W.A. Brown, M. Muller, M.J. Watt, O. Ohara, C.A. McLean, T. Tiganis, Obesity Drives STAT-1-Dependent NASH and STAT-3-Dependent HCC, *Cell*. 175 (2018) 1289-1306.e20. <https://doi.org/10.1016/J.CELL.2018.09.053>.
- [120] M.R. Chikka, D.D. McCabe, H.M. Tyra, D.T. Rutkowski, C/EBP homologous protein (CHOP) contributes to suppression of metabolic genes during endoplasmic reticulum stress in the liver, *J. Biol. Chem.* 288 (2013) 4405–4415. <https://doi.org/10.1074/JBC.M112.432344>.

- [121] J.E. Lambert, M.A. Ramos-Roman, J.D. Browning, E.J. Parks, Increased de novo Lipogenesis is a Distinct Characteristic of Individuals with Nonalcoholic Fatty Liver Disease, *Gastroenterology*. 146 (2014) 726. <https://doi.org/10.1053/J.GASTRO.2013.11.049>.
- [122] K. van Eunen, S.M.J. Simons, A. Gerding, A. Bleeker, G. den Besten, C.M.L. Touw, S.M. Houten, B.K. Groen, K. Krab, D.J. Reijngoud, B.M. Bakker, Biochemical Competition Makes Fatty-Acid  $\beta$ -Oxidation Vulnerable to Substrate Overload, *PLoS Comput. Biol.* 9 (2013). <https://doi.org/10.1371/journal.pcbi.1003186>.
- [123] T.R. Koves, J.R. Ussher, R.C. Noland, D. Slentz, M. Mosedale, O. Ilkayeva, J. Bain, R. Stevens, J.R.B. Dyck, C.B. Newgard, G.D. Lopaschuk, D.M. Muoio, Mitochondrial Overload and Incomplete Fatty Acid Oxidation Contribute to Skeletal Muscle Insulin Resistance, *Cell Metab.* 7 (2008) 45–56. <https://doi.org/10.1016/J.CMET.2007.10.013>.
- [124] B. Bjørndal, E.K. Alterås, C. Lindquist, A. Svardal, J. Skorve, R.K. Berge, Associations between fatty acid oxidation, hepatic mitochondrial function, and plasma acylcarnitine levels in mice, *Nutr. Metab. (Lond)*. 15 (2018). <https://doi.org/10.1186/S12986-018-0241-7>.
- [125] M.J. Gómez-Lechón, M.T. Donato, A. Martínez-Romero, N. Jiménez, J.V. Castell, J.E. O'Connor, A human hepatocellular in vitro model to investigate steatosis, *Chem. Biol. Interact.* 165 (2007) 106–116. <https://doi.org/10.1016/j.cbi.2006.11.004>.
- [126] A. Mehlem, C.E. Hagberg, L. Muhl, U. Eriksson, A. Falkevall, Imaging of neutral lipids by oil red O for analyzing the metabolic status in health and disease, *Nat. Protoc.* 8 (2013) 1149–1154. <https://doi.org/10.1038/nprot.2013.055>.
- [127] B. Qiu, M. Simon, BODIPY 493/503 Staining of Neutral Lipid Droplets

- for Microscopy and Quantification by Flow Cytometry, *Bio-Protocol*. 6 (2016) 1–6. <https://doi.org/10.21769/bioprotoc.1912>.
- [128] A. V. Matveyenko, D. Liuwantara, T. Gurlo, D. Kirakossian, C. Dalla Man, C. Cobelli, M.F. White, K.D. Copps, E. Volpi, S. Fujita, P.C. Butler, Pulsatile portal vein insulin delivery enhances hepatic insulin action and signaling, *Diabetes*. 61 (2012) 2269–2279. <https://doi.org/10.2337/db11-1462>.
- [129] N. Pørksen, T. Grøfte, J. Greisen, A. Mengel, C. Juhl, J.D. Veldhuis, O. Schmitz, M. Rössle, H. Vilstrup, Human insulin release processes measured by intraportal sampling, *Am. J. Physiol. - Endocrinol. Metab.* 282 (2002). <https://doi.org/10.1152/ajpendo.00516.2000>.
- [130] S. Fu, L. Yang, P. Li, O. Hofmann, L. Dicker, W. Hide, X. Lin, S.M. Watkins, A.R. Ivanov, G.S. Hotamisligil, Aberrant lipid metabolism disrupts calcium homeostasis causing liver endoplasmic reticulum stress in obesity, *Nature*. 473 (2011) 528–531. <https://doi.org/10.1038/nature09968>.
- [131] M. Malinouski, Y. Zhou, V. V. Belousov, D.L. Hatfield, V.N. Gladyshev, Hydrogen peroxide probes directed to different cellular compartments, *PLoS One*. 6 (2011). <https://doi.org/10.1371/journal.pone.0014564>.
- [132] M. Galli, A. Hameed, A. Żbikowski, P. Zabielski, Aquaporins in insulin resistance and diabetes: More than channels!, *Redox Biol.* 44 (2021). <https://doi.org/10.1016/j.redox.2021.102027>.

## 10 Abstract

Obesity is a growing problem in modern society, increasing steadily between adults and children. Adipose tissue accumulation increases the release of free fatty acids and free glycerol in plasma, promoting the accumulation of bioactive lipids in the liver and skeletal muscles. Here, the lipid droplets accumulation correlates with the development of insulin resistance and type 2 diabetes. AQPs are molecules dedicated to the flow of water and small uncharged compounds. AQP9 is a glycerol and H<sub>2</sub>O<sub>2</sub> transporter expressed in the liver. From a preliminary proteomic analysis on human liver samples from obese ND, IGT or T2D patients we confirmed the increase of the proteins connected with lipid droplets accumulation as FABP4 and FABP5. We also saw upregulation of the proteins involved in the antioxidant response, a symptom of oxidative stress present in the liver of IGT and T2D patients. Interestingly, we noticed the upregulation of AQP9 in IGT and T2D. Thus, we developed a lipid overload model to study AQPs' role in this process. We showed that the silencing of AQP9 prevents the accumulation of lipid droplets in HepG2 cells, confirming its potential key role in preventing lipid overload. On the other side, the silencing of AQP11 is not significantly influencing the lipid droplets accumulation. We showed that the overexpression of AQP9 is inducing apoptosis in the cells under lipid overload, showing the toxic effect connected to the deregulation of AQP9 expression in HepG2 cells. The lipid overload limits the ability of the cells to transport hydrogen peroxide through aquaporins. Furthermore, the same lipid overload induces the accumulation of hydrogen peroxide in the ER, a symptom of early oxidative stress. We find also hints of the presence of a reductive shield around the ER of HepG2 cells, causing the reduction of HyPer in the region surrounding the ER. We developed two different approaches for the untargeted DIA analysis of experimental and clinical samples. The first one is based on the creation of an HpH-DDA ion library and VWW-DIA runs, a precise but time- and resource-consuming technique. The second one relies mainly on bioinformatics, with a GPF-Hybrid ion library and 40STW DIA runs. We are obtaining similar results with both techniques, but GPF-Hybrid + 40STW is more effective from the point of view of time and resources. The DIA analysis performed on HepG2 cells modulating AQP9 confirmed the essential role of AQP9 in the lipid overload, proposing it as a possible molecular target to prevent lipid-induced insulin resistance in the liver. In conclusion, we reached multiple aims in this study. On one side we elucidated the impact of AQP9 on the lipid overload and oxidative stress homeostasis in HepG2 cells. On the other

side, we developed a novel LC/MS proteomic approach for the analysis of experimental and clinical samples in the aspect of hepatic lipid overload.

## 11 Abstract in Polish

Obecnie otyłość staje się narastającym problemem zdrowotnym, który dotyka zarówno dorosłych, jak i dzieci. Zwiększona objętość tkanki tłuszczowej prowadzi do nasilonego wyrzutu wolnych kwasów tłuszczowych oraz glicerolu do osocza, co z kolei skutkuje akumulacją aktywnych biologicznie lipidów w wątrobie oraz mięśniach szkieletowych. Nagromadzone w tkankach krople tłuszczu korelują z rozwojem insulinooporności oraz cukrzycy typu drugiego. Akwaporyny (AQP) są białkami o charakterze transporterów cząsteczek wody oraz innych małych, obojętnych związków. Pośród nich na uwagę zasługuje obecna w wątrobie AQP9, która jest transporterem nadtlenku wodoru oraz glicerolu. Wstępne badania proteomiczne tkanki wątrobowej pobranej od otyłych donorów bez cukrzycy, z nietolerancją glukozy (IGT) oraz z cukrzycą typu drugiego (T2D) wykazały zwiększoną ekspresję białek powiązanych z akumulacją kropli tłuszczu m. in. FABP4 i FABP5. Ponadto zaobserwowano nadekspresję białek zaangażowanych w odpowiedź antyoksydacyjną, co wskazuje na obecność zwiększonego stresu oksydacyjnego w tkankach donorów z IGT oraz T2D. Dodatkowo, u pacjentów z IGT oraz T2D wykryto zwiększoną ekspresję AQP9, co może sugerować istotną rolę tego białka w patogenezie T2D. Aby zbadać rolę modulacji ekspresji AQP9 w akumulacji lipidów wątrobowych, opracowano model badawczy z wykorzystaniem stymulowanych kwasami tłuszczowymi, glicerolem i insuliną komórek wątrobowych linii HepG2. Wspomniany powyżej model wykazał, iż wyciszenie AQP9 zapobiega akumulacji kropli tłuszczu w komórkach HepG2, co podkreśla kluczową rolę tego białka w tym procesie. Z drugiej strony, nie wykazaliśmy wpływu AQP11 na wewnątrzkomórkową akumulację kropli tłuszczu. Ponadto, nadekspresja AQP9 prowadziła do apoptozy komórek spowodowanej zwiększoną akumulacją lipidów. Nagromadzenie lipidów ogranicza zdolność komórki do transportu nadtlenku wodoru poprzez kanały akwaporynowe oraz prowadzi do nagromadzenia się tego związku w siateczce śródplazmatycznej (ER) i rozwoju stresu oksydacyjnego. Co więcej, poprzez obserwację redukcji HyPer zlokalizowanego w ER, wykazano obecność mechanizmów redukcyjnych. W celu analiz próbek eksperymentalnych oraz klinicznych stworzono dwie strategie niecelowanych analiz DIA. Pierwsza bazuje na bibliotece jonowej stworzonej w oparciu o frakcjonowanie peptydów w środowisku zasadowym (high pH fractionation; HpH-DDA) oraz analizie próbek badanych z wykorzystaniem zmiennej szerokości okien akwizycji (variable window width; VWW-DIA). Metoda ta będąca obecnie złotym standardem w oznaczeniach DIA, jest czaso- i pracochłonna długotrwały proces opracowania biblioteki jonowej. Drugie

podejście opiera się głównie na analizie bioinformatycznej, z wykorzystaniem biblioteki jonowej opartej o frakcjonowanie w fazie gazowej (gas-phase fractionation; GPF-Hybrid) oraz analizie próbek z wykorzystaniem nakładających się okien akwizycji (staggered windows; STW DIA). Obie strategie pozwalają uzyskać zbliżone wyniki, jednakże to GPF-Hybrid + 40STW jest bardziej efektywna z punktu widzenia wymaganych zasobów. Analizy DIA przeprowadzone na komórkach HepG2 z zmienioną ekspresją AQP9 potwierdziły zasadniczą rolę tego białka w akumulacji lipidów, sugerując, iż AQP9 może zostać wykorzystana jako potencjalny cel molekularny zabiegający rozwojowi indukowanej lipidami insulinooporności w wątrobie. Podsumowując, w niniejszym badaniu zrealizowano kilka celów. Po pierwsze, określono wpływ AQP9 na akumulację lipidów oraz homeostazę stresu oksydacyjnego w komórkach HepG2. Po drugie opracowano nowatorskie podejście proteomiczne LC/MS do analizy próbek eksperymentalnych oraz klinicznych w aspekcie przeciążonych lipidami hepatocytów.

## 12 Supplementary materials

Tables containing the significant proteins from the untargeted proteomics experiment with an average Log<sub>2</sub> ratio smaller of -0.58 or bigger of 0.58.

### LO + I VS Ctrl

ID	Symbol	Expr Log Ratio	Expr p-value
Q5EBL8	PDZD11	2.9840	0.0368
Q99541	PLIN2	2.3396	0.0000
Q9NQE9	HINT3	1.9822	0.0199
Q96PU4	UHRF2	1.6676	0.0131
P15121	AKR1B1	1.4931	0.0336
P46952	HAAO	1.4481	0.0102
Q9BRT6	LLPH	1.3850	0.0031
Q09472	EP300	1.3514	0.0159
Q8N6H7	ARFGAP2	1.2146	0.0005
Q96AD5	PNPLA2	1.1366	0.0104
P52292	KPNA2	1.0934	0.0032
Q9P2X0	DPM3	1.0919	0.0125
Q8IUF8	RIOX2	1.0221	0.0428
P17706	PTPN2	0.8787	0.0066
H3-3B	H3-3A/H3-3B	0.8713	0.0279
Q8WXI9	GATAD2B	0.8540	0.0169
P54646	PRKAA2	0.8200	0.0008
P11388	TOP2A	0.7942	0.0057
Q9NVH0	EXD2	0.7930	0.0007
Q13795	ARFRP1	0.7912	0.0131
O15228	GNPAT	0.7825	0.0020
O43715	TRIAP1	0.7635	0.0109
O94766	B3GAT3	0.6999	0.0058
Q96C86	DCPS	0.6523	0.0397
Q96DX5	ASB9	0.6374	0.0298
Q9UII2	ATP5IF1	0.6346	0.0001
O75179	ANKRD17	0.6237	0.0443
Q12846	STX4	0.6125	0.0419
P36969	GPX4	0.5991	0.0468
Q96MR9	ZNF560	0.5889	0.0014
Q96SB4	SRPK1	-0.5825	0.0389
Q96HQ2	CDKN2AIPNL	-0.5835	0.0027
Q5T2E6	ARMH3	-0.5835	0.0283
Q5QJE6	DNTTIP2	-0.5869	0.0016
Q9GZZ1	NAA50	-0.5890	0.0063
P53367	ARFIP1	-0.5891	0.0032
O95342	ABCB11	-0.5935	0.0022
Q9H9T3	ELP3	-0.5952	0.0480
Q53EL6	PDCD4	-0.5956	0.0120
Q9Y2R5	MRPS17	-0.5957	0.0060
Q9UK58	CCNL1	-0.5993	0.0209
Q9BW60	ELOVL1	-0.5998	0.0395
Q9NUQ3	TXLNG	-0.5999	0.0025
Q13190	STX5	-0.6050	0.0128
Q9UHA3	RSL24D1	-0.6053	0.0095
Q93096	PTP4A1	-0.6105	0.0239

Q9P0J0	NDUFA13	-0.6135	0.0074
P23786	CPT2	-0.6136	0.0257
Q5H9R7	PPP6R3	-0.6181	0.0252
O75934	BCAS2	-0.6280	0.0416
Q15397	PUM3	-0.6334	0.0172
Q9UHA4	LAMTOR3	-0.6360	0.0040
P01111	NRAS	-0.6362	0.0022
Q13286	CLN3	-0.6373	0.0482
Q9BYJ9	YTHDF1	-0.6376	0.0007
P56378	ATP5MJ	-0.6382	0.0014
P62253	UBE2G1	-0.6408	0.0111
P35218	CA5A	-0.6435	0.0212
P53041	PPP5C	-0.6451	0.0194
Q13523	PRPF4B	-0.6471	0.0444
Q7Z478	DHX29	-0.6519	0.0278
Q9UGH3	SLC23A2	-0.6566	0.0001
Q99624	SLC38A3	-0.6611	0.0103
P40616	ARL1	-0.6656	0.0000
O14639	ABLIM1	-0.6704	0.0020
Q9H3P2	NELFA	-0.6734	0.0297
P05154	SERPINA5	-0.6747	0.0000
Q96MU7	YTHDC1	-0.6826	0.0444
Q8N6L1	KRTCAP2	-0.6862	0.0046
Q9Y4A5	TRRAP	-0.6967	0.0046
Q5SNT2	TMEM201	-0.6989	0.0369
O14763	TNFRSF10B	-0.7015	0.0082
Q9H9E3	COG4	-0.7025	0.0264
Q9Y6M5	SLC30A1	-0.7034	0.0112
Q6P1L8	MRPL14	-0.7039	0.0375
Q9UH62	ARMCX3	-0.7049	0.0014
Q99757	TXN2	-0.7060	0.0017
O60231	DHX16	-0.7100	0.0229
O00161	SNAP23	-0.7116	0.0000
Q9H3P7	ACBD3	-0.7139	0.0046
P09132	SRP19	-0.7161	0.0017
Q8TAE8	GADD45GIP1	-0.7167	0.0438
Q14019	COTL1	-0.7221	0.0110
Q9NUQ7	UFSP2	-0.7258	0.0105
P30047	GCHFR	-0.7267	0.0139
Q15819	UBE2V2	-0.7276	0.0201
P61758	VBP1	-0.7277	0.0019
Q96C57	C12orf43	-0.7353	0.0331
Q9UIL1	SCOC	-0.7413	0.0007
P83876	TXNL4A	-0.7447	0.0162
Q00403	GTF2B	-0.7467	0.0139
Q96QD8	SLC38A2	-0.7471	0.0309
Q03518	TAP1	-0.7491	0.0314
O00233	PSMD9	-0.7507	0.0164
Q70CQ2	USP34	-0.7507	0.0094
Q86T03	PIP4P1	-0.7526	0.0389
Q96G23	CERS2	-0.7614	0.0008
Q7Z4G4	TRMT11	-0.7649	0.0204
Q9UEW8	STK39	-0.7702	0.0001
Q6UW63	POGLUT2	-0.7722	0.0080

Q96S97	MYADM	-0.7735	0.0187
Q9UNN5	FAF1	-0.7741	0.0092
Q12959	DLG1	-0.7784	0.0047
Q9Y3E0	GOLT1B	-0.7964	0.0041
Q96PY5	FMNL2	-0.8008	0.0043
Q08170	SRSF4	-0.8020	0.0422
Q9UI26	IPO11	-0.8052	0.0124
O14957	UQCR11	-0.8109	0.0174
Q8N0U8	VKORC1L1	-0.8115	0.0270
P83111	LACTB	-0.8121	0.0148
O95139	NDUFB6	-0.8128	0.0015
Q07812	BAX	-0.8233	0.0015
Q9NZQ3	NCKIPSD	-0.8240	0.0003
P32519	ELF1	-0.8294	0.0052
P37059	HSD17B2	-0.8430	0.0286
Q92783	STAM	-0.8470	0.0106
Q92925	SMARCD2	-0.8490	0.0054
Q9H9P8	L2HGDH	-0.8502	0.0422
P51580	TPMT	-0.8526	0.0014
Q9NTG7	SIRT3	-0.8555	0.0358
Q9BSH5	HDHD3	-0.8591	0.0258
P22059	OSBP	-0.8610	0.0076
Q9Y5J7	TIMM9	-0.8611	0.0359
Q14790	CASP8	-0.8653	0.0085
Q14146	URB2	-0.8700	0.0003
Q15286	RAB35	-0.8815	0.0091
Q9C0I1	MTMR12	-0.8868	0.0082
P02649	APOE	-0.8901	0.0292
Q13217	DNAJC3	-0.8933	0.0012
Q49A26	GLYR1	-0.8980	0.0058
Q9BRJ7	NUDT16L1	-0.9051	0.0005
Q32MZ4	LRRFIP1	-0.9095	0.0049
Q14684	RRP1B	-0.9121	0.0046
Q9BZH6	WDR11	-0.9239	0.0052
Q9P260	RELCH	-0.9531	0.0065
Q9Y2W2	WBP11	-0.9570	0.0055
P15529	CD46	-0.9608	0.0013
P02753	RBP4	-0.9619	0.0400
P57105	SYNJ2BP	-0.9653	0.0062
Q86TS9	MRPL52	-0.9804	0.0101
O60518	RANBP6	-0.9827	0.0172
P38571	LIPA	-1.0018	0.0495
O14732	IMPA2	-1.0086	0.0472
Q9NP61	ARFGAP3	-1.0279	0.0053
Q96BP2	CHCHD1	-1.0439	0.0321
Q9BXP2	SLC12A9	-1.0457	0.0001
Q8NAV1	PRPF38A	-1.0508	0.0137
Q86TM6	SYVN1	-1.0530	0.0123
Q9BVJ6	UTP14A	-1.0637	0.0004
Q9H0U6	MRPL18	-1.0638	0.0081
Q96GQ5	RUSF1	-1.0772	0.0002
P37235	HPCAL1	-1.0889	0.0123
Q96HR3	MED30	-1.1124	0.0001
Q9BVL2	NUP58	-1.1125	0.0160

<b>Q96JB5</b>	CDK5RAP3	-1.1216	0.0024
<b>O14735</b>	CDIPT	-1.1326	0.0100
<b>Q9H1P3</b>	OSBPL2	-1.1452	0.0024
<b>Q8TB61</b>	SLC35B2	-1.2167	0.0024
<b>Q9Y5B0</b>	CTDP1	-1.2286	0.0015
<b>Q13526</b>	PIN1	-1.2479	0.0191
<b>Q15526</b>	SURF1	-1.2517	0.0001
<b>Q9HA64</b>	FN3KRP	-1.2552	0.0159
<b>Q9UBU6</b>	FAM8A1	-1.2554	0.0149
<b>P61020</b>	RAB5B	-1.2708	0.0156
<b>Q9NRP0</b>	OSTC	-1.2724	0.0172
<b>Q9HC07</b>	TMEM165	-1.2769	0.0477
<b>O95400</b>	CD2BP2	-1.2880	0.0221
<b>Q8NBQ7</b>	AQP11	-1.3060	0.0149
<b>Q9H3H5</b>	DPAGT1	-1.3190	0.0002
<b>P52758</b>	RIDA	-1.3304	0.0378
<b>Q9NUL5</b>	SHFL	-1.4309	0.0190
<b>P62072</b>	TIMM10	-1.4557	0.0074
<b>P52655</b>	GTF2A1	-1.4783	0.0005
<b>Q96HR8</b>	NAF1	-1.5248	0.0450
<b>O75208</b>	COQ9	-1.5594	0.0006
<b>Q86WJ1</b>	CHD1L	-1.5629	0.0058
<b>P78383</b>	SLC35B1	-1.5892	0.0001
<b>Q9Y3B9</b>	RRP15	-1.5896	0.0071
<b>P26885</b>	FKBP2	-1.7105	0.0013
<b>Q96B49</b>	TOMM6	-1.7184	0.0036
<b>Q969S9</b>	GFM2	-1.7417	0.0218
<b>P35914</b>	HMGCL	-1.9557	0.0143
<b>Q8IZP0</b>	ABI1	-2.0944	0.0007
<b>Q8IZ21</b>	PHACTR4	-2.2056	0.0327
<b>P62745</b>	RHOB	-2.7949	0.0415
<b>Q6RFH5</b>	WDR74	-2.7964	0.0019
<b>O43402</b>	EMC8	-3.0990	0.0150
<b>Q9NVH6</b>	TMLHE	-5.4533	0.0012

**LO + I + 9mf VS LO + I**

<b>ID</b>	<b>Symbol</b>	<b>Expr Log Ratio</b>	<b>Expr p-value</b>
<b>Q9HB90</b>	RRAGC	2.5642	0.0021
<b>O43402</b>	EMC8	2.2530	0.0010
<b>Q9H3H5</b>	DPAGT1	2.0181	0.0000
<b>Q15526</b>	SURF1	1.9737	0.0000
<b>P25311</b>	AZGP1	1.9229	0.0144
<b>P52758</b>	RIDA	1.8767	0.0178
<b>P62072</b>	TIMM10	1.8580	0.0173
<b>Q8IZP0</b>	ABI1	1.8518	0.0055
<b>Q0VGL1</b>	LAMTOR4	1.7615	0.0002
<b>Q9NUL5</b>	SHFL	1.6859	0.0255
<b>O95807</b>	TMEM50A	1.5729	0.0134
<b>Q9BTE7</b>	DCUN1D5	1.4312	0.0338
<b>Q9HC21</b>	SLC25A19	1.4154	0.0011
<b>Q9BV40</b>	VAMP8	1.3909	0.0053
<b>P13473</b>	LAMP2	1.3571	0.0081
<b>Q13438</b>	OS9	1.3555	0.0182
<b>Q15043</b>	SLC39A14	1.3451	0.0145
<b>Q9NRP0</b>	OSTC	1.3284	0.0344
<b>Q96B49</b>	TOMM6	1.3089	0.0070
<b>Q86YN1</b>	DOLPP1	1.3079	0.0325
<b>P52657</b>	GTF2A2	1.3001	0.0226
<b>P07148</b>	FABP1	1.2819	0.0354
<b>Q9UBU6</b>	FAM8A1	1.2792	0.0292
<b>Q86T03</b>	PIP4P1	1.2719	0.0324
<b>Q9NVH6</b>	TMLHE	1.2073	0.0001
<b>Q9BX66</b>	SORBS1	1.2052	0.0499
<b>Q8NFAQ8</b>	TOR1AIP2	1.1794	0.0263
<b>P48634</b>	PRRC2A	1.1570	0.0177
<b>Q9BYJ9</b>	YTHDF1	1.1505	0.0178
<b>Q15738</b>	NSDHL	1.1201	0.0362
<b>Q86TS9</b>	MRPL52	1.0499	0.0262
<b>O14735</b>	CDIPT	1.0270	0.0145
<b>Q92947</b>	GCDH	1.0210	0.0090
<b>O75410</b>	TACC1	1.0109	0.0037
<b>O95563</b>	MPC2	1.0016	0.0085
<b>P35610</b>	SOAT1	0.9936	0.0235
<b>P52655</b>	GTF2A1	0.9872	0.0244
<b>P60520</b>	GABARAPL2	0.9823	0.0109
<b>P52895</b>	AKR1C1/AKR1C2	0.9712	0.0168
<b>P40616</b>	ARL1	0.9535	0.0027
<b>P61758</b>	VBP1	0.9410	0.0134
<b>P54886</b>	ALDH18A1	0.9336	0.0201
<b>Q15041</b>	ARL6IP1	0.9182	0.0001
<b>Q9H4A6</b>	GOLPH3	0.9120	0.0391
<b>Q15796</b>	SMAD2	0.9068	0.0300
<b>Q9BXP2</b>	SLC12A9	0.8935	0.0090
<b>Q04323</b>	UBXN1	0.8914	0.0053
<b>P20823</b>	HNF1A	0.8652	0.0442
<b>Q9Y5J7</b>	TIMM9	0.8627	0.0274
<b>Q9UEW8</b>	STK39	0.8588	0.0000
<b>P16455</b>	MGMT	0.8462	0.0164

P36551	CPOX	0.8444	0.0017
Q969X1	TMBIM1	0.8337	0.0153
Q9H7L9	SUDS3	0.8301	0.0142
P21695	GPD1	0.8126	0.0155
Q96A26	FAM162A	0.8035	0.0029
P14324	FDPS	0.7975	0.0467
Q6P1X6	C8orf82	0.7902	0.0298
O43617	TRAPPC3	0.7900	0.0199
Q9Y6M5	SLC30A1	0.7775	0.0138
Q15904	ATP6AP1	0.7765	0.0053
Q8WVK2	SNRNP27	0.7555	0.0062
P20020	ATP2B1	0.7507	0.0215
Q5T8P6	RBM26	0.7473	0.0171
Q8WW59	SPRYD4	0.7453	0.0406
P25786	PSMA1	0.7441	0.0015
Q9ULC5	ACSL5	0.7434	0.0150
Q9H2W6	MRPL46	0.7221	0.0487
Q70CQ2	USP34	0.7168	0.0362
O00139	KIF2A	0.7137	0.0292
Q7L5D6	GET4	0.7067	0.0085
Q96GQ5	RUSF1	0.7024	0.0232
Q9UKX7	NUP50	0.7012	0.0089
Q9NZJ9	NUDT4	0.6940	0.0111
P99999	CYCS	0.6912	0.0042
Q9BWE0	REPIN1	0.6880	0.0072
P11234	RALB	0.6874	0.0033
Q4VC31	MIX23	0.6865	0.0104
O95081	AGFG2	0.6818	0.0175
Q8N3C0	ASCC3	0.6810	0.0062
P18085	ARF4	0.6773	0.0002
Q96QD8	SLC38A2	0.6735	0.0461
P04179	SOD2	0.6729	0.0021
Q16719	KYNU	0.6716	0.0430
P17252	PRKCA	0.6708	0.0174
Q9Y3B7	MRPL11	0.6684	0.0212
Q9HC07	TMEM165	0.6649	0.0403
P63272	SUPT4H1	0.6588	0.0002
Q9UBB9	TFIP11	0.6570	0.0491
Q92882	OSTF1	0.6400	0.0378
Q8WTV0	SCARB1	0.6328	0.0379
P36543	ATP6V1E1	0.6275	0.0369
O94760	DDAH1	0.6246	0.0044
Q9Y3E0	GOLT1B	0.6175	0.0165
O95232	LUC7L3	0.6136	0.0002
P20618	PSMB1	0.5999	0.0176
Q9NZN3	EHD3	0.5965	0.0053
P23141	CES1	0.5922	0.0404
Q7Z3C6	ATG9A	0.5886	0.0048
Q9Y6M9	NDUFB9	-0.5817	0.0137
Q14790	CASP8	-0.5826	0.0057
P78406	RAE1	-0.5836	0.0116
P60660	MYL6	-0.5856	0.0002
P00395	MT-CO1	-0.5876	0.0081
P08708	RPS17	-0.5877	0.0001

P12931	SRC	-0.5900	0.0154
O75955	FLOT1	-0.5916	0.0339
P07954	FH	-0.5920	0.0036
Q9P000	COMMD9	-0.5996	0.0147
Q07955	SRSF1	-0.6027	0.0062
Q9H2P9	DPH5	-0.6041	0.0371
Q13242	SRSF9	-0.6050	0.0068
P52907	CAPZA1	-0.6050	0.0010
Q8NEJ9	NGDN	-0.6053	0.0079
P62888	RPL30	-0.6088	0.0148
O94855	SEC24D	-0.6107	0.0007
P63261	ACTG1	-0.6132	0.0000
O94874	UFL1	-0.6137	0.0017
P62273	RPS29	-0.6141	0.0462
P53384	NUBP1	-0.6166	0.0035
Q7Z5K2	WAPL	-0.6170	0.0091
Q96IF1	AJUBA	-0.6175	0.0008
Q07817	BCL2L1	-0.6220	0.0001
P49321	NASP	-0.6237	0.0000
Q8WY22	BRI3BP	-0.6239	0.0123
P62714	PPP2CB	-0.6301	0.0028
Q7Z7K6	CENPV	-0.6336	0.0012
P62873	GNB1	-0.6349	0.0159
Q13492	PICALM	-0.6354	0.0203
P19022	CDH2	-0.6386	0.0013
P10619	CTSA	-0.6387	0.0009
P08754	GNAI3	-0.6390	0.0427
P08238	HSP90AB1	-0.6404	0.0000
Q14651	PLS1	-0.6445	0.0025
P35221	CTNNA1	-0.6454	0.0046
Q14257	RCN2	-0.6459	0.0437
Q96ME7	ZNF512	-0.6488	0.0096
Q86VR2	RETREG3	-0.6491	0.0391
Q9NQR4	NIT2	-0.6519	0.0391
P49821	NDUFV1	-0.6521	0.0002
P49354	FNTA	-0.6560	0.0147
O75781	PALM	-0.6612	0.0011
P54802	NAGLU	-0.6623	0.0214
P32754	HPD	-0.6628	0.0007
Q96ER3	SAAL1	-0.6664	0.0365
Q9H9Y2	RPF1	-0.6695	0.0129
Q13547	HDAC1	-0.6714	0.0191
Q92925	SMARCD2	-0.6722	0.0233
O43765	SGTA	-0.6739	0.0006
Q96SB4	SRPK1	-0.6743	0.0044
O00629	KPNA4	-0.6759	0.0003
Q13451	FKBP5	-0.6770	0.0052
Q96FC7	PHYHIPL	-0.6798	0.0000
Q92597	NDRG1	-0.6802	0.0201
O43488	AKR7A2	-0.6804	0.0105
O15027	SEC16A	-0.6805	0.0205
O14979	HNRNPDL	-0.6811	0.0068
P05787	KRT8	-0.6812	0.0000
O15145	ARPC3	-0.6821	0.0022

<b>Q9BZE9</b>	ASPSCR1	-0.6844	0.0163
<b>Q99622</b>	C12orf57	-0.6889	0.0068
<b>P17844</b>	DDX5	-0.6901	0.0066
<b>O95758</b>	PTBP3	-0.6943	0.0010
<b>P37108</b>	SRP14	-0.6946	0.0000
<b>P53582</b>	METAP1	-0.6981	0.0035
<b>P02786</b>	TFRC	-0.7004	0.0001
<b>Q08209</b>	PPP3CA	-0.7013	0.0015
<b>P31150</b>	GDI1	-0.7016	0.0054
<b>P08134</b>	RHOC	-0.7016	0.0001
<b>Q00688</b>	FKBP3	-0.7019	0.0042
<b>P35237</b>	SERPINB6	-0.7049	0.0004
<b>Q14137</b>	BOP1	-0.7080	0.0001
<b>P21333</b>	FLNA	-0.7101	0.0010
<b>Q9UBD5</b>	ORC3	-0.7120	0.0085
<b>O43491</b>	EPB41L2	-0.7159	0.0000
<b>Q8IX18</b>	DHX40	-0.7211	0.0167
<b>P37802</b>	TAGLN2	-0.7212	0.0001
<b>P35080</b>	PFN2	-0.7322	0.0029
<b>Q96N66</b>	MBOAT7	-0.7336	0.0048
<b>O95819</b>	MAP4K4	-0.7352	0.0072
<b>Q93062</b>	RBPM5	-0.7360	0.0026
<b>Q9Y3B3</b>	TMED7	-0.7368	0.0008
<b>P08727</b>	KRT19	-0.7373	0.0002
<b>P55081</b>	MFAP1	-0.7375	0.0152
<b>Q969X5</b>	ERGIC1	-0.7407	0.0244
<b>P46108</b>	CRK	-0.7426	0.0311
<b>P49458</b>	SRP9	-0.7429	0.0038
<b>Q15397</b>	PUM3	-0.7467	0.0104
<b>Q96DX5</b>	ASB9	-0.7480	0.0090
<b>Q9NZZ3</b>	CHMP5	-0.7481	0.0437
<b>Q66K74</b>	MAP1S	-0.7486	0.0192
<b>Q15648</b>	MED1	-0.7559	0.0295
<b>Q9BZH6</b>	WDR11	-0.7573	0.0074
<b>Q15843</b>	NEDD8	-0.7670	0.0026
<b>Q9NVS9</b>	PNPO	-0.7670	0.0100
<b>P33527</b>	ABCC1	-0.7688	0.0137
<b>Q9Y3D3</b>	MRPS16	-0.7710	0.0154
<b>Q01995</b>	TAGLN	-0.7736	0.0006
<b>Q8NAV1</b>	PRPF38A	-0.7762	0.0169
<b>Q7LGA3</b>	HS2ST1	-0.7779	0.0053
<b>Q13509</b>	TUBB3	-0.7816	0.0061
<b>P42858</b>	HTT	-0.7836	0.0001
<b>Q9Y5Z4</b>	HEBP2	-0.7881	0.0002
<b>O96019</b>	ACTL6A	-0.7887	0.0003
<b>O75569</b>	PRKRA	-0.7896	0.0019
<b>Q96HQ2</b>	CDKN2AIPNL	-0.7918	0.0003
<b>Q5XKE5</b>	KRT79	-0.7921	0.0010
<b>Q96H79</b>	ZC3HAV1L	-0.7931	0.0384
<b>P35244</b>	RPA3	-0.7944	0.0017
<b>Q07157</b>	TJP1	-0.7961	0.0025
<b>P62633</b>	CNBP	-0.8005	0.0009
<b>Q9NT62</b>	ATG3	-0.8039	0.0000
<b>P16403</b>	H1-2	-0.8052	0.0000

P15848	ARSB	-0.8063	0.0098
P36578	RPL4	-0.8066	0.0001
P11310	ACADM	-0.8070	0.0073
P11047	LAMC1	-0.8071	0.0062
Q06546	GABPA	-0.8082	0.0422
O60508	CDC40	-0.8155	0.0002
Q14847	LASP1	-0.8168	0.0000
Q14344	GNA13	-0.8178	0.0071
Q9Y6N5	SQOR	-0.8217	0.0048
Q6VN20	RANBP10	-0.8234	0.0430
Q8IUF8	RIOX2	-0.8251	0.0302
Q9UNP9	PPIE	-0.8313	0.0393
P02749	APOH	-0.8332	0.0126
Q9Y5X1	SNX9	-0.8371	0.0009
P78310	CXADR	-0.8434	0.0018
O14639	ABLIM1	-0.8461	0.0056
Q12797	ASPH	-0.8477	0.0001
Q13557	CAMK2D	-0.8517	0.0169
Q8NEY8	PPHLN1	-0.8537	0.0021
O95249	GOSR1	-0.8591	0.0060
Q69YQ0	SPECC1L	-0.8597	0.0036
P07203	GPX1	-0.8628	0.0013
P24666	ACP1	-0.8633	0.0001
O15514	POLR2D	-0.8719	0.0002
O75448	MED24	-0.8727	0.0216
P63220	RPS21	-0.8754	0.0000
Q5UIP0	RIF1	-0.8759	0.0000
P42330	AKR1C3	-0.8766	0.0000
Q9UJY4	GGA2	-0.8774	0.0095
P13861	PRKAR2A	-0.8814	0.0001
P52435	POLR2J	-0.8839	0.0025
Q16181	SEPTIN7	-0.8843	0.0001
P35914	HMGCL	-0.8895	0.0396
P08243	ASNS	-0.8904	0.0025
O14802	POLR3A	-0.8940	0.0018
P62899	RPL31	-0.8947	0.0007
P67870	CSNK2B	-0.8976	0.0010
Q2TAA2	IAH1	-0.8980	0.0133
Q16540	MRPL23	-0.9022	0.0156
Q9NX47	MARCHF5	-0.9161	0.0275
P13051	UNG	-0.9183	0.0046
P04066	FUCA1	-0.9187	0.0031
Q9NQ94	A1CF	-0.9231	0.0096
Q12800	TFCP2	-0.9272	0.0017
Q9Y2H6	FNDC3A	-0.9338	0.0137
Q9P2X0	DPM3	-0.9341	0.0392
Q9NPF0	CD320	-0.9347	0.0443
Q9NYH9	UTP6	-0.9369	0.0021
P30740	SERPINB1	-0.9405	0.0007
Q9Y6K9	IKBKG	-0.9440	0.0237
Q14126	DSG2	-0.9483	0.0096
Q9UKY7	CDV3	-0.9488	0.0000
O75718	CRTAP	-0.9498	0.0044
P62875	POLR2L	-0.9512	0.0018

<b>P27361</b>	MAPK3	-0.9581	0.0065
<b>Q9UHI6</b>	DDX20	-0.9609	0.0059
<b>P51668</b>	UBE2D1	-0.9612	0.0002
<b>Q01844</b>	EWSR1	-0.9644	0.0000
<b>Q96LZ7</b>	RMDN2	-0.9657	0.0004
<b>O15460</b>	P4HA2	-0.9657	0.0119
<b>O95197</b>	RTN3	-0.9660	0.0014
<b>P36969</b>	GPX4	-0.9668	0.0013
<b>P53367</b>	ARFIP1	-0.9730	0.0380
<b>Q96I15</b>	SCLY	-0.9765	0.0125
<b>Q9BUJ2</b>	HNRNPUL1	-0.9788	0.0003
<b>Q99470</b>	SDF2	-0.9869	0.0254
<b>O15116</b>	LSM1	-0.9923	0.0102
<b>Q13247</b>	SRSF6	-0.9947	0.0180
<b>Q7RTV0</b>	PHF5A	-0.9983	0.0022
<b>O60739</b>	EIF1B	-1.0050	0.0022
<b>Q9UQB8</b>	BAIAP2	-1.0063	0.0174
<b>P63167</b>	DYNLL1	-1.0116	0.0000
<b>Q9UPU5</b>	USP24	-1.0212	0.0020
<b>P19823</b>	ITIH2	-1.0254	0.0101
<b>P60709</b>	ACTB	-1.0255	0.0000
<b>P50416</b>	CPT1A	-1.0284	0.0022
<b>Q96K37</b>	SLC35E1	-1.0366	0.0009
<b>P67809</b>	YBX1	-1.0543	0.0001
<b>Q9Y697</b>	NFS1	-1.0771	0.0041
<b>O14773</b>	TPP1	-1.0786	0.0009
<b>Q99961</b>	SH3GL1	-1.0900	0.0000
<b>Q96PE7</b>	MCEE	-1.1055	0.0001
<b>Q9H9T3</b>	ELP3	-1.1095	0.0089
<b>Q27J81</b>	INF2	-1.1155	0.0447
<b>Q8IXB1</b>	DNAJC10	-1.1200	0.0008
<b>O75843</b>	AP1G2	-1.1314	0.0498
<b>Q05397</b>	PTK2	-1.1359	0.0214
<b>P01024</b>	C3	-1.1362	0.0084
<b>O75494</b>	SRSF10	-1.1436	0.0005
<b>P52756</b>	RBM5	-1.1479	0.0058
<b>P04156</b>	PRNP	-1.1622	0.0001
<b>Q03518</b>	TAP1	-1.1632	0.0023
<b>P29083</b>	GTF2E1	-1.1695	0.0000
<b>P11169</b>	SLC2A3	-1.1865	0.0000
<b>P07108</b>	DBI	-1.1898	0.0041
<b>Q8NBZ7</b>	UXS1	-1.1989	0.0011
<b>P12694</b>	BCKDHA	-1.2056	0.0148
<b>P62736</b>	ACTA2	-1.2063	0.0000
<b>Q9GZS3</b>	WDR61	-1.2097	0.0009
<b>O75368</b>	SH3BGRL	-1.2164	0.0009
<b>O60443</b>	GSDME	-1.2288	0.0041
<b>P49326</b>	FMO5	-1.2314	0.0015
<b>Q96AD5</b>	PNPLA2	-1.2399	0.0095
<b>P14854</b>	COX6B1	-1.2402	0.0000
<b>Q02809</b>	PLOD1	-1.2464	0.0021
<b>P15289</b>	ARSA	-1.2498	0.0365
<b>O14967</b>	CLGN	-1.2642	0.0415
<b>P11717</b>	IGF2R	-1.2659	0.0030

P41235	HNF4A	-1.2705	0.0106
P53041	PPP5C	-1.2742	0.0003
Q6UW68	TMEM205	-1.2772	0.0000
P52565	ARHGDI A	-1.2803	0.0000
Q9UK41	VPS28	-1.2895	0.0031
P61353	RPL27	-1.2963	0.0001
O00308	WWP2	-1.2964	0.0153
P00734	F2	-1.2991	0.0020
Q96CW5	TUBGCP3	-1.2995	0.0119
Q9BW72	HIGD2A	-1.3008	0.0000
P11166	SLC2A1	-1.3079	0.0030
P07942	LAMB1	-1.3193	0.0066
Q9BQ95	ECSIT	-1.3195	0.0160
Q86TG7	PEG10	-1.3238	0.0020
Q8IZA0	KIAA0319L	-1.3240	0.0007
Q969H8	MYDGF	-1.3355	0.0000
P56199	ITGA1	-1.3397	0.0032
Q9NWW4	CZIB	-1.3456	0.0029
Q8WVQ1	CANT1	-1.3511	0.0399
P63313	TMSB10/TMSB4X	-1.3576	0.0000
Q8WXA9	SREK1	-1.3733	0.0054
P06865	HEXA	-1.3793	0.0007
P07307	ASGR2	-1.3823	0.0074
Q5R3I4	TTC38	-1.4083	0.0073
P01034	CST3	-1.4153	0.0000
P02753	RBP4	-1.4176	0.0118
Q9BY67	CADM1	-1.4330	0.0000
O14880	MGST3	-1.4367	0.0006
O96013	PAK4	-1.4368	0.0115
Q7Z739	YTHDF3	-1.4427	0.0013
P01344	IGF2	-1.4470	0.0020
O95721	SNAP29	-1.4491	0.0134
O95470	SGPL1	-1.4760	0.0000
P07306	ASGR1	-1.4770	0.0014
P02763	ORM1	-1.4845	0.0094
Q99735	MGST2	-1.4852	0.0015
Q96A49	SYAP1	-1.4884	0.0106
P08697	SERPINF2	-1.5059	0.0003
Q9NPA0	EMC7	-1.5077	0.0023
Q96KA5	CLPTM1L	-1.5113	0.0016
Q6PUV4	CPLX2	-1.5241	0.0005
Q96C90	PPP1R14B	-1.5450	0.0000
Q12768	WASHC5	-1.5571	0.0271
Q9NUK0	MBNL3	-1.5776	0.0000
P35790	CHKA	-1.5955	0.0333
Q86WJ1	CHD1L	-1.5969	0.0007
P02679	FGG	-1.6168	0.0037
O75891	ALDH1L1	-1.6197	0.0032
P07711	CTSL	-1.6324	0.0002
Q9H299	SH3BGRL3	-1.6401	0.0001
Q9NY61	AATF	-1.6609	0.0043
O95139	NDUFB6	-1.6742	0.0132
O15230	LAMA5	-1.6993	0.0038
O00584	RNASET2	-1.7122	0.0011

<b>Q9BUR5</b>	APOO	-1.7273	0.0022
<b>Q99569</b>	PKP4	-1.7392	0.0018
<b>P30049</b>	ATP5F1D	-1.7690	0.0000
<b>O95298</b>	NDUFC2	-1.7691	0.0000
<b>P21980</b>	TGM2	-1.7991	0.0004
<b>P31947</b>	SFN	-1.8003	0.0014
<b>P47914</b>	RPL29	-1.8073	0.0000
<b>Q96PU4</b>	UHRF2	-1.8474	0.0060
<b>Q9P0M9</b>	MRPL27	-1.8679	0.0087
<b>P09455</b>	RBP1	-1.9108	0.0005
<b>Q9Y371</b>	SH3GLB1	-1.9294	0.0017
<b>Q8NB37</b>	GATD1	-1.9888	0.0000
<b>O43674</b>	NDUFB5	-2.0467	0.0000
<b>P14543</b>	NID1	-2.0721	0.0058
<b>P02671</b>	FGA	-2.1676	0.0016
<b>Q92504</b>	SLC39A7	-2.1694	0.0000
<b>Q14192</b>	FHL2	-2.1931	0.0351
<b>P09668</b>	CTSH	-2.2159	0.0009
<b>Q86VM9</b>	ZC3H18	-2.3226	0.0132
<b>Q9UHD9</b>	UBQLN2	-2.3634	0.0002
<b>P62854</b>	RPS26	-2.4523	0.0000
<b>P02751</b>	FN1	-2.5951	0.0005
<b>P02675</b>	FGB	-2.7976	0.0012
<b>Q5EBL8</b>	PDZD11	-2.8188	0.0336
<b>P02765</b>	AHSG	-2.8583	0.0003
<b>P18827</b>	SDC1	-3.4144	0.0004
<b>P10646</b>	TFPI	-4.0282	0.0001
<b>Q99538</b>	LGMN	-4.0550	0.0000
<b>P02788</b>	LTF	-5.7654	0.0000

**LO + I + 9i VS LO + I**

<b>ID</b>	<b>Symbol</b>	<b>Expr Log Ratio</b>	<b>Expr p-value</b>
Q9NVH6	TMLHE	5.7959	0.0235
O43402	EMC8	2.6420	0.0000
Q9H3Q1	CDC42EP4	2.0571	0.0191
P11182	DBT	1.9937	0.0058
P09601	HMOX1	1.9415	0.0007
P62072	TIMM10	1.8723	0.0078
Q0VGL1	LAMTOR4	1.5555	0.0001
Q8NC44	RETREG2	1.4847	0.0069
Q86T03	PIP4P1	1.3152	0.0003
Q9Y5B0	CTDP1	1.3040	0.0093
P52655	GTF2A1	1.2001	0.0021
P84101	SERF2	1.1980	0.0070
O95400	CD2BP2	1.1877	0.0152
Q96DX5	ASB9	1.1775	0.0036
Q15526	SURF1	1.1381	0.0075
Q9BZX2	UCK2	1.1073	0.0214
Q8NBQ7	AQP11	1.0476	0.0005
Q9H7L9	SUDS3	1.0410	0.0456
O14763	TNFRSF10B	1.0347	0.0007
Q96JB5	CDK5RAP3	1.0334	0.0024
Q9Y2Y0	ARL2BP	1.0322	0.0006
Q6PK18	OGFOD3	1.0277	0.0102
Q04323	UBXN1	1.0248	0.0314
Q15796	SMAD2	1.0208	0.0275
P28676	GCA	1.0163	0.0003
Q86TS9	MRPL52	0.9917	0.0015
P02647	APOA1	0.9755	0.0013
Q9NRF9	POLE3	0.9623	0.0067
Q969S9	GFM2	0.9565	0.0136
Q8WW59	SPRYD4	0.9508	0.0056
Q86TG7	PEG10	0.9448	0.0135
Q9NWT6	HIF1AN	0.9395	0.0240
O95807	TMEM50A	0.8929	0.0498
Q96GQ5	RUSF1	0.8786	0.0118
Q86Y56	DNAAF5	0.8751	0.0044
Q9H9T3	ELP3	0.8674	0.0154
Q53EL6	PDCD4	0.8609	0.0001
Q9UJC3	HOOK1	0.8512	0.0166
Q9P260	RELCH	0.8504	0.0004
Q9NRP0	OSTC	0.8491	0.0016
Q5T2E6	ARMH3	0.8383	0.0280
O75208	COQ9	0.8266	0.0236
Q9UBC2	EPS15L1	0.8265	0.0093
Q8TF68	ZNF384	0.8242	0.0198
Q9NRN9	METTL5	0.8110	0.0458
P33897	ABCD1	0.8070	0.0311
Q9UBB4	ATXN10	0.7966	0.0088
Q9HC21	SLC25A19	0.7949	0.0033
P09455	RBP1	0.7900	0.0280
O00139	KIF2A	0.7701	0.0089
Q9NZQ3	NCKIPSD	0.7451	0.0054

Q9P0J7	KCMF1	0.7425	0.0146
Q8WVK2	SNRNP27	0.7365	0.0325
Q15836	VAMP3	0.7363	0.0038
Q14451	GRB7	0.7354	0.0016
O95819	MAP4K4	0.7338	0.0098
Q8IZ83	ALDH16A1	0.7323	0.0063
O00273	DFFA	0.7309	0.0417
Q96DG6	CMBL	0.7133	0.0045
P10644	PRKAR1A	0.6968	0.0051
Q9NTG7	SIRT3	0.6924	0.0408
Q9BWS9	CHID1	0.6912	0.0194
Q9NRX1	PNO1	0.6884	0.0019
Q8NC54	C5orf15	0.6853	0.0294
O00754	MAN2B1	0.6850	0.0216
P54619	PRKAG1	0.6776	0.0085
Q9NZB2	FAM120A	0.6773	0.0498
Q8WVY7	UBLCP1	0.6689	0.0385
Q9UEE9	CFDP1	0.6685	0.0043
P07711	CTSL	0.6660	0.0094
Q5T8P6	RBM26	0.6639	0.0002
O96011	PEX11B	0.6596	0.0428
Q8TB36	GDAP1	0.6531	0.0125
Q92542	NCSTN	0.6304	0.0291
Q14746	COG2	0.6196	0.0002
O95342	ABCB11	0.6165	0.0140
Q5VWZ2	LYPLAL1	0.6107	0.0181
Q8WVC6	DCAKD	0.5940	0.0403
P33121	ACSL1	0.5890	0.0001
O95999	BCL10	0.5887	0.0092
P61457	PCBD1	0.5872	0.0109
P56937	HSD17B7	0.5855	0.0044
Q99624	SLC38A3	0.5847	0.0153
Q9UKR5	ERG28	0.5840	0.0023
Q15043	SLC39A14	-0.5906	0.0273
P52292	KPNA2	-0.5983	0.0250
Q8NBQ5	HSD17B11	-0.6003	0.0026
Q9P0S9	TMEM14C	-0.6010	0.0209
Q6P1J9	CDC73	-0.6010	0.0029
O00767	SCD	-0.6025	0.0369
P56199	ITGA1	-0.6026	0.0379
Q9UDY8	MALT1	-0.6064	0.0364
P15848	ARSB	-0.6072	0.0298
Q08AG7	MZT1	-0.6150	0.0260
O43819	SCO2	-0.6179	0.0441
Q14145	KEAP1	-0.6275	0.0293
P48509	CD151	-0.6314	0.0338
P07148	FABP1	-0.6415	0.0002
Q15758	SLC1A5	-0.6478	0.0083
Q9BW60	ELOVL1	-0.6572	0.0354
P11388	TOP2A	-0.6584	0.0000
Q9Y697	NFS1	-0.6592	0.0275
Q9NZ45	CISD1	-0.6685	0.0236
Q9Y221	NIP7	-0.6739	0.0269
Q96HR8	NAF1	-0.6756	0.0434

<b>Q9UN36</b>	NDRG2	-0.6810	0.0368
<b>Q96T37</b>	RBM15	-0.6872	0.0021
<b>Q9UH62</b>	ARMCX3	-0.7031	0.0385
<b>O75381</b>	PEX14	-0.7131	0.0330
<b>O94925</b>	GLS	-0.7152	0.0057
<b>P05556</b>	ITGB1	-0.7281	0.0002
<b>Q13217</b>	DNAJC3	-0.7301	0.0007
<b>Q13496</b>	MTM1	-0.7302	0.0164
<b>Q92598</b>	HSPH1	-0.7357	0.0084
<b>Q5RI15</b>	COX20	-0.7359	0.0001
<b>P22413</b>	ENPP1	-0.7385	0.0001
<b>P05026</b>	ATP1B1	-0.7492	0.0317
<b>Q8TD30</b>	GPT2	-0.7506	0.0025
<b>P29992</b>	GNA11	-0.7544	0.0014
<b>O00469</b>	PLOD2	-0.7589	0.0027
<b>Q8NAV1</b>	PRPF38A	-0.8016	0.0378
<b>O15457</b>	MSH4	-0.8537	0.0220
<b>P31150</b>	GDI1	-0.8626	0.0151
<b>Q96HC4</b>	PDLIM5	-0.8628	0.0000
<b>O60739</b>	EIF1B	-0.8830	0.0104
<b>P15104</b>	GLUL	-0.8934	0.0282
<b>Q8NEY8</b>	PPHLN1	-0.8943	0.0022
<b>P54709</b>	ATP1B3	-0.9127	0.0077
<b>O14493</b>	CLDN4	-0.9228	0.0186
<b>P08962</b>	CD63	-0.9305	0.0117
<b>P50750</b>	CDK9	-0.9396	0.0128
<b>P16066</b>	NPR1	-0.9435	0.0152
<b>Q93034</b>	CUL5	-0.9443	0.0316
<b>Q9UMY4</b>	SNX12	-0.9445	0.0221
<b>P29317</b>	EPHA2	-0.9454	0.0100
<b>Q15035</b>	TRAM2	-0.9476	0.0162
<b>Q9NR56</b>	MBNL1	-0.9505	0.0242
<b>Q04828</b>	AKR1C1/AKR1C2	-0.9516	0.0385
<b>Q9Y3B9</b>	RRP15	-0.9564	0.0051
<b>O95197</b>	RTN3	-0.9688	0.0007
<b>O43617</b>	TRAPPC3	-0.9850	0.0072
<b>Q13769</b>	THOC5	-0.9957	0.0222
<b>P49841</b>	GSK3B	-1.0363	0.0285
<b>P52756</b>	RBM5	-1.0764	0.0492
<b>Q71RC2</b>	LARP4	-1.1101	0.0019
<b>P01034</b>	CST3	-1.1311	0.0001
<b>O15530</b>	PDPK1	-1.1504	0.0418
<b>Q6ZMG9</b>	CERS6	-1.2204	0.0247
<b>Q9H3K2</b>	GHITM	-1.2287	0.0018
<b>O00560</b>	SDCBP	-1.2517	0.0372
<b>P29558</b>	RBMS1	-1.2590	0.0014
<b>P04156</b>	PRNP	-1.2971	0.0000
<b>Q96QD8</b>	SLC38A2	-1.3212	0.0010
<b>P62834</b>	RAP1A	-1.3716	0.0042
<b>O15020</b>	SPTBN2	-1.3871	0.0281
<b>Q9BV40</b>	VAMP8	-1.3922	0.0183
<b>Q9Y5V0</b>	ZNF706	-1.4318	0.0212
<b>P02795</b>	MT2A	-1.4394	0.0281
<b>O60218</b>	AKR1B10	-1.4890	0.0173

<b>P27449</b>	ATP6V0C	-2.0960	0.0170
<b>O00116</b>	AGPS	-2.2481	0.0077
<b>Q96K49</b>	TMEM87B	-3.2411	0.0026

**LO + I + 9mf VS LO + I + 9i**

<b>ID</b>	<b>Symbol</b>	<b>Expr Log Ratio</b>	<b>Expr p-value</b>
Q9NQ94	A1CF	-1.2994	0.0006
Q13685	AAMP	0.5938	0.0417
Q9NY61	AATF	-1.1037	0.0043
P33527	ABCC1	-0.8230	0.0002
Q96IU4	ABHD14B	-0.8616	0.0000
Q8IZP0	ABI1	2.0199	0.0028
O14639	ABLIM1	-0.5873	0.0189
P11310	ACADM	-0.6046	0.0269
P24666	ACP1	-0.7862	0.0001
O95573	ACSL3	0.6229	0.0045
Q9ULC5	ACSL5	1.2185	0.0036
P62736	ACTA2	-0.8717	0.0002
P60709	ACTB	-0.7761	0.0001
P63261	ACTG1	-0.6057	0.0001
O96019	ACTL6A	-0.6298	0.0029
O14672	ADAM10	-0.6464	0.0016
Q9H2P0	ADNP	-0.6702	0.0315
O95081	AGFG2	1.0643	0.0040
O00116	AGPS	2.4452	0.0039
P02765	AHSG	-2.9539	0.0000
O95831	AIFM1	0.5877	0.0425
Q96IF1	AJUBA	-0.6623	0.0147
Q92667	AKAP1	-1.1395	0.0127
P15121	AKR1B1	2.2765	0.0010
O60218	AKR1B10	1.4046	0.0003
P52895	AKR1C1/AKR1C2	1.6035	0.0031
O43488	AKR7A2	-0.9161	0.0035
P54886	ALDH18A1	1.3118	0.0099
O75891	ALDH1L1	-1.0666	0.0015
O75843	AP1G2	-0.9797	0.0006
P02647	APOA1	-0.7844	0.0109
P02749	APOH	-1.3825	0.0000
Q9BUR5	APOO	-2.0395	0.0068
P07741	APRT	-0.6621	0.0003
Q96P48	ARAP1	-0.6918	0.0206
P18085	ARF4	0.6851	0.0001
Q8N6H7	ARFGAP2	-1.6277	0.0167
P52565	ARHGDI	-1.1269	0.0000
P40616	ARL1	0.8229	0.0076
Q15041	ARL6IP1	1.0531	0.0001
Q9UH62	ARMCX3	1.0891	0.0072
Q5T2E6	ARMH3	-0.8739	0.0499
O15143	ARPC1B	-0.5892	0.0004
Q96DX5	ASB9	-1.9256	0.0000
P07306	ASGR1	-1.1831	0.0000
P07307	ASGR2	-1.4790	0.0000
Q12797	ASPH	-0.9570	0.0000
Q9BZE9	ASPSCR1	-0.8874	0.0005
Q9NT62	ATG3	-0.8793	0.0033
Q8NHH9	ATL2	0.6244	0.0040
P05023	ATP1A1	1.1386	0.0004

P05026	ATP1B1	1.0198	0.0000
P54709	ATP1B3	0.9759	0.0004
P20020	ATP2B1	0.8463	0.0131
P30049	ATP5F1D	-1.6137	0.0000
Q15904	ATP6AP1	0.7740	0.0047
P27449	ATP6V0C	2.3607	0.0000
Q9UBB4	ATXN10	-1.2044	0.0001
P25311	AZGP1	1.4322	0.0065
Q9UQB8	BAIAP2	-0.8092	0.0250
P12694	BCKDHA	-1.6787	0.0006
Q14137	BOP1	-0.6105	0.0006
Q96K17	BTF3L4	-0.8033	0.0004
Q9H3H3	C11orf68	-0.5975	0.0001
Q96C57	C12orf43	0.8759	0.0131
P01024	C3	-1.2665	0.0001
Q9BY67	CADM1	-0.9119	0.0000
Q05682	CALD1	-0.5949	0.0044
Q13557	CAMK2D	-0.8380	0.0157
P52907	CAPZA1	-0.6689	0.0006
Q86X55	CARM1	-0.7159	0.0019
P16152	CBR1	-0.5821	0.0001
P48509	CD151	0.7208	0.0061
O95400	CD2BP2	-0.8638	0.0154
P15529	CD46	1.2026	0.0333
P08962	CD63	1.9959	0.0206
O60508	CDC40	-0.5830	0.0023
Q9H3Q1	CDC42EP4	-1.7293	0.0209
P19022	CDH2	-1.1773	0.0000
O14735	CDIPT	0.8931	0.0205
Q96JB5	CDK5RAP3	-0.7912	0.0004
Q96HQ2	CDKN2AIPNL	-0.9543	0.0000
Q9UKY7	CDV3	-0.6605	0.0001
Q7Z7K6	CENPV	-0.7151	0.0005
Q6ZMG9	CERS6	1.1123	0.0001
Q86WJ1	CHD1L	-2.2839	0.0006
Q9BWS9	CHID1	-1.0102	0.0012
P35790	CHKA	-2.0783	0.0001
Q9H444	CHMP4B	0.6863	0.0023
Q9NZZ3	CHMP5	-0.8126	0.0007
Q99653	CHP1	0.6148	0.0237
O14967	CLGN	-0.8395	0.0019
Q96KA5	CLPTM1L	-1.5238	0.0002
Q9P000	COMMD9	-1.0098	0.0200
P14854	COX6B1	-0.7125	0.0001
Q6PUV4	CPLX2	-1.1107	0.0001
P50416	CPT1A	-1.2171	0.0001
P46108	CRK	-0.7032	0.0245
O75718	CRTAP	-0.9757	0.0001
P41240	CSK	0.8051	0.0185
P67870	CSNK2B	-0.6518	0.0041
P21291	CSR1	0.7624	0.0362
Q12996	CSTF3	-0.6428	0.0052
Q13363	CTBP1	-0.6302	0.0023
Q9NSA3	CTNNBIP1	-1.0762	0.0034

P10619	CTSA	-0.8666	0.0000
P09668	CTSH	-2.5719	0.0000
P07711	CTSL	-2.2984	0.0000
Q93034	CUL5	1.8372	0.0258
P78310	CXADR	-0.8708	0.0020
P00167	CYB5A	0.8199	0.0048
P99999	CYCS	0.9884	0.0013
Q9NWW4	CZIB	-1.4762	0.0002
P07108	DBI	-0.6259	0.0127
Q9Y4B6	DCAF1	0.7268	0.0005
O75935	DCTN3	-0.7695	0.0005
Q9BTE7	DCUN1D5	1.1231	0.0002
O94760	DDAH1	0.7400	0.0028
O00273	DFFA	-0.6750	0.0016
Q96LJ7	DHRS1	-0.7905	0.0000
Q86Y56	DNAAF5	-0.8373	0.0033
Q8IXB1	DNAJC10	-0.6998	0.0100
Q99543	DNAJC2	-0.6988	0.0199
Q13217	DNAJC3	1.4354	0.0073
P50570	DNM2	-0.5865	0.0009
Q9H3H5	DPAGT1	1.7000	0.0020
P27487	DPP4	0.6990	0.0288
Q14919	DRAP1	-0.8932	0.0441
Q99956	DUSP9	-0.9971	0.0012
P63167	DYNLL1	-1.0457	0.0000
Q9BQ95	ECSIT	-0.9464	0.0043
Q8NDI1	EHBP1	-1.0030	0.0007
Q9NZN3	EHD3	1.0667	0.0001
Q13144	EIF2B5	-0.7513	0.0321
Q14240	EIF4A2	0.6897	0.0153
P32519	ELF1	0.8386	0.0121
Q9NXB9	ELOVL2	2.0813	0.0336
Q9H9T3	ELP3	-1.9769	0.0001
Q9NPA0	EMC7	-1.2574	0.0022
P22413	ENPP1	0.6174	0.0001
Q9HCM4	EPB41L5	1.2752	0.0499
P29317	EPHA2	1.2262	0.0048
Q969X5	ERGIC1	-0.9000	0.0009
Q01844	EWSR1	-0.8041	0.0000
Q96KP1	EXOC2	-0.5897	0.0053
P00734	F2	-1.2105	0.0000
P07148	FABP1	1.9233	0.0103
Q96A26	FAM162A	1.0172	0.0008
Q92520	FAM3C	1.0973	0.0417
Q9Y4F1	FARP1	-0.9238	0.0002
P14324	FDPS	1.0905	0.0163
P02671	FGA	-2.5034	0.0000
P02675	FGB	-2.1737	0.0000
P02679	FGG	-1.7671	0.0000
Q14192	FHL2	-2.7044	0.0001
Q00688	FKBP3	-0.7645	0.0028
P21333	FLNA	-0.7085	0.0000
Q14254	FLOT2	-0.7306	0.0030
P49326	FMO5	-0.9663	0.0010

P02751	FN1	-3.1673	0.0000
Q9Y2H6	FNDC3A	-0.8173	0.0000
P02792	FTL	2.1643	0.0498
P04066	FUCA1	-1.3781	0.0000
P10253	GAA	-0.8339	0.0005
P60520	GABARAPL2	0.8821	0.0142
Q06546	GABPA	-1.0011	0.0035
Q8TAE8	GADD45GIP1	0.5918	0.0444
Q10471	GALNT2	-0.5957	0.0086
Q14353	GAMT	-0.7360	0.0116
Q8WXI9	GATAD2B	-0.8950	0.0312
Q8NB37	GATD1	-2.4581	0.0000
P28676	GCA	-1.5820	0.0001
Q92947	GCDH	1.0498	0.0299
Q8TB36	GDAP1	-0.6999	0.0069
Q13630	GFUS	-0.7350	0.0205
Q9UJY4	GGA2	-1.0893	0.0006
Q9H3K2	GHITM	1.3233	0.0251
Q92896	GLG1	-0.6681	0.0008
P35754	GLRX	0.7223	0.0045
O94925	GLS	0.8885	0.0031
P15104	GLUL	1.8815	0.0100
P29992	GNA11	1.0220	0.0002
Q14344	GNA13	-1.0241	0.0011
P62873	GNB1	-0.7167	0.0036
P63218	GNG5	0.7911	0.0012
P15586	GNS	-0.9667	0.0402
O95249	GOSR1	-1.1353	0.0009
P21695	GPD1	1.0444	0.0075
Q8TD30	GPT2	0.9108	0.0084
P07203	GPX1	-1.1051	0.0005
P36969	GPX4	-1.0844	0.0005
O60443	GSDME	-1.5365	0.0001
P49841	GSK3B	1.2325	0.0205
P06396	GSN	-0.8953	0.0003
P29083	GTF2E1	-0.8805	0.0009
Q9Y5Q8	GTF3C5	-0.8507	0.0329
Q9BSH5	HDHD3	0.6168	0.0004
Q9Y5Z4	HEBP2	-0.9879	0.0000
P06865	HEXA	-1.4267	0.0000
O14964	HGS	-0.7965	0.0081
Q9BW72	HIGD2A	-0.9296	0.0030
P35914	HMGCL	-1.3028	0.0080
Q01581	HMGCS1	0.7218	0.0377
P09601	HMOX1	-2.0152	0.0000
P41235	HNF4A	-1.3568	0.0001
Q9BUJ2	HNRNPUL1	-1.1010	0.0002
Q9UJC3	HOOK1	-0.6013	0.0155
Q5SSJ5	HP1BP3	-0.6793	0.0131
Q8NBQ5	HSD17B11	0.8061	0.0008
P04792	HSPB1	-0.8329	0.0000
Q92598	HSPH1	0.9808	0.0005
P42858	HTT	-0.9724	0.0048
Q9NX55	HYPK	1.1332	0.0003

Q2TAA2	IAH1	-1.1752	0.0013
P51553	IDH3G	-0.6478	0.0376
Q13907	IDI1	1.0498	0.0174
P08069	IGF1R	1.7594	0.0210
P01344	IGF2	-0.9705	0.0001
P11717	IGF2R	-1.1274	0.0000
Q9Y6K9	IKBKG	-1.8770	0.0162
Q27J81	INF2	-1.2916	0.0138
Q5TA45	INTS11	-0.6213	0.0005
P48200	IREB2	1.0354	0.0086
P56199	ITGA1	-0.7371	0.0182
P05556	ITGB1	1.0204	0.0004
P19823	ITIH2	-0.9462	0.0000
Q9Y287	ITM2B	1.0559	0.0364
P26440	IVD	-0.5968	0.0070
Q9P0J7	KCMF1	-1.1992	0.0027
Q8IZA0	KIAA0319L	-1.7449	0.0001
P08727	KRT19	-1.1217	0.0001
Q5XKE5	KRT79	-0.8596	0.0032
P05787	KRT8	-0.7954	0.0000
Q16719	KYNU	0.6899	0.0221
O15230	LAMA5	-2.0293	0.0000
P07942	LAMB1	-0.8392	0.0000
P11047	LAMC1	-1.0714	0.0007
P13473	LAMP2	1.6392	0.0053
Q71RC2	LARP4	1.2377	0.0115
Q14847	LASP1	-0.8094	0.0000
P01130	LDLR	0.7082	0.0212
Q99538	LGMN	-4.0776	0.0000
P50851	LRBA	0.6634	0.0041
P09960	LTA4H	-0.5870	0.0042
P02788	LTF	-5.8798	0.0000
Q9NX58	LYAR	1.4518	0.0440
Q5VWZ2	LYPLAL1	-1.1534	0.0000
P27338	MAOB	0.7884	0.0113
Q66K74	MAP1S	-1.0483	0.0002
O95819	MAP4K4	-1.4690	0.0001
P28482	MAPK1	-0.6199	0.0090
P27361	MAPK3	-1.2277	0.0002
Q9NX47	MARCHF5	-0.6123	0.0285
Q9NR56	MBNL1	0.8884	0.0011
Q9NUK0	MBNL3	-1.2344	0.0002
Q96N66	MBOAT7	-1.3672	0.0000
Q96PE7	MCEE	-0.8532	0.0011
Q9ULC4	MCTS1	-0.5912	0.0467
Q15648	MED1	-0.9689	0.0093
O75448	MED24	-1.2944	0.0006
P53582	METAP1	-0.6775	0.0117
Q9NRN9	METTL5	-0.9756	0.0039
Q99735	MGST2	-1.3197	0.0113
O14880	MGST3	-1.4018	0.0009
Q5JRA6	MIA3	-0.7278	0.0232
Q4VC31	MIX23	0.8772	0.0045
O95563	MPC2	0.7468	0.0188

Q9BYD1	MRPL13	-0.6480	0.0005
Q16540	MRPL23	-0.7218	0.0222
Q9P0M9	MRPL27	-1.7720	0.0159
Q9Y2Q9	MRPS28	0.6238	0.0047
O15457	MSH4	2.0589	0.0321
P02795	MT2A	2.2911	0.0000
P49914	MTHFS	1.0187	0.0023
P55157	MTPP	1.2575	0.0348
Q96S97	MYADM	0.6917	0.0055
Q969H8	MYDGF	-0.9958	0.0000
Q9UM54	MYO6	-0.6029	0.0282
Q4G0N4	NADK2	1.1877	0.0112
Q96HR8	NAF1	1.2516	0.0012
P54802	NAGLU	-1.1403	0.0039
Q99733	NAP1L4	-0.6310	0.0027
Q15003	NCAPH	0.9309	0.0262
O43674	NDUFB5	-1.4566	0.0012
O95139	NDUFB6	-1.5189	0.0298
O95298	NDUFC2	-1.4840	0.0000
O00217	NDUFS8	0.8372	0.0067
P49821	NDUFV1	-0.7671	0.0000
Q15843	NEDD8	-0.7883	0.0024
Q8IXH7	NELFCD	-0.8616	0.0002
Q8NEJ9	NGDN	-0.7922	0.0049
P14543	NID1	-2.0904	0.0001
Q9BYG3	NIFK	-0.7438	0.0139
Q9NQR4	NIT2	-0.7168	0.0182
Q9ULX3	NOB1	-0.7028	0.0003
Q5JPE7	NOMO1 (includes others)	0.5987	0.0169
O15118	NPC1	1.5511	0.0323
P16083	NQO2	-1.0230	0.0032
Q15738	NSDHL	1.2895	0.0246
Q9BSD7	NTPCR	-0.8083	0.0017
Q9UKX7	NUP50	0.7117	0.0056
Q9BVL2	NUP58	-0.9087	0.0073
P04181	OAT	0.7922	0.0027
Q6PK18	OGFOD3	-1.2397	0.0064
Q9UBD5	ORC3	-0.9852	0.0000
P02763	ORM1	-0.6700	0.0025
Q9BZF1	OSBPL8	-0.7466	0.0101
O15460	P4HA2	-0.7808	0.0008
Q9UKS6	PACSIN3	-0.8904	0.0008
O75781	PALM	-0.7850	0.0352
Q53EL6	PDCD4	-0.5931	0.0469
Q96HC4	PDLIM5	1.0419	0.0000
Q15121	PEA15	-0.8782	0.0102
Q86TG7	PEG10	-2.2686	0.0000
O96011	PEX11B	-0.7218	0.0190
O75381	PEX14	0.8412	0.0198
P35080	PFN2	-0.7220	0.0004
P18669	PGAM1	-0.6155	0.0000
Q8IXK0	PHC2	0.9696	0.0475
O43175	PHGDH	0.6087	0.0031
Q96FC7	PHYHIPL	-0.9316	0.0000

Q13492	PICALM	-0.8892	0.0009
Q92643	PIGK	-0.6649	0.0011
Q9H490	PIGU	-0.5948	0.0047
Q99569	PKP4	-1.7729	0.0358
Q15149	PLEC	-0.6513	0.0003
Q02809	PLOD1	-1.3055	0.0000
O00469	PLOD2	1.3595	0.0089
Q8IY26	PLPP6	-0.7800	0.0058
Q9NRX1	PNO1	-0.7099	0.0079
Q9NVS9	PNPO	-1.2858	0.0005
O15514	POLR2D	-1.0881	0.0023
P36954	POLR2I	-0.7044	0.0091
P62875	POLR2L	-0.8036	0.0000
O14802	POLR3A	-0.7796	0.0034
Q15165	PON2	-0.6475	0.0018
Q13427	PPIG	0.9623	0.0332
P49593	PPM1F	-1.1436	0.0008
Q96C90	PPP1R14B	-1.6920	0.0002
P53041	PPP5C	-1.1917	0.0005
P54646	PRKAA2	-0.6343	0.0124
P13861	PRKAR2A	-0.9902	0.0001
O75569	PRKRA	-0.8822	0.0031
Q14558	PRPSAP1	-0.6951	0.0031
P48634	PRRC2A	1.1566	0.0187
O75832	PSMD10	-0.9241	0.0422
Q14997	PSME4	0.6636	0.0103
O95456	PSMG1	-0.5885	0.0009
Q05397	PTK2	-1.0912	0.0207
Q15397	PUM3	-0.7207	0.0021
P49023	PXN	-0.6548	0.0011
Q9ULZ3	PYCARD	-0.8605	0.0207
P11234	RALB	0.7848	0.0056
P43487	RANBP1	-0.6103	0.0017
P62834	RAP1A	0.7622	0.0006
Q8IY67	RAVER1	-0.5824	0.0262
O43251	RBFOX2	-0.6865	0.0412
Q96T37	RBM15	1.8271	0.0364
P09455	RBP1	-2.7008	0.0000
P02753	RBP4	-1.1126	0.0028
Q14257	RCN2	-0.7287	0.0142
Q9P260	RELCH	-1.3288	0.0002
P78509	RELN	-0.7475	0.0081
Q9BWE0	REPIN1	0.8745	0.0023
Q86VR2	RETREG3	-0.9901	0.0175
Q6NUM9	RETSAT	-0.5955	0.0005
Q6NTF9	RHBDD2	-1.2829	0.0027
P52758	RIDA	1.5571	0.0451
Q5UIP0	RIF1	-0.7242	0.0211
Q9BVS4	RIOK2	-1.1926	0.0122
O00584	RNASET2	-1.3253	0.0000
Q96EP0	RNF31	-1.6019	0.0333
Q9H9Y2	RPF1	-0.9287	0.0030
P61353	RPL27	-1.0550	0.0000
P46779	RPL28	-0.6111	0.0004

P47914	RPL29	-1.9915	0.0000
P62899	RPL31	-0.7683	0.0006
P36578	RPL4	-0.8109	0.0000
P63220	RPS21	-0.7409	0.0000
P62854	RPS26	-1.9455	0.0000
Q9HB90	RRAGC	1.9453	0.0033
Q9Y3B9	RRP15	2.2865	0.0144
Q15050	RRS1	-0.5812	0.0060
Q9UHA3	RSL24D1	0.9200	0.0110
Q92541	RTF1	-1.4539	0.0121
P82979	SARNP	-0.5940	0.0009
Q8WTV0	SCARB1	0.6341	0.0246
O00767	SCD	1.0339	0.0056
Q96I15	SCLY	-1.2875	0.0015
O43819	SCO2	1.5143	0.0105
P18827	SDC1	-3.6599	0.0008
P34741	SDC2	1.9665	0.0356
O00560	SDCBP	1.9150	0.0371
Q99470	SDF2	-0.7758	0.0408
O15027	SEC16A	-1.1168	0.0053
P01011	SERPINA3	1.5516	0.0215
P30740	SERPINB1	-1.0953	0.0000
P35237	SERPINB6	-0.6794	0.0000
P36955	SERPINF1	-1.3570	0.0012
P08697	SERPINF2	-1.6701	0.0000
P31947	SFN	-1.8519	0.0000
O95470	SGPL1	-1.5068	0.0000
O75368	SH3BGRL	-1.6998	0.0020
Q9H299	SH3BGRL3	-1.3236	0.0000
Q99961	SH3GL1	-1.0324	0.0001
Q9Y371	SH3GLB1	-2.0293	0.0000
Q9NUL5	SHFL	1.1530	0.0249
Q9NXA8	SIRT5	-0.7927	0.0172
Q9UGH3	SLC23A2	-0.9630	0.0380
Q99808	SLC29A1	-0.5894	0.0000
P11166	SLC2A1	-1.0926	0.0000
P11169	SLC2A3	-1.4230	0.0017
Q9Y6M5	SLC30A1	0.9078	0.0134
P78383	SLC35B1	1.0242	0.0298
Q96K37	SLC35E1	-1.0681	0.0016
Q96QD8	SLC38A2	1.9947	0.0022
Q99624	SLC38A3	-0.7110	0.0001
Q15043	SLC39A14	1.9357	0.0058
Q92504	SLC39A7	-2.1203	0.0000
Q9Y289	SLC5A6	-0.9183	0.0052
O14745	SLC9A3R1	-0.6702	0.0000
Q969G3	SMARCE1	-0.8955	0.0026
O95721	SNAP29	-1.5104	0.0000
Q9Y5X1	SNX9	-0.7017	0.0002
P35610	SOAT1	1.1394	0.0018
P00441	SOD1	0.8677	0.0001
P04179	SOD2	0.9942	0.0014
Q8TCT8	SPPL2A	0.9826	0.0462
Q9Y6N5	SQOR	-1.3087	0.0000

P12931	SRC	-0.7878	0.0030
P37108	SRP14	-0.7349	0.0002
P61011	SRP54	0.7026	0.0034
P49458	SRP9	-0.9561	0.0012
O75494	SRSF10	-0.9218	0.0033
Q13247	SRSF6	-0.9861	0.0190
Q9P289	STK26	1.1106	0.0358
Q9UEW8	STK39	0.7464	0.0092
P63272	SUPT4H1	0.5930	0.0015
Q15526	SURF1	0.8355	0.0032
Q96A49	SYAP1	-1.1900	0.0052
P57105	SYNJ2BP	-0.6929	0.0491
O75410	TACC1	1.3202	0.0011
Q01995	TAGLN	-0.6415	0.0005
Q03518	TAP1	-0.7530	0.0126
Q9UBB9	TFIP11	0.7791	0.0308
P10646	TFPI	-3.7494	0.0000
P21980	TGM2	-2.0750	0.0000
Q9Y2W1	THRAP3	0.6096	0.0348
Q07157	TJP1	-0.8202	0.0002
Q9H061	TMEM126A	-0.8704	0.0127
Q9P0S9	TMEM14C	1.1741	0.0027
Q6UW68	TMEM205	-1.5601	0.0001
Q96K49	TMEM87B	1.9912	0.0006
Q9NVH6	TMLHE	-4.5886	0.0380
P63313	TMSB10/TMSB4X	-1.2486	0.0000
Q9H0E2	TOLLIP	-0.6840	0.0062
O60784	TOM1	-0.9555	0.0004
Q96B49	TOMM6	0.8518	0.0066
P11388	TOP2A	0.8965	0.0061
Q8NFK8	TOR1AIP2	1.5555	0.0160
Q53FA7	TP53I3	-0.6342	0.0000
Q96S44	TP53RK	-0.9755	0.0022
O14773	TPP1	-1.4442	0.0000
O43617	TRAPPC3	1.7749	0.0000
Q8TEL6	TRPC4AP	-1.1912	0.0203
Q99614	TTC1	-0.6169	0.0026
Q5R3I4	TTC38	-2.0081	0.0000
Q13509	TUBB3	-0.9551	0.0000
O75896	TUSC2	0.7654	0.0003
P51668	UBE2D1	-0.8299	0.0001
P61077	UBE2D3	-0.8054	0.0000
P61088	UBE2N	-0.6131	0.0073
Q05086	UBE3A	-1.3053	0.0036
Q9BZL1	UBL5	0.7039	0.0358
Q9UHD9	UBQLN2	-2.2741	0.0000
O94874	UFL1	-0.6007	0.0016
Q96PU4	UHRF2	-1.4927	0.0035
Q14694	USP10	-0.6817	0.0019
Q9UPU5	USP24	-0.9530	0.0007
Q9NYH9	UTP6	-0.6807	0.0175
P46939	UTRN	0.7286	0.0383
Q8NBZ7	UXS1	-1.4431	0.0052
Q9BV40	VAMP8	2.7832	0.0000

<b>P50552</b>	VASP	0.8423	0.0001
<b>P61758</b>	VBP1	1.1746	0.0101
<b>Q9BQB6</b>	VKORC1	-0.6857	0.0007
<b>Q9UK41</b>	VPS28	-1.2373	0.0030
<b>Q9NRW7</b>	VPS45	-0.7106	0.0090
<b>P04004</b>	VTN	-0.7072	0.0363
<b>Q9BZH6</b>	WDR11	-1.0390	0.0000
<b>Q9GZS3</b>	WDR61	-1.4226	0.0000
<b>Q8IWA0</b>	WDR75	-0.6845	0.0004
<b>O00308</b>	WWP2	-1.2178	0.0000
<b>P67809</b>	YBX1	-1.1221	0.0000
<b>Q7Z739</b>	YTHDF3	-1.2841	0.0037
<b>Q86VM9</b>	ZC3H18	-0.8035	0.0139
<b>Q96ME7</b>	ZNF512	-0.9504	0.0031
<b>Q9Y5V0</b>	ZNF706	1.5032	0.0118